Title

Exceptional Stress-director Coupling Relation and Fracture Behavior of Liquid Crystal Elastomers

Author

Wei, Chen

Publication Date

2025

Peer reviewed|Thesis/dissertation

UNIVERSITY OF CALIFORNIA

Los Angeles

Exceptional Stress-director Coupling Relation and Fracture Behavior of Liquid Crystal Elastomers

A dissertation submitted in partial satisfaction of the

requirements for the degree Doctor of Philosophy

in Mechanical Engineering

by

Chen Wei

2025

ABSTRACT OF THE DISSERTATION

Exceptional Stress-director Coupling Relation and Fracture Behavior of Liquid Crystal Elastomers

by

Chen Wei

Doctor of Philosophy in Mechanical Engineering

University of California, Los Angeles, 2025

Professor Lihua Jin, Chair

A liquid crystal elastomer (LCE) combines cross-linked elastomers and rod-like liquid crystals (LCs), presenting the hyperelasticity characteristics of elastomers and the unique properties associated with LCs. A LCE is a highly promising material utilized in the realm of actuators, soft robotics, and related applications, primarily attributed to its unique capability of spontaneous strain achieved through changes in ordering and director. This dissertation aims to characterize the stress-director coupling behavior under different loading conditions and its effect on crack-tip fields and fracture propagation, providing a comprehensive understanding of LCEs and guidance in further design.

First, LCEs exhibit extremely slow relaxation due to a combination of viscous network deformation and director reorientation. We study the rate-dependent stress-director coupling behavior under various loading rates. Our experimental setup successfully captures rate-dependent stress, strain, and director reorientation in real-time, and distinguishes the two relaxation time scales of the network deformation and mesogen reorientation. Based on the experimental findings, a viscoelastic constitutive model is developed to manifest the relation between rate-dependent macroscopic deformation and microscopic director rotation in LCEs. This work provides a comprehensive investigation into and mechanistic understanding of the rate-dependent behavior of LCEs.

Secondly, we explore the exceptional stress-director coupling effect around the crack tip. We examine edge-cracked LCEs samples subjected to tensile loading at different angles relative to the initial director. Unlike traditional elastomers, LCEs exhibit an elliptical stress/strain distribution, attributed to the significant and inhomogenous director reorientation at the crack tips. Notably, we observe a domain wall formation along a certain polar angle at the crack tip, caused by opposite director rotation. Moreover, LCEs with a tilted initial director to the loading exhibit much smaller crack openings and energy release rates compared to the parallel loading. We attribute these findings to a combined effect of bulk softening at the remote region and the formation of domains of opposite director rotation near the crack tip.

In the end, we report the intriguing crack propagation behavior in LCEs during post-cut experiments with varying initial directors. A post-cut method, which induces a crack after the sample is stretched and held for a long time, is utilized to minimize the effect of bulk viscosity, enabling a systematical record of crack propagation rates and directions. Besides, a growth delay is observed after post-cutting, followed by steady-state propagation. The results reveal that

cracks typically propagate perpendicular to the director ahead of the crack tip. During the steady stage, crack velocity increases with higher pre-stretching levels. Notably, anomalous growth occurs when strip domains and monodomain coexist at the crack tip, attributed to the lower fracture energy in the strip domain compared to monodomain. This study offers valuable insights into fracture behavior and provides significant contributions to the development of fracture criteria.

The dissertation of Chen Wei is approved.

Jiann-Wen Ju

Samanvaya Srivastava

Vijay Gupta

Vinay Kumar Goyal

Lihua Jin, Committee Chair

University of California, Los Angeles

2025

TABLE OF CONTENTS

LIST OF FIGURES

LIST OF TABLES

ACKNOWLEDGMENTS

First of all, I would like to express my deepest gratitude to my advisor, Prof. Lihua Jin, whose exceptional guidance, expertise, and continuous support throughout my Ph.D. journey. Under her mentorship, I have gained the skills and confidence to tackle new challenges. She has not only supported my academic growth but also my personal development. I still remember the hard time when I began studying LCEs. Coming from a background with limited knowledge of mechanics, I was completely at a loss about where to start. It is Prof. Jin's patient teaching and encouragement that help me to overcome these challenges. She introduced me to the fascinating world of mechanics and opened my eyes to its beauty. Since then, with confidence and perseverance, I have learned to embrace challenges and am not afraid of any difficulties, whether in academics or life. I think the biggest treasure gained in Ph.D. study is not how much paper is published, but the ability to solve complex problems and the optimistic mindset I now carry toward an uncertain future. For all of this, I will always be deeply grateful to Prof. Jin.

I would also like to express sincere thanks to my committee members: Prof. Jiann-Wen Woody Ju, Prof. Samanvaya Srivastava, Prof. Vijay Gupta, and Prof. Vinay Goyal, for their thoughtful suggestions, constructive feedback, and continuous encouragement. Their valuable guidance significantly improves the quality of my work, and I deeply appreciate their time and dedication. I would offer a special thank you to Prof. Vinay Goyal who teaches me how to utilize my knowledge to solve real-world problems. This practical insight will undoubtedly be invaluable in my further career development.

I also want to thank my friends and colleagues. I have learned a lot from Dr. Yu Zhou and Dr. Yuzhen Chen, and I am grateful for their knowledge and guidance. I appreciate Boliang Wu

for sharing valuable tips on conducting experiments. I also thank Weixuan Liu's support in both research and life. And I would thank all the members of the Mechanics of Soft Material Lab.

And I would like to offer my heartfelt thanks to my parents, to whom I owe everything. Their endless love, support and care have been the pillars of my strength throughout my life. While most of my peers can spend time with their parents, I have often found myself apart from them due to my studies. I always feel frustrated and sorry for not being able to be them as much as I would have liked. I hope with all my heart that in the future, we will have more time to be together and I can show them the gratitude and love they so richly deserve.

Last but not least, I would like to thank myself and my cat, Sunny. Together, we have walked through such a long and challenging journey. The road ahead still holds challenges, but I am confident we can face whatever comes next. Thank myself for not giving up. I will continue to move forward with determination and hope.

VITA

2016-2018 M.S in Civil Engineering, Northwestern University, Evanston, US

2012-2016 B.S in Civil Engineering, Zhejiang University, China

SELECTIVE PUBLICATIONS

[1] Zhou, Y., **Wei, C.,** & Jin, L. (2025). A modified semi-soft model of liquid crystal elastomers: application to elastic and viscoelastic responses. *Journal of the Mechanics and Physics of Solid,* 106027

[2] **Wei, C**., Zhou, Y., & Jin, L. (2025). Intriguing crack propagation of a liquid crystal elastomer. *In preparation*

[3] **Wei, C**., Zhou, Y., Hsu, B., & Jin, L. (2024). Exceptional stress-director coupling at the crack tip of a liquid crystal elastomer. *Journal of the Mechanics and Physics of Solids*, 105522.

[4] Guo, Y., Luo, Y., Plamthottam, R., Pei, S., **Wei, C.,** Han, Z., Fan, J., Possinger, M., Liu, K., Zhu, Y. and Fei, Z., (2024). Haptic artificial muscle skin for extended reality. *Science Advances*, *10*(43), p.eadr1765.

[5] **Wei, C.**, Cao, S., Zhou, Y., Lin, D., & Jin, L. (2023). Rate-dependent stress-order coupling in main-chain liquid crystal elastomers. *Soft Matter*, *19*(41), 7923-7936.

[6] Zeng, M., Du, Y., Jiang, Q., Kempf, N., **Wei, C.**, Bimrose, M. V., ... & Zhang, Y. (2023). High-throughput printing of combinatorial materials from aerosols. *Nature*, *617*(7960), 292-298.

[7] Wang, H., **Wei, C**., Zhang, Y., Ma, Y., Chen, Y., Wang, H., & Feng, X. (2022). Tunable three-dimensional vibrational structures for concurrent determination of thin film modulus and density. *Journal of Applied Mechanics*, *89*(3), 031009.

[8] Li, Y., Ma, Y., **Wei, C.,** Luan, H., Xu, S., Han, M., ... & Rogers, J. A. (2018). Thin, millimeter scale fingernail sensors for thermal characterization of nail bed tissue. *Advanced Functional Materials*, *28*(30), 1801380.

[9] Crawford, K. E., Ma, Y., Krishnan, S., **Wei, C.**, Capua, D., Xue, Y., ... & Rogers, J. A. (2018). Advanced approaches for quantitative characterization of thermal transport properties in soft materials using thin, conformable resistive sensors. *Extreme Mechanics Letters*, *22*, 27-35.

[10] Madhvapathy, S. R., Ma, Y., Patel, M., Krishnan, S., **Wei, C.,** Li, Y., ... & Rogers, J. A. (2018). Epidermal electronic systems for measuring the thermal properties of human skin at depths of up to several millimeters. *Advanced Functional Materials*, *28*(34), 1802083.

Chapter 1 Introduction

Soft smart materials have seen remarkable progress, driven by the increasing demand for enhanced control, flexibility, reliability, and versatility. Among these, liquid crystal elastomers (LCEs) stand out as one of the highly promising materials. Compared to other types of soft stimuli-response materials, LCEs have the advantages of high energy density, fast responses, safe operation and reversible actuation, facilitating broad applications including stimuli-responsive actuators [1–3], biomedical devices [4,5], artificial muscles [6,7] and soft robots [8–12]. Particularly, LCEs can be activated by a wide range of external stimuli, including heating [13–15], light irradiation [10,16,17], magnetic fields [18–20], and electrical fields [21–23]. This multi-modal responsiveness broadens the application potential and makes LCEs a versatile tool in advanced material science. This dissertation studies the constitutive and fracture behavior of LCEs under various loading conditions, providing a comprehensive understanding of stress-director coupling behavior and its effect in the presence of a crack. The findings not only advance the fundamental knowledge of LCEs but also offer insights for designing LCEs, paving the way for future commercial use.

1.1 Basic of LCEs – Stress-director Coupling

Liquid crystal elastomers (LCEs) present a synergistic combination of cross-linked elastomers and rod-like liquid crystals (LCs), thereby exhibiting both the hyperelasticity of elastomers and the unique properties associated with LCs [24]. In this dissertation, we focus on the nematic main-chain LCEs, where LCs are integrated into the network backbone (Figure

1.1a). Nematic LC mesogens tend to align in a specific orientation, with the average direction called the director, $\boldsymbol{d}$ [25–27], which can be identified by their uniaxial optical axis.

LCEs have unique mechanical behavior attributed to the interaction between mechanical deformation and the alignment of directors. When LC mesogens are heated above a transition temperature T_{ni}, they undergo a phase transition from the aligned nematic phase to the randomly oriented isotropic phase, inducing macroscopic contraction of LCEs (Figure 1.1b) [24,28]. Figure 1.1b shows the temperature-induced shape change in a monodomain LCE, highlighting shrinkage along the director axis and expansion along the orthogonal dimensions due to the disordering of LCs. Moreover, LCs can also be reoriented by other external stimuli, such as external loading, magnetic fields, and electrical fields, which can lead to significant spontaneous strain up to around 400% or stress if constrained. On the other hand, mechanical deformation not parallel to the director can reorient the director to the stretching direction [24,29–34], inducing a stress plateau in the stress-strain relation (Figure 1.1c) [24,28]. Figure 1.1c presents stress-stretch curves for LCEs with various initial directors, demonstrating a more obvious plateau when the initial director orientation deviates further away from the stretching direction. This distinctive stress-director coupling effect differentiates LCEs from conventional soft materials, endowing them with unique mechanical responses under various loading conditions.

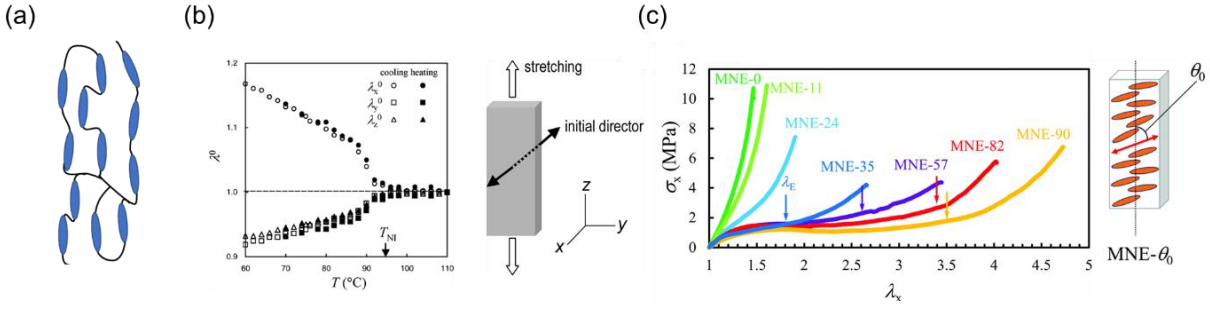

Figure 1.1 (a) Schematic of main-chain monodomain LCEs. (b) Thermal-induced shape variation in the unloaded state [28]. (c) Stress-strain curves with various initial directors under tension [29].

1.2Rate-dependent Behavior of LCEs

It has been reported that LCEs present significant rate-dependent stress-strain relations [29,30,35–47]. Different from traditional viscoelastic materials governed solely by viscous network dynamics, LCEs' mechanical response is intricately influenced by both viscous networks and the dynamics reorientation of directors. The interplay results in distinctive rate-dependent characteristics under tension and relaxation.

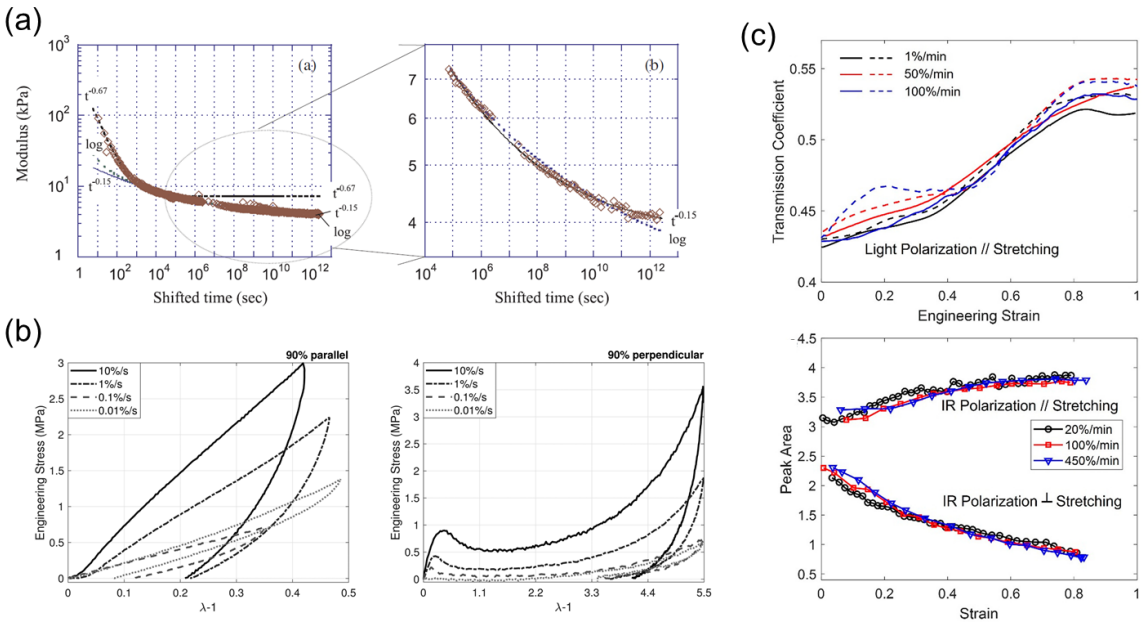

Figure 1.2 (a) Stress relaxation of LCEs [39].(b) Stress-strain curves of LCEs under parallel/perpendicular loading from rates of 0.01%/s to 10%/s [29]. (c) Director-strain relation at different loading rates [32].

Figure 1.2a shows multi-stage stress relaxation in LCEs, demonstrating that LCs' reorientation has a profound influence on relaxation, and the material does not reach equilibrium after a long time of relaxation. In tension tests, LCEs behave similarly to normal viscoelastic

materials when director roration is negligible. However, it presents a rate-dependent stress plateau driven by dynamic director reorientation (Figure 1.2b). The relaxation timescales of the network and directors differ markedly, as shown in Figure 1.2c, where the director exhibits minimal rotation at loading rates far from equilibrium. To illustrate the complex stress-director coupling effect, several viscoelastic models have been developed, which will be explored in detail in Chapter 2.

1.3 Fracture Behavior of LCEs

Understanding the stress/strain field around a defect is essential for evaluating the fracture behavior of soft materials [48–50]. The complex stress-director coupling effect can induce significant inhomogeneous deformation near defects, resulting in an unusual stress/strain distribution different from traditional Neo-Hookean (Figure 1.3a) [51–53].

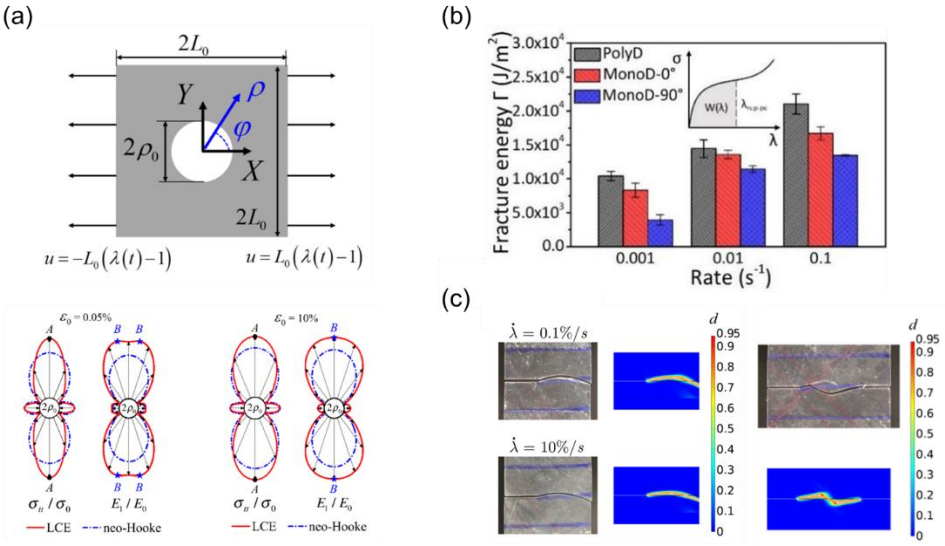

Figure 1.3 (a) Unusual stress and strain concentration on a LCE plate with a hole [51]. (b) Fracture energy of polydomain and monodomain under parallel and perpendicular loading [54]. (c) Tilted crack propagation path in LCEs with initial director $\theta_0 = 45°$ [55].

Fracture energy, a critical parameter to assess a material's resistance to failure, is commonly measured through pure shear in soft materials [56]. Rate-dependent fracture energy encompasses the intrinsic fracture energy associated with network chain breakage and the dissipation energy that occurs during crack propagation [57–59]. Figure 1.3(c) presents the rate-dependent fracture energy of polydomain and monodomain LCE under parallel and perpendicular, indicating the profound influence of director reorientation fracture energy. In addition, the fracture energy of LCEs is highly temperature dependent, influenced not only by the change of network chains but also by the transition of directors from an ordered to a disordered state as temperature increases [60].

Crack growth analysis, especially in viscoelastic materials, remains a challenging yet crucial area of research. There is limited research on the crack growth path of LCEs. In pure shear tests, both polydomain and monodomain LCEs under perpendicular and parallel loading exhibit a horizontal crack propagation path [54,61]. However, when the loading direction is inclined relative to the initial director, the crack path becomes tilted. Figure 1.3c illustrates the inclined crack propagation path in LCEs with a tilted initial director $\theta_0 = 45°$ under tension [55]. A phase-field model, based on the assumption that the crack propagates perpendicularly to the director, has been proposed and generally aligned well with the experimental observation at different tension rates.

1.4 Motivation and Objectives

LCEs have gained remarkable attention due to their unique mechanical properties and potential broad applicability across various fields. Despite extensive research, the complex interplay between stress-director coupling and fracture behaviors remains inadequately

understood. It is still an ongoing challenge to systematically characterize mechanical responses under diverse loading conditions, particularly in the presence of a crack tip. In this dissertation, we will rigorously investigate the mechanisms, providing a comprehensive analysis that enhances the understanding of LCEs. The findings are intended to expand their applications and inform the development of materials with improved performance characteristics.

In this dissertation, we explore the dynamic changes in stress, strain and director orientation through both experimental and theoretical (Figure 1.4) [62]. Based on the birefringence of LCs, we have developed a universal technique to track the director trajectory, which can be applied to various types of LCEs. Since there is additional shear strain induced by director reorientation and LCEs typically experience inhomogeneous deformation, we employ the digital image correlation method to capture local strain components. By measuring stress, strain, and director simultaneously, we can observe the stress-director coupling effect, which helps us develop a more reasonable constitutive model that reflects the unique mechanical behavior of LCEs.

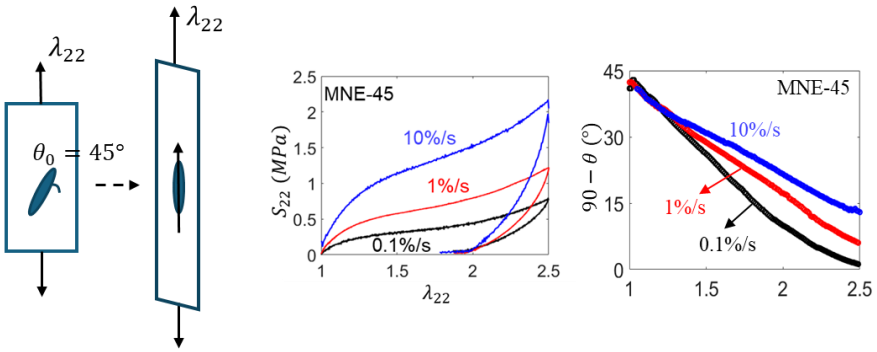

Figure 1.4 Rate-dependent mechanical behavior of LCEs [62]

Additionally, there is very limited research on the fracture behavior of LCEs. Because of the complex material properties of LCEs, it is challenging to derive analytical solutions near a

sharp crack tip. To address this issue, we combine developed experimental testing with a novel algorithm implemented within the ABAQUS UEL subroutine to investigate an edge-cracked LCE sample under various loading directions (Figure 1.5) [63]. This approach reveals exceptional stress, strain, and director distributions around the crack tip. For the first time, detailed insights into the local behavior at the crack tip in LCEs are presented.

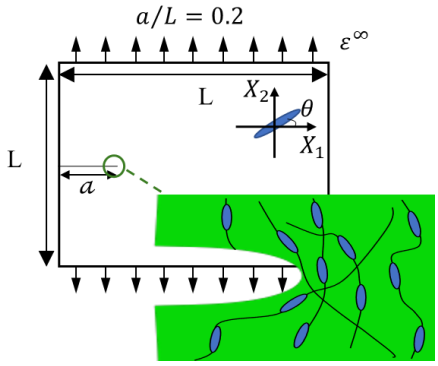

Figure 1.5 Schematic of an edge-cracked LCE sample under tension [63].

Although people have reported rate-dependent and stretching-direction-dependent fracture energy, most studies focus on either polydomain or monodomain under perpendicular or parallel loading, and the applicability of traditional analysis (such as pure shear) across all scenarios remains uncertain. Moreover, establishing appropriate fracture criteria for such complex materials continues to be a challenge. In this dissertation, we utilize a post-cut method and report crack growth in LCEs with varying initial directors (Figure 1.6) [64]. The relation among the crack propagation, initial directors, and pre-stretching levels are investigated, which offers valuable guidance to develop more robust criteria and methods.

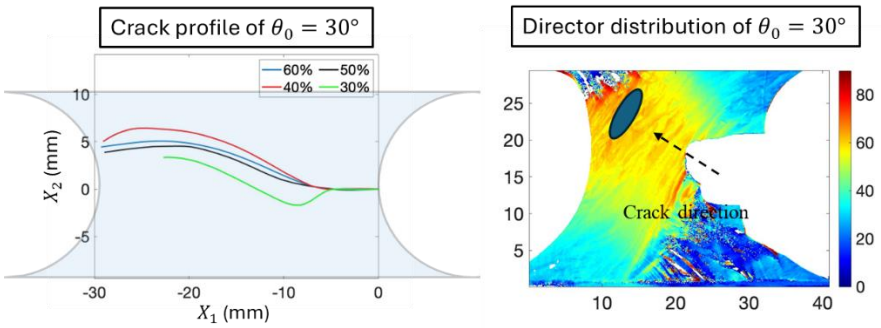

Figure 1.6 An example of crack propagation profile and director distribution [64].

1.5 Outline of the Dissertation

The goal of this dissertation is to characterize the stress-director coupling relation and fracture behavior of LCEs, providing a comprehensive understanding of the mechanisms of LCEs and guidance in further designing LCEs. The dissertation is organized as follows:

In Chapter 2, we systematically measured stress, strain and director reorientation under various loading rates and distinguished the relaxation time scales of the network and director. A general viscoelastic model was developed to further illustrate the rate-dependent stress-director coupling effect.

Chapter 3 presents an exceptional stress-director coupling effect around the crack tip. We stretched an edge-cracked LCE sample without crack propagation, reporting stress, strain, and director distribution. Besides, we evaluated the fracture behavior based on the crack opening displacement and energy release rate.

In Chapter 4, we study the crack propagation rate and direction in LCEs with various initial directors. We utilized a post-cut method and analyzed the influence of the pre-stretching level and initial directors on crack propagation. A phase field model was utilized to demonstrate the effect of director reorientation.

Chapter 5 concludes the dissertation.

Chapter 2 Rate-dependent Stress-director Coupling

Although the rate-dependent stress-strain relation of LCEs has already been widely observed, the effect of the intricate interplay of director rotation and network extension on the viscoelastic behavior of main-chain LCEs remains inadequately understood. In this Chapter, we present real-time measurements of the stress, director rotation, and all strain components in main-chain nematic LCEs subjected to uniaxial tension both parallel and tilted to the initial directors at different loading rates and relaxation tests. We find that both network extension and director rotation play roles in viscoelasticity, and the characteristic relaxation time of the network extension is much larger than that of the director rotation. Interestingly, the gradual change of the director in a long-time relaxation indicates the director reorientation delay is not solely due to the viscous rotation of liquid crystals but also arises from its coupling with the highly viscous network. Additionally, significant rate-dependent shear strain occurs in LCEs under uniaxial tension, showing non-monotonic changes when the angle between the stretching and the initial director is large enough. Finally, a viscoelastic constitutive model, only considering the viscosity of the network by introducing multiplicative decomposition of the deformation gradient, is utilized to manifest the relation between rate-dependent macroscopic deformation and microscopic director rotation in LCEs.

2.1 Introduction

A large number of previous studies about side-chain LCEs show mesogen rotation and network extension have different characteristic times.[22,37,39,41] Fukunaga *et al*.[22] studied the deformation of side-chain LCEs under an electro-optical effect and found the director rotates about 1 order of magnitude faster than the mechanical deformation. Clarke *et al*.[37] studied

stress relaxation during the polydomain-monodomain transition with stress fitting by a power law in a short time and a logarithmic scale in a long time, which they explained by a proposed theoretical model considering a cooperative mechanical barrier for each domain rotation. Hotta and Terentjev[39] systematically investigated the rate-dependent and relaxation responses of side-chain LCEs, and also reported two distinct relaxation regions for long-time stress relaxation. Although fitting both regions by power laws, they found the short-time region shows a power exponent of 0.67, representing the stress relaxation is facilitated by the director rotation due to the polydomain-to-monodomain transformation, while the long-time region shows a power exponent of 0.15, where the director relaxation is almost finished and the LCEs behave like isotropic rubber. Schonstein *et al*.[65] reported a broad distribution of director relaxation times but with a small mean relaxation time on the order of 0.01s via light scattering. Previous studies showed that shape recovery of LCEs takes a very long time and requires a very slow loading rate of around $10^{-4}\ s^{-1}$ to reach quasi-equilibrium mainly due to the slow relaxation of the network.[29,39,42,47] These findings suggest that the director rotates slightly faster than the network deforms. Researchers have also shown that the crosslinker forming conditions, director fields, LC phases, chemical components, and many other parameters could profoundly influence the viscoelasticity of LCEs.[38,41–46] However, the viscoelasticity of main-chain LCEs was not studied intensively until very recently. The comprehensive understanding of viscoelasticity in main-chain LCEs remains challenging due to the complicated synergy of the network extension and mesogen rotation to give rise to high viscosity. Azoug *et al*.[36] and Martin Linares *et al*.[40] studied the main-chain polydomain LCEs under uniaxial tension, reporting rate-dependent anisotropic stress responses. Moreover, Luo *et al*.[32] evaluated the director alignment of main-

chain monodomain LCEs by optical measurements, finding the director almost reaches equilibrium rotation at the loading rate of 450%/min. However, it is not clear what the relaxation time scales of the network extension and director rotation are for main-chain LCEs, and how they influence the macroscopic stress-strain behavior and microscopic director rotation.

To better understand how viscoelastic LC reorientation affects the mechanical responses of LCEs, we need to capture the real-time director rotation at different loading rates. Wide-angle X-ray scattering [29,66–68] (WAXS) and polarized Fourier transform infrared spectroscopy [28,34,69,70] (FTIR) have been used to measure the mesogen reorientation. However, WAXS can only obtain diffraction patterns at quasi-static loading, while FTIR has a strict requirement of specific functional groups on the chain backbone, giving an angular-dependent absorbance spectrum. Both of them have the restriction that they cannot measure universal main-chain LCEs orientation dynamically. Conversely, polarized optical microscopy is an alternative method to capture mesogen reorientation under fast loading [31,32,68,71]. Recently, Luo *et al*.[32] used crossed-polarized optical measurements to evaluate the director rotation in monodomain LCEs at different loading rates. Mistry *et al*.[31] used polarized optical microscopy to measure the director distribution in LCEs subjected to step stretching almost perpendicular to the initial director. Here, we will use crossed-polarized optical measurement to characterize the director rotation of LCEs under oblique stretching at different rates. The optical data will be recorded at different angles of the crossed polarizer and analyzer with respect to the stretching direction at different strains to probe the director. More details can be found in section 2.2.

Some viscoelastic models are developed to better understand the viscoelasticity mechanism of LCEs. Zhang *et al.*[72] and Zhou and Bhattacharya [73] proposed a viscoelastic

model considering both viscous network and director via applying a simple Rayleigh dissipation energy. It shows the semi-soft elasticity effect, rate-dependent stress, and director rotation. However, as the stress is the summation of the elastic and viscoelastic contributions, which is equivalent to a simple Kelvin-Voigt model, it cannot accurately capture the stress response under high loading rates due to an impractical instantaneous non-zero stress, and neither can it capture relaxation tests due to an unrealistic constant stress. Later, Wang *et al*.[74] proposed a nonlinear viscoelastic model by multiplicative decomposition of the deformation gradient to elastic and viscous parts. The predicted stress-strain behavior of LCEs under loading perpendicular to the initial director agrees well with the experimental results [36]. Here, following the work of Wang *et al*.[74], we establish a viscoelastic LCE model by considering the more realistic viscosity of the network and the low viscosity of the director based on our experimental measurements. Furthermore, the semi-soft elasticity is introduced in the elastic free energy.

This Chapter aims to bridge the existing knowledge gap in understanding the effect of the intricate interplay of director rotation and network extension on the viscoelastic behavior of LCEs. In particular, we systematically characterize the real-time director-stress-stretch relations for main-chain monodomain LCEs with different initial directors under different loading rates, showing not only rate-dependent stress-stretch behavior, but also rate-dependent director-stretch relation. Since director rotation also induces shear strain, we apply digital image correlation (DIC) to quantitatively measure the fields of all the rate-dependent strain components relative to the mesogen rotation. Moreover, we conduct relaxation tests and record the time evolution of the stress and director under fixed stretch. By comparing the results from the rate-dependent director-stress-stretch measurements and relaxation tests, we further distinguish the relaxation

times of the network and director. To better understand how the two viscoelastic dissipation processes govern the microscopic director rotation and macroscopic deformation, we develop a viscoelastic model via the multiplicative decomposition-based method, which implements more realistic viscosity and elastic energy compared to existing literature. This Chapter is organized as follows. In section 2.2, we introduce the experimental methodology. In section 2.3, we report the experimental results, including rate-dependent stress-strain and director-strain relations, and stress and director relaxation results. The theoretical model and the predicted viscoelastic behavior compared with the experimental results are presented in section 2.4. Section 2.5 concludes the Chapter.

2.2 Experimental Methods

2.2.1 Sample Preparation

In this study, the main-chain monodomain LCEs were synthesized via a two-stage thiol-acrylate Michael addition-photopolymerization (TAMAP) reaction [75]. The crosslinker, pentaerythritol tetrakis(3-mercaptopropionate) (PETMP, 95%), and chain extender, 2,2-(ethylenedioxy) diethanethiol (EDDET, 95%), were obtained from Sigma-Aldrich and used as received. The diacrylate mesogen, 1,4-Bis-[4-(3-arcyloyoxypropyloxy) benzoyloxy]-2-methylbenzene (RM257, 95%), was purchased from Wilshire company. Dipropylamine (DPA, 98%) and (2-hydroxyethoxy)-2-methylpropiophenone (HHMP, 98%) were selected as the catalyst and photoinitiator to enable the second-stage photopolymerization reaction, respectively. Toluene (98%) was used as the solvent for RM257. To prepare a sample, firstly, RM257 was fully dissolved in a vial with 60 wt% of toluene at 80 ℃. Then, PETMP, EDDET, HHMP, and DPA solution (DPA:toluene = 1:50) were poured into the solution and mixed using a vortex

mixer for 60 s to obtain a uniform solution. The molar ratio of thiol functional groups between PETMP and EDDET was 15:85, corresponding to a ratio of 15 mol% PETMP. The molar ratio of DPA with respect to the thiol functional group was 1 mol%, while the molar ratio of HHMP was 1 mol%. The solution was degassed for about 2 mins to remove all bubbles and then poured into a mold. Then the samples were cured at room temperature for 24 hours and put into an oven at 80 ℃ for another 24 hours to remove the toluene from the LCE sample. At this stage, thiol-acrylate formed a loose network and the sample showed an opaque appearance at room temperature. There would be an excess of 15 mol% acrylate groups for a second-stage photo-crosslinking reaction. In the second stage, the LCE sample was stretched uniaxially to 90% strain by a mechanical stretcher. The pre-stretch forced mesogens to reorientate to the tension direction, and the sample became transparent, indicating a monodomain LCE. The pre-stretched sample was exposed to UV light for 1 hour to photopolymerize the excessive acrylate groups, forming a denser network. After releasing the samples from the stretcher, a thin film of monodomain LCE sheet remains.

Rectangular strips with a width of 3 mm and length of 35 mm were cut out of the LCE sheet with angles $\theta_0 = 90°, 60°, 45°$, and $30°$ between the director and the $X_1 - axis$, as shown in Figure 2.1. The angles between the longitudinal direction and the director were measured by a protractor and further verified by the optical polariscopy method, which will be discussed in section 2.2.3. The samples are designated as monodomain nematic elastomers-θ_0 (MNE-θ_0), i.e. MNE-90, MNE-60, MNE-45 and MNE-30

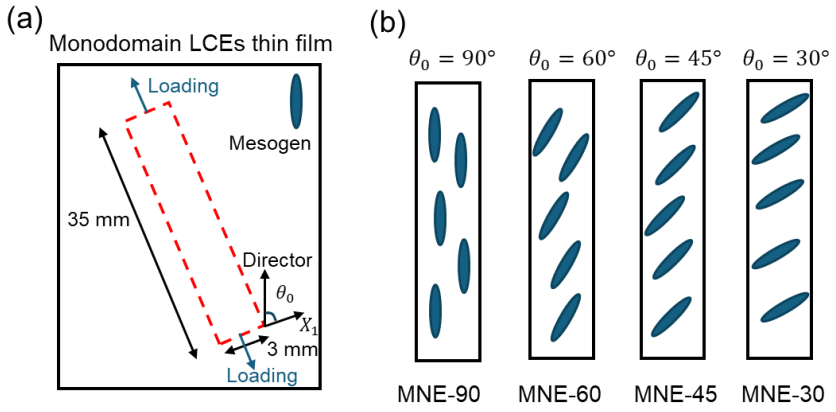

Figure 2.1 Schematics of specimens with different initial directors. (a) The specimen (red dashed line) was cut from a LCE thin film with the angle between the director and the $X_1 - axis$ defined as θ_0. (b) Specimens with different initial directors are defined as MNE-90, MNE-60, MNE-45, and MNE-30, corresponding to $\theta_0 = 90°,\ 60°,\ 45°$ and $30°$, respectively. The specimens were 3 mm in width and 35 mm in length.

2.2.2 Uniaxial Stretch

Uniaxial tension measurement was performed in the longitudinal direction of a LCE specimen at different loading rates using an Instron universal testing machine (Model 5944) with a 50 N load cell to record the LCE rate-dependent stress-strain relationship. A specimen was mounted in a pair of tensile grips, leaving a gauge length of 15 mm. The ratio of the length to width (= 5) is high enough to ensure that the majority of the specimen undergoes uniaxial tension, with negligible edge effects. The thickness was measured at three locations by an electronic caliper, giving the average thickness over all specimens to be 0.11 ± 0.01 mm. The specimens MNE-90, MNE-60, MNE-45, and MNE-30 were uniaxially stretched up to 40%, 100%, 150%, and 200% strain, respectively, with loading rates of 10%/s, 1%/s, and 0.1%/s, and unloaded at the same rates until stress reached zero. The maximum stretches were set as high as

possible, but below the fracture points of specimens with different directors to ensure completion of the tests. Although the specimens show complete recovery at room temperature after unloading, to accelerate the recovery process, after each loading and unloading, a specimen was put on a hotplate at 30 ℃ for 5 mins and then at room temperature for another 10 mins to release any residual stress. The next test would be run once the specimen was fully recovered. From these tests, we were able to plot the nominal stress as a function of stretch. Here the stretch is defined as $\lambda = L/L_0$, where L_0 is the unstretched gauge length (15 mm) and L is the extended length.

2.2.3 Crossed-polarized Optical Measurement

Director rotation driven by stretching at different loading rates was dynamically characterized by the crossed-polarized optical measurement. A light source, a polarizer, a specimen stretched by the Instron universal testing machine, an analyzer with the polarization perpendicular to the polarizer, and a camera were set up in the order as shown in Figure 2.2a. The appearance change of the specimen under uniaxial tension was recorded by a Canon EOS 6D DSLR camera per 1% strain simultaneously with the measured stress-strain relation. The recorded images were used to measure the transmitted light intensity by ImageJ. Because the dramatic change of specimen thickness under large stretching can alter the measurement of brightness, we recorded the transmitted light intensity for different orientations of the crossed-polarizers by rotating them every 10° to determine the director as a function of stretch. Since the director $\mathbf{d}$ is symmetric ($\mathbf{d} = -\mathbf{d}$) and the initial director is known, the light intensity is cycled every 90°. Therefore, we can calculate director rotation by only measuring the transmitted light at different angles between the polarizer and the tension direction, φ, from 0° to 90°. The

measured transmitted intensity I for different φ (Figure 2.2a), can be fitted by the following equation to determine the director,

$$I = I_0 Sin^2\left(\frac{b\pi(90°-\varphi-\theta)}{180}\right) + d, \quad (2.1)$$

where $I_0, b, \theta,$ and d are fitting parameters. In particular, the parameter θ represents the current director. Figure 2.2b shows one example of the measured transmitted intensity as a function of angle φ and the fitting curve based on eqn (2.1) at zero strain. The curve fits the experimental data well. The φ value at the lowest intensity corresponds to the polarizer parallel or perpendicular to the director, and the φ value at the highest intensity corresponds to the polarizer 45° away from the director. Figure 2.2c shows the appearance of an MNE-90 specimen with different φ angles. When $\varphi = 0°$ or 90°, the specimen looks darkest, while when $\varphi = 45°$, the specimen looks brightest. We similarly measured the director for different LCE specimens as a function of stretch under different loading rates of 0.1%/s, 1%/s, and 10%/s.

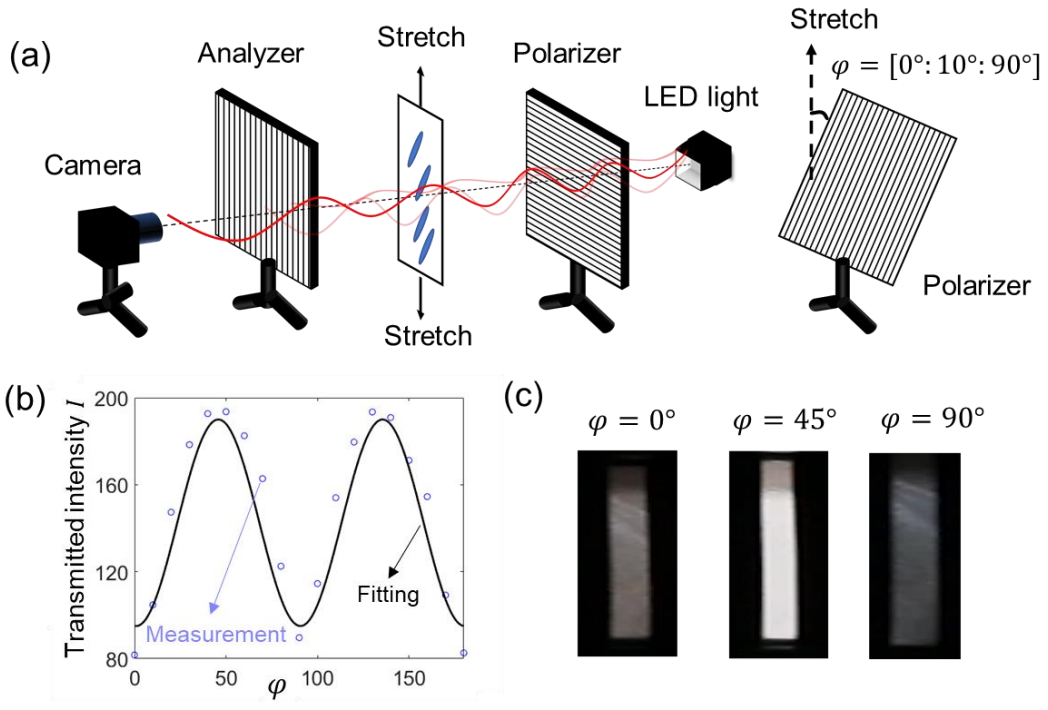

Figure 2.2 (a) Schematics of the setup of the crossed-polarized optical measurement for directors. (b) The transmitted intensity I was measured as a function of the angle between the polarizer and the tension direction, φ, and fitted by eqn (2.1) to determine the director θ. (c) The appearance of an MNE-90 specimen showing different brightness was captured by a camera with different angles $\varphi = 0°$, $45°$, and $90°$.

2.2.4 Digital Image Correlation (DIC)

Attributed to director reorientation, LCEs can experience shear strain even under uniaxial external tension. Here we use the 2D digital image correlation (DIC) method to measure all the strain components in the middle region of specimens at different loading rates. To generate a high-quality pattern, Koh-I-Noor Rapidraw ink, which dries fast and has a dark color, was sprayed using a Gocheer airbrush, which generates small droplets, at 30 psi with a 0.3 mm nozzle. The changes of the speckle patterns under deformation were recorded as videos by a Canon EOS 6D DSLR camera along with a Canon 100mm F/2.8L macro lens. The videos were set at 30 frames per second (fps). To enhance the optical contrast, a whiteboard was used as a background, and a white LED light was shot on the sample. Figure 2.3a presents an example of an MNE-45 specimen with speckle patterns in the undeformed (left) and stretched (right) states. After testing, videos were converted to images by the open-source software FFmpeg, with an imaging rate of 2 fps, 0.5 fps, and 0.2 fps for loading rates of 10%/s, 1%/s, and 0.1%/s, respectively. The images were then read by an open-source 2D DIC Matlab software, Ncorr,[76] to calculate the deformation gradient $\boldsymbol{F}$. We selected the middle part of a specimen as the region of interest (ROI) and set the image of the undeformed sample as the reference image. Here, we set the three critical parameters which can affect the results as the following: subset radius as 25,

subset spacing as 3, and strain radius as 20. More details are available in the instruction manual (http://www.ncorr.com/). Figure 2.3b shows the distributions of the components of the deformation gradient calculated by Ncorr for the MNE-45 specimen at 100% external strain in the x_2 direction at the loading rate of 1%/s. The deformation gradient $\boldsymbol{F}$ under uniaxial tension could be written as:

$$\boldsymbol{F} = \begin{bmatrix} \lambda_{11} & \lambda_{12} & 0 \\ \lambda_{21} & \lambda_{22} & 0 \\ 0 & 0 & \lambda_{33} \end{bmatrix}, \quad (2.2)$$

where λ_{22} is the normal component in the stretch direction, λ_{21} is the shear deformation, λ_{11} and λ_{33} are the stretches in width and thickness. λ_{12} is almost zero during the test, so we could set it as zero. From Figure 2.3b, we could see that all the components exhibit uniform distributions in the middle part of the specimen. Therefore, we can calculate the median value of the selected region to represent the strain of the specimen and plot λ_{11}, λ_{21} and λ_{22} versus external stretch. When the initial director is tilted with the elongation direction, an obvious shear deformation is expected and observed (Figure 2.3b, 3c).

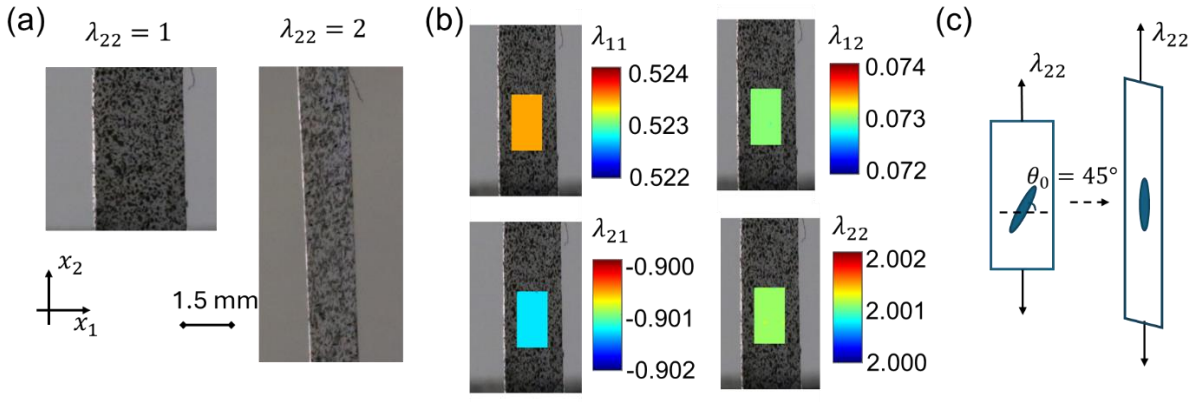

Figure 2.3 (a) Representative images of speckle patterns generated by spraying ink with an airbrush on an MNE-45 specimen in the undeformed ($\lambda_{22} = 1$) and deformed ($\lambda_{22} = 2$) states. (b) Distributions of the

components of the deformation gradient, λ_{11}, λ_{12}, λ_{21} and λ_{22}, using the DIC method in the MNE-45 specimen under an external tensile stretch $\lambda_{22} = 2$ at the loading rate of 1%/s. (c) the schematic of deformation of the MNE-45 specimen under uniaxial tension based on the DIC results.

2.2.5 Relaxation Tests

To characterize the reduction of stress and evolution of directors of LCEs during relaxation, specimens were subjected to uniaxial stretch performed in the same apparatus as described in sections 2.2.2 and 2.2.3. Specimens MNE-90, MNE-60, MNE-45, and MNE-30 were stretched to a fixed strain, $\varepsilon_0 = 30\%, 50\%, 70\%$, and 100%, respectively, at a very high loading rate of 267%/s. The specimens were then held for 3600 seconds, and the stress and director rotation were recorded as functions of time by an Instron universal testing machine and the crossed-polarized optical measurement, respectively. The applied strains are different for different specimens to observe significant director rotation and ensure that specimens would not break during the tests. As the loading rate is very fast, the stress oscillates at the very beginning. We counted the time t_0 as the end of loading when the oscillation dies out. t_0 is 0.40 s, 0.47 s, 0.56 s, and 0.74 s for specimens MNE-90, MNE-60, MNE-45, and MNE-30, respectively. The stress relaxation curves were fitted with a power law:

$$\sigma(t) = m_1 + m_2(t - t_0)^{-\beta}, \tag{2.3}$$

where *t* is the total experiment time, m_1, m_2 and β are fitting parameters. Based on the previous study,[41] β is about 0.4 for a main-chain smectic LCE. We used the nonlinear least-squares solver (lsqcurvefit) in Matlab to fit the experimental results and set $\beta = 0.4$ as the initial value.

2.3 Experimental Results

2.3.1 Rate-dependent Director-stress-strain Relationship

The uniaxial loading-unloading nominal stress-strain curves for LCE specimens with different initial directors under different loading rates, 10%/s, 1%/s, and 0.1%/s, are shown in Figure 2.4. The corresponding director-strain relations during loading are shown in Figure 2.5. In general, the prepared samples show birefringence, indicating they are monodomain, and the measured initial director is close to the design. For MNE-90, the director does not rotate with strain independent of the loading rates (Figure 2.5a). Consequently, the stress-strain loading curves are similar to those of classical neo-Hookean materials. When the initial director is oblique to the elongation direction, as in MNE-60, MNE-45, and MNE-30, the director gradually rotates as the strain increases, and eventually approaches the elongation direction when the strain is high enough (Figure 2.5b, c, and d). As a result, the director rotation produces high spontaneous strain and stress plateau in the stress-stretch relation, where the stress increases a little while the strain increases a lot (Figure 2.4b, c and d). For a LCE with a higher initial director angle θ_0, the nominal stress is lower at a given level of strain, and the specimen can survive a higher stretch due to the spontaneous strain.

All the specimens exhibit rate-dependent stress and director responses. Since the area between a loading and an unloading stress-strain curve represents dissipation energy, our results show that the specimens do not reach equilibrium even at 0.1%/s (Figure 2.4). A higher loading rate leads to higher nominal stress and higher dissipation. For MNE-90, where no director rotation occurs, the stress-strain curve is highly rate-dependent and hysteretic, suggesting a highly viscous network extension. For LCEs with initial directors oblique to stretching (MNE-

60, MNE-45, MNE-30), directors show rate-dependent rotation from the initial angles to the elongation direction ($\theta = 90°$). At a higher loading rate, the directors rotate less at a given strain, showing delayed behavior due to a shorter response time.

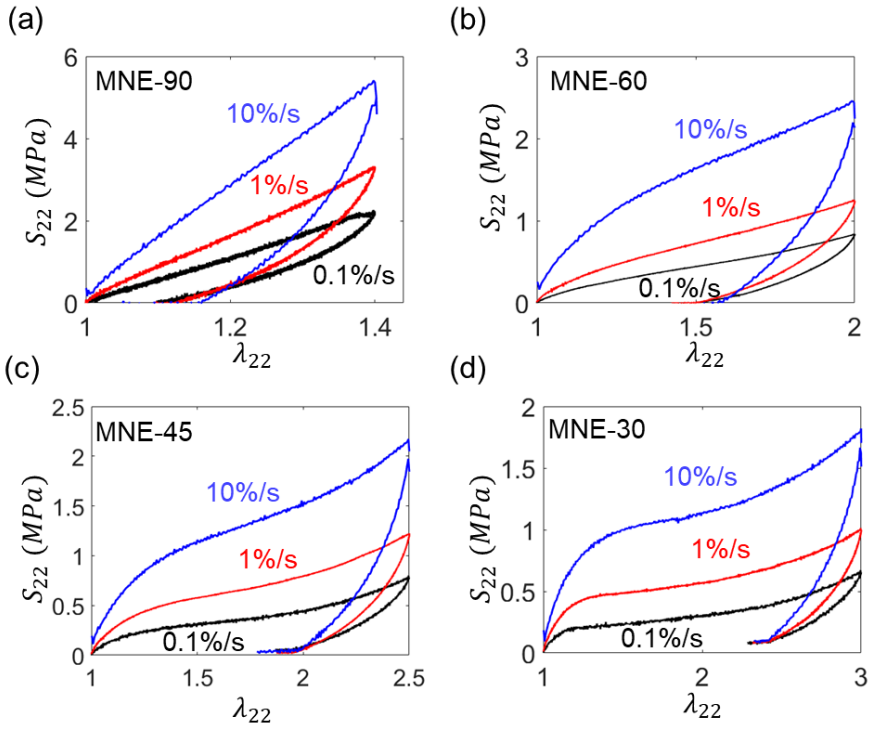

Figure 2.4 Loading and unloading nominal stress (S_{22}) as a function of the applied external stretch (λ_{22}) for specimens (a) MNE-90, (b) MNE-60, (c) MNE-45, and (d) MNE-30 under uniaxial tension at loading and unloading rates of 10%/s, 1%/s, and 0.1%/s.

From Figure 2.4 and Figure 2.5, it is obvious that there is a strong relationship between director rotation and stress responses. From MNE-45 and MNE-30, we could observe the stress-strain curves show three regimes: 1) when the stretch λ_{22} is small, the stress is neo-Hookean-like; 2) as the sample is stretched more, the director rotates more, and a stress plateau occurs; 3) when the director approaches the elongation direction, the stress-strain curve becomes stiffened again. The stress plateau is caused by spontaneous deformation due to director rotation

elaborated by previous studies [24,29,31]. As we have shown the rate-dependent director in Figure 2.5, it is expected to observe a rate-dependent stress plateau. When a fast loading at 10%/s is applied, the director rotation is delayed, so the sample's deformation is mainly accommodated by network extension. When a slow loading at 0.1%/s is applied, the director rotates more, so the stress plateau is wider and occurs at a lower strain level. In section 2.3.3, we will further distinguish the contributions of the director and the network viscosity by stress relaxation tests.

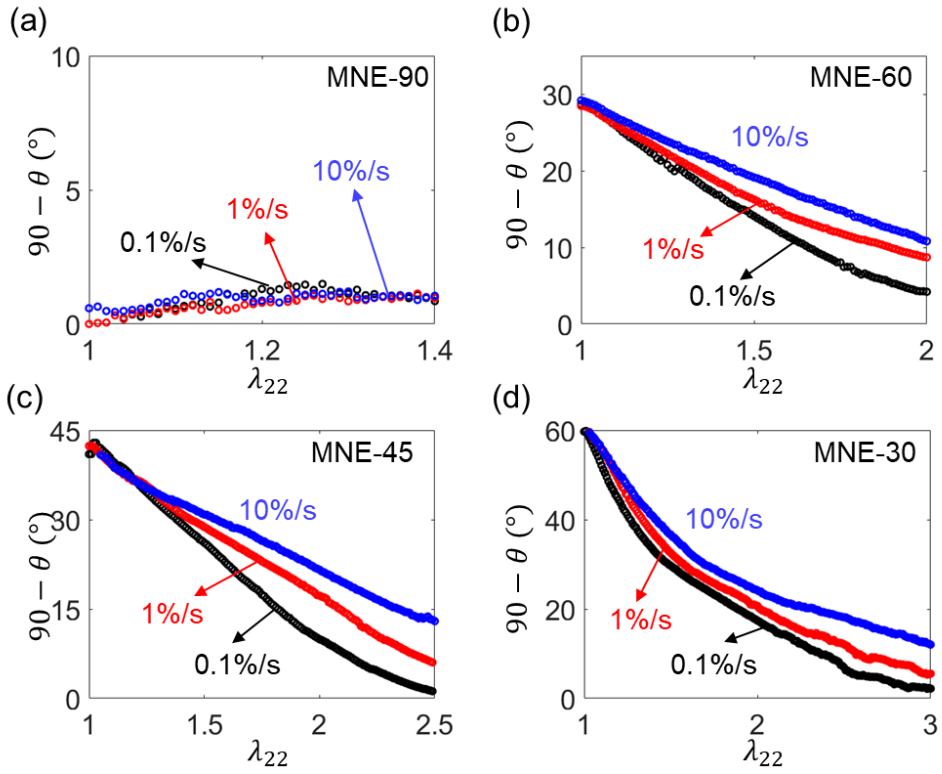

Figure 2.5 Director reorientation as a function of the applied external stretch λ_{22} at loading rates 10%/s, 1%/s, and 0.1%/s for (a) MNE-90, (b) MNE-60, (c) MNE-45, and (d) MNE-30, respectively.

2.3.2 DIC Measurement

The rate-dependent strain fields of LCEs were measured by DIC. The median value of the strain components λ_{11}, λ_{21} and λ_{22} were calculated by Ncorr. Figure 2.6 shows λ_{11}, λ_{22}, and λ_{21}

of MNE-60, MNE-45, and MNE-30 measured from DIC at loading rates of 10%/s, 1%/s, and 0.1%/s. Figure 2.6b, e, and h plot the axial stretch λ_{22} measured by DIC versus λ_{22} prescribed by the Instron. Their values are very close (grey dashed curve) for all different loading rates and initial directors, verifying the accuracy of the DIC method.

The transverse stretch λ_{11} measured for MNE-60, MNE-45, and MNE-30 is rate-dependent (Figure 2.6a, d, and g). When the loading rate is higher, as mentioned in section 2.3.1, the director rotates less, leading to lower spontaneous deformation. As a result, LCEs behave more like traditional incompressible elastomers. The stress state is closer to the uniaxial state, which satisfies $\lambda_{11} = \lambda_{33} = 1/\sqrt{\lambda_{22}}$ (grey soild lines in Figure 2.6a, d, and g). We could see that the measured λ_{11} under fast loadings (blue curves) is closer to that of the uniaxial (plane stress) condition. When the loading rate is low, the spontaneous strain caused by director rotation dominates the deformation. As the director rotation mainly occurs in the $x_1 - x_2$ plane of the specimens [29], the deformation is close to a plane strain condition ($\lambda_{11} = 1/\lambda_{22}$, $\lambda_{33} = 1$, grey dashed lines in Figure 2.6a, d, and g). Our results indeed show that the measured λ_{11} under slow loadings (black curves) is closer to that of the plane strain case. Moreover, since a higher initial director angle θ_0 corresponds to less director rotation, λ_{11} of MNE-60 is closest to that of the uniaxial condition among the three cases under the same loading condition, while MNE-30 is closest to that of the plane strain condition.

Figure 2.6c, f, and i show the measured shear deformation λ_{21} as a function of the external stretch λ_{22}. Different from traditional elastomers, LCEs exhibit considerable shear strain under uniaxial tension due to the director rotation. As the director is rate-dependent, it is not surprising to see the rate-dependent shear strain. For MNE-60 and MNE-45, the absolute value

of λ_{21} monotonically increases with λ_{22}, exhibiting large shear strain (~-1.4 for MNE-60 and ~-1.6 for MNE-45) when the director rotates almost parallel to the stretching direction ($\lambda_{22} = 2$ for MNE-60 and $\lambda_{22} = 2.5$ for MNE-45) at the loading rate of 0.1%/s. For MNE-30, it is interesting to observe that λ_{21} non-monotonically changes with λ_{22}, i.e. at a small stretch, the shear strain first rises to be positive and then decreases with the stretch to a negative value. When the director rotates almost parallel to the stretching direction ($\lambda_{22} = 3$ at the loading rate of 0.1%/s), the shear strain is around -1.26. Such non-monotonic shearing has been predicted by theoretical modeling before [72,77]. When the external stretch λ_{22} is high, faster loading rates lead to lower shear strain for all different directors due to a delay in director rotation.

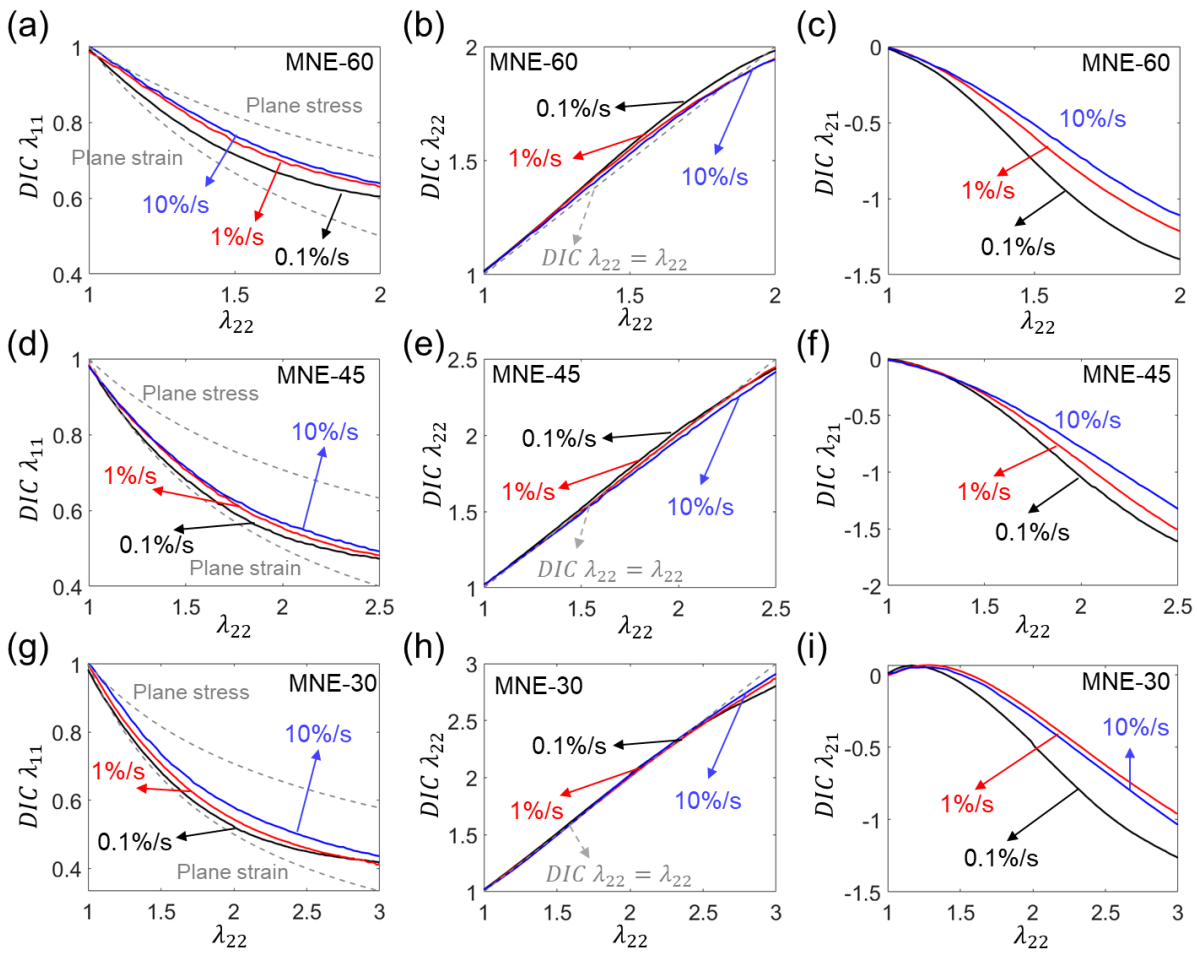

Figure 2.6 Components of the deformation gradient, λ_{11}, λ_{22}, and λ_{21}, measured by the DIC method as functions of the applied external stretch λ_{22} at different loading rates of 10%/s, 1%/s, and 0.1%/s for specimens (a)(d)(g) MNE-60, (b)(e)(h) MNE-45, and (c)(f)(i) MNE-30, respectively.

2.3.3 Relaxation Test

The stress relaxation of viscoelastic LCEs has been documented for many years [37,39,41]. Compared to traditional elastomers, LCEs show more complex relaxation behavior due to the relaxation of both the director and the network, and their coupling effort. Here by applying a nearly instantaneous stretch, we characterize both the stress relaxation and director reorientation over time to distinguish the different characteristic time scales of the network extension and director rotation.

Figure 2.7 shows the stress relaxation of MNE-90, where the director hardly rotates. The specimen was stretched to 30% strain nearly instantaneously in a short time period t_0 and held for 3600 s. The stress was measured as a function of the total experimental time t. The relaxation of stress shows two distinct relaxation regimes and can be fitted by two different power laws as shown in eqn (2.3). At the early stage ($t < 1.5s$), the power law with an exponent around 0.14 fits the experimental data well, while at the long term ($t > 1.5s$), relaxation follows a power law with an exponent around 0.40. The long-term exponent is similar to the one previously reported for main-chain smectic polydomain LCEs [41]. At a short time, the stress does not match the long-time fitting curve, which may be caused by slight director rotation since mesogens may not align perfectly with the stretching direction.

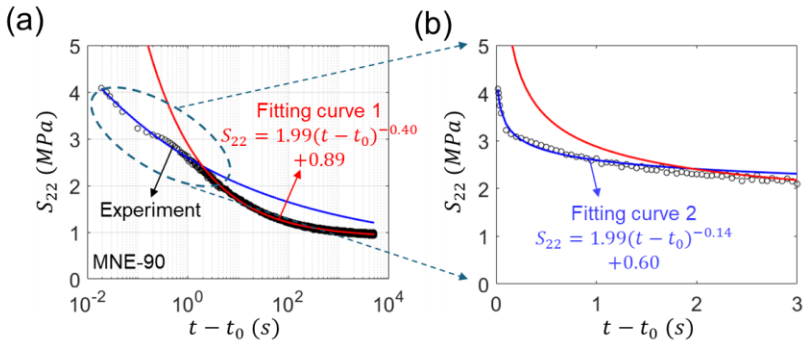

Figure 2.7 Stress relaxation of MNE-90. (a) Stress S_{22} as a function of the relaxation time $t - t_0$, where t represents the total experimental time, and t_0 represents the short loading period. Two power laws are utilized to fit the experimental data: a power law with an exponent 0.14 for the experimental data before t =1.5s, and a second power law with an exponent 0.40 for the experimental data after t =1.5s. (b) Zoom-in relation of S_{22} and $t - t_0$ within the first 3 seconds.

Figure 2.8 shows the relaxation of stress (Figure 2.8a-c) and directors (Figure 2.8d-i) for MNE-60, MNE-45, and MNE-30. The specimens were stretched to different fixed strains, 50%, 70%, and 100%, respectively, to ensure significant director rotation but no fracture during a test. Then the specimens were held for 3600 s, and the stress and directors were recorded over time. Stress relaxation could be divided into two parts. Compared to MNE-90, the stress relaxation in LCEs with a tilted director with respect to the stretching is more complicated at the early stage ($t < 1.5\ s$), as stress relaxation is a synergy of the director reorientation, the backbone orientation, and the polymer chain sliding. As Figure 2.8g-i show, the director has already rotated a lot by the time the loading is completed ($t = t_0$). At the stage $t_0 < t < 1.5s$, MNE-60, MNE-45 and MNE-30, particularly MNE-30, show a the sharp drop in stress (Figure 2.8a-c), caused by the spontaneous strain due to director rotation. When $t > 1.5s$, the director rotates smoothly, and the stress relaxation can be fitted by a power law well with a power exponent around 0.4 for

all the samples, which behaves similarly to MNE-90. This suggests that after $t > 1.5s$, stress relaxation is dominated by the network viscosity. The further relaxation of the director after $t > 1.5s$ may be due to the further extension of the network. As mesogens locate on the backbone, the network slow extension can drag the mesogens to further realign to the stretching direction. Furthermore, it is coincident that the director relaxation could be fitted well with the same power law formula $\theta = m_1 + 20(t - t_0)^{-\beta}$ of stress relaxation (eqn (2.3)), but with a much smaller power exponent around 0.04 (Figure 2.8d-f).

To probe the characteristic times of the network relaxation and director rotation, we compare the director and stress values from the uniaxial tension tests at different rates and the relaxation tests. We choose some representative cases in Table 2.1 and Table 2.2.

In Table 2.1, we listed the relative directors $(90 - \theta)$ measured for MNE-60 at 50% uniaxial strain, for MNE-45 at 70% strain, and for MNE-30 at 100% strain at the loading rates of 10%/s (1st column), 1%/s (3rd column), and 0.1%/s (5th column). In 2nd, 4th, and 6th columns, we compared them with the directors measured from the relaxation tests for MNE-60, MNE-45, and MNE-30 at the relaxation time equal to the time needed to load the specimens to the corresponding strain in the uniaxial tests. If the directors from the uniaxial tension tests equal or approach those from the relaxation, this means the director rotation reaches equilibrium at that loading rate. We find that the directors measured from the uniaxial tension tests at 1%/s are close to those from the relaxation tests, and the directors measured from the uniaxial tension tests at 0.1%/s are almost the same as those from the relaxation tests (Table 2.1). To be more specific, taking MNE-60 as an example, the relative director is about 19.1° under 50% strain at the rate of 10%/s, while the relative director reaches around 16.8° when relaxing for 5 s in the relaxation

test; the relative director is about 16.3° under 50% strain at the rate of 1%/s, while the relative director reaches around 15.3° when relaxing for 50 s in the relaxation test; the relative director is about 14.1° under 50% strain at the rate of 0.1%/s, while the relative director reaches around 13.9° when relaxing for 500 s. Allowing $\pm 1°$ natural error, the results suggest mesogen reorientation approaches equilibrium at 1%/s and has already reached equilibrium at 0.1%/s.

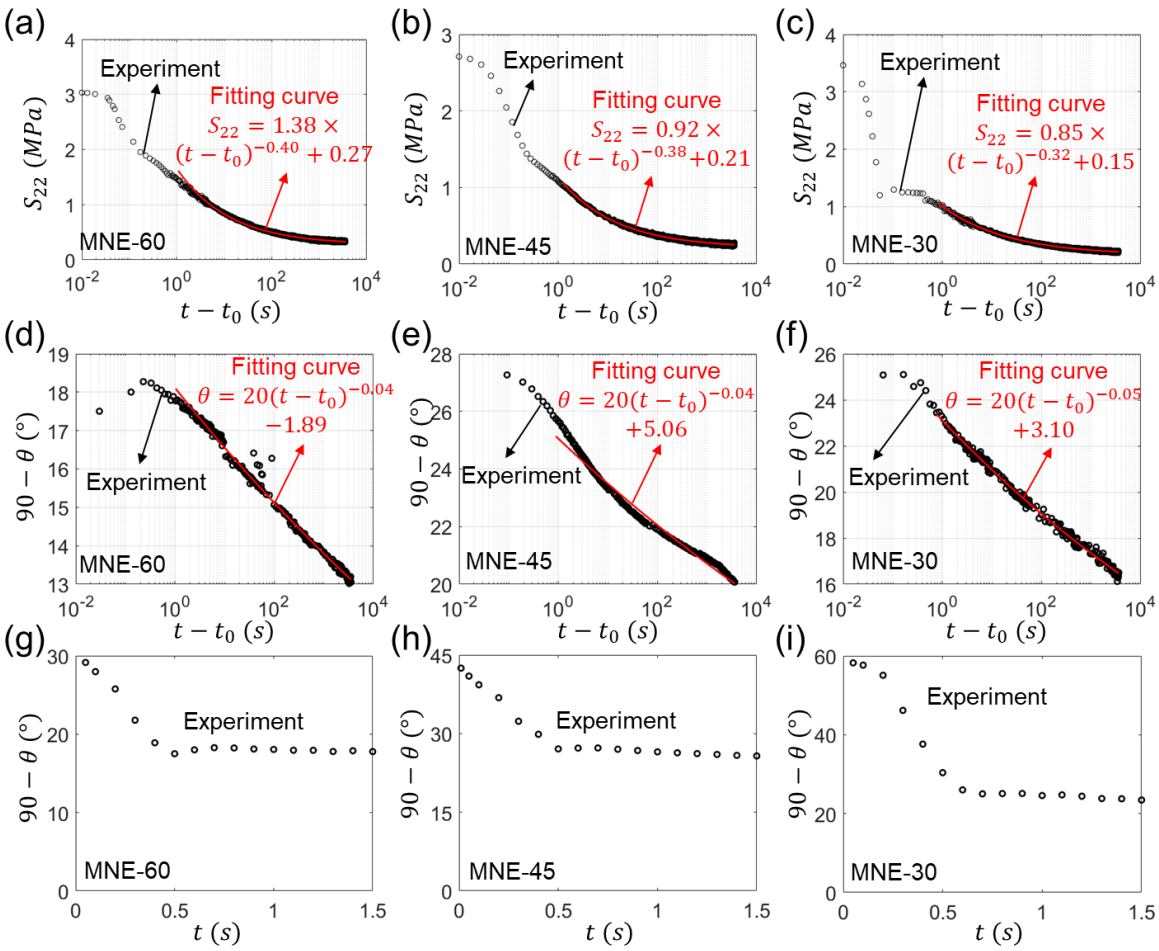

Figure 2.8 Stress and director relaxation as functions of time for MNE-60, MNE-45, and MNE-30. Power laws with exponents 0.40, 0.38 and 0.32 fit well the stress relaxation results after $t = 1.5s$ for (a) MNE-60, (b) MNE-45, and (c) MNE-30, respectively. The director relaxation with power laws of exponents 0.04, 0.04 and 0.05 fit well the director relaxation results after $t = 1.5s$ for (d) MNE-60, (e) MNE-45,

and (f) MNE-30. The director relaxation within 1.5s for (g) MNE-60, (h) MNE-45, and (i) MNE-30. For the relaxation tests, MNE-60, MNE-45, and MNE-30 were stretched to 30%, 70%, and 100% strain, respectively, and held for 3600s.

Table 2.1 The director ($90° - \theta$) measured from the uniaxial tension tests and relaxation tests (unit: degree)

	Uniaxial tests at 10%/s under 50%, 70% and 100%	Relaxation tests at 5s, 7s and 10s	Uniaxial tests at 1%/s under 50%, 70% and 100%	Relaxation tests at 50s, 70s and 100s	Uniaxial tests at 0.1%/s under 50%, 70% and 100%	Relaxation tests at 500s, 700s and 1000s
MNE-60	19.1	16.8	16.3	15.3	14.1	13.9
MNE-45	26.4	23.8	24.2	22	19.1	20.9
MNE-30	24.2	21.1	20.7	19.0	17.4	17.3

Table 2.2 The stress measured from the uniaxial tension tests and relaxation tests (unit: MPa)

	Uniaxial tests at 10%/s under 30%, 50%, 70% and 100%	Relaxation tests at 3s, 5s, 7s and 10s	Uniaxial tests at 1%/s under 30%, 50%, 70% and 100%	Relaxation tests at 30s, 50s, 70s and 100s	Uniaxial tests at 0.1%/s under 30%, 50%, 70% and 100%	Relaxation tests at 300s, 500s, 700s and 1000s
MNE-90	4.11	2.20	2.41	1.44	1.66	1.10
MNE-60	1.63	1.07	0.77	0.57	0.45	0.38
MNE-45	1.29	0.66	0.65	0.40	0.36	0.28
MNE-30	1.13	0.58	0.57	0.35	0.30	0.24

In Table 2.2, we listed the stress measured for MNE-90 at 30% uniaxial strain, for MNE-60 at 50% strain, for MNE-45 at 70% strain, and for MNE-30 at 100% strain at the loading rates of 10%/s (1st column), 1%/s (3rd column), and 0.1%/s (5th column). Similarly, in the 2nd, 4th, and 6th columns, we compared them with the stress measured from the relaxation tests at the corresponding relaxation time. As a result, the stress values measured from the uniaxial tension tests are much higher than those in the corresponding relaxation tests for all specimens at all rates, which means the material is far away from the equilibrium state. Taking MNE-60 as an example, the stress is about 1.63 MPa under 30% strain at the rate of 10%/s, 0.77 MPa at the rate of 1%/s, and 0.45 MPa at the rate of 0.1%/s, while the stress is around 1.07, 0.57 MPa and 0.38

when the specimens are relaxed for 3 s, 30 s and 300 s, respectively, in the relaxation tests. As we have discussed that the director almost reaches equilibrium at 0.1%/s, we could conclude that the viscosity at slow loading is due to the reorganization of the viscoelastic network. And the director relaxes at least two orders of magnitude faster than the network.

In general, based on the relaxation of the director and stress, we can see that the relaxation time of the network is much larger than that of directors, and the long-time stress relaxation ($t > 1.5\ s$) is mainly attributed to the reorganization of the viscoelastic network. However, since the mesogens are on the main chains of the polymer network, the relaxation is the synergy of the director and network. On one hand, the fast-responsive director rotation causes fast macroscopic deformation, leading to a sharp stress drop at the early stage of stress relaxation. On the other hand, the slowly relaxed network extension further facilitates the director alignment at a long relaxation time.

2.4 Theoretical Model

LCEs show unique stress behavior distinct from traditional elastomers mainly due to mesogen alignment and director rotation. Recently, some viscoelastic models have been developed to describe the rate-dependent stress and director of LCEs subjected to external stretching [72,74]. Here, following the work of Wang *et al*,[74] we will establish a viscoelastic model for LCEs based on multiplicative decomposition, which is widely used for modeling viscoelastic elastomers [74,78]. The viscoelastic constitutive model assumes the elastic energy as the sum of the neo-classical free energy and the semi-soft energy [24,79–81], but only considers the viscosity of the network. After fitting our experimental results, the model will be used to manifest the relation between rate-dependent macroscopic deformation and microscopic director rotation.

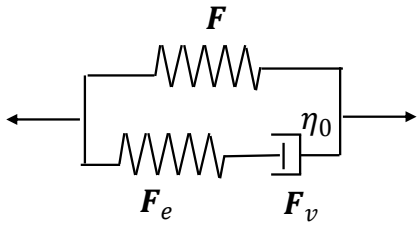

Figure 2.9 Rheological model for the viscoelasticity of LCEs

2.4.1 A General Continuum Viscoelastic Model for LCEs

Consider a material particle in a body in the reference configuration labeled by its position vector **X**. It moves to position **x** at time t in the current configuration. The deformation gradient is defined as $F_{iK} = \partial x_i(\mathbf{X}, t)/\partial X_K$. The rheological model is composed in parallel of an equilibrium spring, representing the elasticity after viscoelastic relaxation, and a Maxwell unit with a non-equilibrium spring and a dashpot connected in series, describing non-equilibrium behavior (Figure 2.9). In the Maxwell unit, we assume the total deformation gradient $\boldsymbol{F}$ can be decomposed into an elastic part $\boldsymbol{F}_e$ and a viscoelastic part $\boldsymbol{F}_v$, $\boldsymbol{F} = \boldsymbol{F}_e\boldsymbol{F}_v$. Based on the experiments in sections 2.2 and 2.3, we know that the viscosity of the director rotation is much smaller than that of the network, so we could assume the viscosity is mainly from the network. Thus, the dashpot in the rheological model in Figure 2.9 represents the viscous behavior of the network. Here we assume the free energy density in the reference state f_r is a function of the deformation gradient $\boldsymbol{F}$, the elastic part $\boldsymbol{F}_e$, and director $\boldsymbol{d}$, $f_r = f_r(\boldsymbol{F}, \boldsymbol{F}_e, \boldsymbol{d})$. According to the free energy imbalance for the isothermal condition, we can write the nonequilibrium thermodynamics requirement as

$$\int -\dot{f}_r dV + \int \boldsymbol{B}\dot{\boldsymbol{u}}\, dV + \int \boldsymbol{T}\dot{\boldsymbol{u}}\, dA + \int \gamma_d \boldsymbol{d}\cdot\dot{\boldsymbol{d}}\, dV \geq 0, \tag{2.4}$$

where $\dot{}$ in $\dot{f}_r$, $\dot{\boldsymbol{u}}$ and $\dot{\boldsymbol{d}}$ represents a small variation over a small time increment, $\dot{} = \delta/\delta t$, the volume element dV and area element dA are both defined in the reference configuration; the body force and traction do work at the rate $\int \boldsymbol{B}\dot{\boldsymbol{u}}\, dV + \int \boldsymbol{T}\dot{\boldsymbol{u}}\, dA$; γ_d is a Lagrange multiplier to enforce the unit vector constraint of $\boldsymbol{d}$, $\boldsymbol{d}\cdot\boldsymbol{d} \equiv 1$. Using the relation $\dot{f}_r = \frac{\partial f_r}{\partial \boldsymbol{F}} : \dot{\boldsymbol{F}} + \frac{\partial f_r}{\partial \boldsymbol{F}_e} : \dot{\boldsymbol{F}}_e + \frac{\partial f_r}{\partial \boldsymbol{d}} \cdot \dot{\boldsymbol{d}}$, we could further expand the inequality eqn (2.4) in the following manner

$$\int (\boldsymbol{B} + div_X(\boldsymbol{S}))\dot{\boldsymbol{u}} dV + \int (-\boldsymbol{S}\cdot\boldsymbol{N} + \boldsymbol{T})\dot{\boldsymbol{u}} dA + \int (\gamma_d \boldsymbol{d} - \frac{\partial f_r}{\partial \boldsymbol{d}})\dot{\boldsymbol{d}} dV + \int \frac{\partial f_r}{\partial \boldsymbol{F}_e} : \boldsymbol{F}_e \boldsymbol{L}^{\boldsymbol{v}} dV \geq 0, \quad (2.5)$$

where $\boldsymbol{L}^{\boldsymbol{v}} = \dot{\boldsymbol{F}}_{\boldsymbol{v}} \boldsymbol{F}_{\boldsymbol{v}}^{-\mathbf{1}}$, $\boldsymbol{N}$ is the unit vector normal to any given surface at the reference state, $\mathbf{S} = \frac{\partial f_r}{\partial \boldsymbol{F}} + \frac{\partial f_r}{\partial \boldsymbol{F}_e} \boldsymbol{F}_v^{-T}$ is the first Piola-Kirchhoff stress. The inequality should always be satisfied, requiring each of the above terms to be positive or equal to zero due to the independency of $\dot{\boldsymbol{u}}$, $\dot{\boldsymbol{d}}$ and $\dot{\boldsymbol{F}}_{\boldsymbol{e}}$ (and therefore $\dot{\boldsymbol{F}}_{\boldsymbol{v}}$).

Then we can get the force balance equation and traction relation from the first two terms:

$$\boldsymbol{B} + div_X(\boldsymbol{S}) = \mathbf{0}, \quad (2.6)$$

$$-\boldsymbol{S}\cdot\boldsymbol{N} + \boldsymbol{T} = \mathbf{0}. \quad (2.7)$$

The third term in eqn (2.5) indicates that $\frac{\partial f_r}{\partial \boldsymbol{d}}$ should be in the same direction as $\boldsymbol{d}$, requiring that

$$\boldsymbol{d} \times \frac{\partial f_r}{\partial \boldsymbol{d}} = \mathbf{0}, \quad (2.8)$$

which is a governing equation for the director field, equivalent to the balance of rotational momentum derived in previous work [82]. To satisfy the non-negative requirement of the last term in eqn (2.5), we propose a simple evolution equation for $\boldsymbol{L}^{\boldsymbol{v}}$

$$\boldsymbol{L^v} = \frac{1}{\eta_0}\boldsymbol{F}_e^T\frac{\partial f_r}{\partial \boldsymbol{F}_e}. \quad (2.9)$$

Solving the above force balance equation together with the boundary condition eqn (2.6)-(7), the constitutive equation for the director eqn (2.8), and the evolution equation for $\boldsymbol{L^v}$ eqn (2.9), we can determine the viscoelastic stress-director-strain behavior of LCEs under arbitrary inhomogeneous deformation.

Next, we assume the free energy of LCEs includes the synergetic work of the director rotation and network extension. We employed the free energy as the summation of the equilibrium and nonequilibrium parts based on the neo-classical theory including the semi-soft elasticity [24,51,83], $f_r = f_r^{eq} + f_r^{neq}$, with

$$f_r^{eq} = \frac{\mu^{eq}}{2} tr\left(\boldsymbol{F}^{eq}\boldsymbol{F}^{eq^T} + a(\boldsymbol{I} - \boldsymbol{d_0}\otimes\boldsymbol{d_0})\boldsymbol{F^T}\cdot\boldsymbol{d}\otimes\mathbf{d}\cdot\mathbf{F}\right) - p(J-1), \quad (2.10)$$

$$f_r^{neq} = \frac{\mu^{neq}}{2} tr\left(\boldsymbol{F}^{neq}\boldsymbol{F}^{neq^T} + a(\boldsymbol{I} - \boldsymbol{d_0}\otimes\boldsymbol{d_0})\boldsymbol{F}_e{}^{\boldsymbol{T}}\cdot\boldsymbol{d}\otimes\mathbf{d}\cdot\boldsymbol{F}_e\right) - \mu^{neq}\ln(J^e), \quad (2.11)$$

where μ^{eq} and μ^{neq} are the shear modulus of the equilibrium and non-equilibrium; p is the Lagrange multiplier to incorporate the incompressibility $J = \det(F) = 1;\ J^e = \det(\boldsymbol{F}_e)$; $\boldsymbol{F}^{eq} \coloneqq \boldsymbol{l}^{-1/2}\boldsymbol{F}\boldsymbol{l_0}^{1/2}$; $\boldsymbol{F}^{neq} \coloneqq \boldsymbol{l}^{-1/2}\boldsymbol{F}_e\boldsymbol{l_0}^{1/2}$; a represents the semi-soft parameter, the value of which is kept the same for the equilibrium and non-equilibrium free energy; $\boldsymbol{d}$ and $\boldsymbol{d_0}$ represent the director in the current and reference states, respectively. $\boldsymbol{l}$ and $\boldsymbol{l_0}$ are the corresponding dimensionless shape (metric) tensor, $\boldsymbol{l} = \frac{1}{l_\parallel}((l_\parallel - l_\perp)\boldsymbol{d}\otimes\boldsymbol{d} + l_\perp\boldsymbol{I})$ and $\boldsymbol{l_0} = \frac{1}{l_\parallel^0}\left(\left(l_\parallel^0 - l_\perp^0\right)\boldsymbol{d_0}\otimes\boldsymbol{d_0} + l_\perp^0\boldsymbol{I}\right)$. The effective lengths along or perpendicular to the director ($l_\parallel\ and\ l_\perp$) are assumed to remain constant during deformation, and we can denote their ratio as

$$r \coloneqq \frac{l_\parallel}{l_\perp} = \frac{l_\parallel^0}{l_\perp^0}. \quad (2.12)$$

In the absence of non-equilibrium and with parameters $r = 1$ and $a = 0$, eqn (2.10) recovers the conventional neo-Hookean elastic energy. When $r \neq 1$, the backbone shows anisotropy owing to the presence of LCs by the free energy $\frac{\mu^{eq}}{2} tr\left(\boldsymbol{F}^{eq}\boldsymbol{F}^{eq^T}\right) = \frac{\mu^{eq}}{2} tr(\boldsymbol{l}^{-1}\boldsymbol{F}\boldsymbol{l_0}\boldsymbol{F}^{\boldsymbol{T}})$. The energy term could also be interpreted as the classical neo-Hookean elastic energy incorporating a deformation gradient $\boldsymbol{F}^{eq} = \boldsymbol{l}^{-1/2}\boldsymbol{F}\boldsymbol{l_0}^{1/2}$ from the isotropic phase of the reference configuration to the isotropic phase of the current configuration [77]. The energy term $\frac{\mu^{eq}}{2} tr(a(\boldsymbol{I} - \boldsymbol{d_0} \otimes \boldsymbol{d_0})\boldsymbol{F}^{\boldsymbol{T}} \cdot \boldsymbol{d} \otimes \mathbf{d} \cdot \mathbf{F})$ represents the semi-soft elasticity, describing fluctuation of chains with various anisotropy r. When $a = 0$, it implies the director can rotate with negligible stress; when $a > 0$, a stress threshold is required to initiate the rotation of the director. We can also rewrite the term as $\frac{\mu^{eq}}{2} a\|\boldsymbol{F}^{\boldsymbol{T}}\boldsymbol{d} - (\boldsymbol{F}^{\boldsymbol{T}}\boldsymbol{d} \cdot \boldsymbol{d_0})\boldsymbol{d_0}\|^2$, indicating that the energy vanishes when $\boldsymbol{F}^{\boldsymbol{T}}\boldsymbol{d}$ is parallel to $\boldsymbol{d_0}$.

Consider the homogeneous deformation of a thin LCE sample with a tilted director subjected to uniaxial stress in the x_2 direction, and we assume the director only rotates in the x_1-x_2 plane, i.e $\boldsymbol{d} = (\cos\theta\,, \sin\theta\,, 0)^T$.We can rewrite the first Piola-Kirchhoff stress, evolution equation for $\boldsymbol{L^v}$ eqn (2.9), and the constitutive equation for the director eqn (2.8) as

$$\boldsymbol{S} = \mu^{eq}\left(\left(\boldsymbol{l}^{-1}\boldsymbol{F}\boldsymbol{l_0}\right) + a\boldsymbol{d} \otimes (\boldsymbol{I} - \boldsymbol{d_0} \otimes \boldsymbol{d_0})\boldsymbol{F}^{\boldsymbol{T}}\mathbf{d}\right) + \mu^{neq}\left(\left(\boldsymbol{l}^{-1}\boldsymbol{F}_e\boldsymbol{l_0}\boldsymbol{F_e}^{\boldsymbol{T}}\boldsymbol{F}^{-\boldsymbol{T}}\right) + a\boldsymbol{d} \otimes (\boldsymbol{I} - \boldsymbol{d_0} \otimes \boldsymbol{d_0})\boldsymbol{F_e}^{\boldsymbol{T}}\mathbf{d}\boldsymbol{F_e}^{\boldsymbol{T}}\boldsymbol{F}^{-\boldsymbol{T}}\right) - Jp\boldsymbol{F}^{-\boldsymbol{T}} - \mu^{neq}\boldsymbol{F}^{-\boldsymbol{T}}, \quad (2.13)$$

$$\dot{\boldsymbol{F}}_{\boldsymbol{v}} = \frac{\mu^{neq}}{\eta_0}(\boldsymbol{F}_e^T\boldsymbol{l}^{-1}\boldsymbol{F}_e\boldsymbol{l_0} + a\boldsymbol{F}_e^T\boldsymbol{d} \otimes (\boldsymbol{I} - \boldsymbol{d_0} \otimes \boldsymbol{d_0})\boldsymbol{F}_e^T\mathbf{d} - \boldsymbol{I})\boldsymbol{F}_{\boldsymbol{v}}, \quad (2.14)$$

$$\boldsymbol{s}^{eqd} \times \boldsymbol{d} + \boldsymbol{s}^{neqd} \times \boldsymbol{d} = \mathbf{0}. \quad (2.15)$$

where $\boldsymbol{s}^{eqd} \coloneqq \mu^{eq}\left(\left(l_{\parallel}^{-1} - l_{\perp}^{-1}\right)\boldsymbol{F}\boldsymbol{l_0}\boldsymbol{F}^{\boldsymbol{T}}\boldsymbol{d} + a\boldsymbol{F}(\boldsymbol{I} - \boldsymbol{d_0} \otimes \boldsymbol{d_0})\boldsymbol{F}^{\boldsymbol{T}}\boldsymbol{d}\right)$ and $\boldsymbol{s}^{neqd} \coloneqq \mu^{neq}\left(\left(l_{\parallel}^{-1} - l_{\perp}^{-1}\right)\boldsymbol{F}_e\boldsymbol{l_0}\boldsymbol{F}_e{}^{\boldsymbol{T}}\boldsymbol{d} + a\boldsymbol{F}_e(\boldsymbol{I} - \boldsymbol{d_0} \otimes \boldsymbol{d_0})\boldsymbol{F}_e{}^{\boldsymbol{T}}\boldsymbol{d}\right)$. Since the deformation is homogeneous, the force balance equation eqn (2.6) is satisfied automatically. As discussed in section 2.2.4, the deformation gradient under uniaxial tension could be written as

$$\boldsymbol{F} = \begin{bmatrix} \lambda_{11} & 0 & 0 \\ \lambda_{21} & \lambda_{22} & 0 \\ 0 & 0 & \dfrac{1}{\lambda_{11}\lambda_{22}} \end{bmatrix}, \qquad (2.16)$$

where the shear strain λ_{21} exists due to director rotation; λ_{22} is the stretching direction. Also, we can assume the viscous part of the deformation gradient $\boldsymbol{F_v}$ as

$$\boldsymbol{F_v} = \begin{bmatrix} F_{v11} & F_{v12} & 0 \\ F_{v21} & F_{v22} & 0 \\ 0 & 0 & F_{v33} \end{bmatrix}. \qquad (2.17)$$

The elastic deformation gradient can be expressed as $\boldsymbol{F_e} = \boldsymbol{F}\boldsymbol{F_v}^{-\boldsymbol{1}}$. Inserting the expressions of $\boldsymbol{F}$, $\boldsymbol{F}_v$ ($\boldsymbol{F_e}$) and $\boldsymbol{d}$ into eqn (2.13) to (2.15), and using the condition $\boldsymbol{S} = diag(0, S_{22}, 0)$ for uniaxial tension, we numerically solve S_{22}, θ and all the components of $\boldsymbol{F}$ and $\boldsymbol{F}_v$ ($\boldsymbol{F_e}$) as functions of time with Matlab, where the Lagrange multiplier p is determined using $S_{33} = 0$.

2.4.2 Analysis of Uniaxial Tension

Here we study the director θ, shear strain λ_{21} and engineering stress S_{22} as functions of the normal stretch λ_{22} at different loading rates $\dot{\lambda_{22}}$. The viscoelastic model proposed in section 2.4.1 has five material parameters. As the viscoelastic relaxation is significant, we estimate $\mu^{neq}/\mu^{eq} = 9$ based on the stress relaxation test on MNE-90. The network viscosity $\eta_0/(\mu^{eq} + \mu^{neq}) = 1s$ and the semi-soft parameter $a = 0.08$ are selected to fit the director

reorientation and stress response from the uniaxial tension tests. The parameter $r = 5.5$ is calculated based on the following thermomechanical deformation test. We recorded the length of a monodomain LCE sample in the nematic configuration at room temperature as l_{nem}. Then we heated the specimen upto $130\,℃$, which is above the phase transition temperature T_{ni}, using a hotplate, and recorded the length in the isotropic configuration as l_{iso}. The macroscopic length change in response to the temperature change is purely due to the phase transition of LCs, correlating to the magnitude of the anisotropic backbone [24,29], and relates to r via:

$$r = (\frac{l_{nem}}{l_{iso}})^3. \qquad (2.18)$$

We measured l_{nem} and l_{iso} several times and took an average value to obtain $r = 5.5$. Analytical solutions of the uniaxial engineering stress S_{22} (Figure 2.10a-c), the director angle $90 - \theta$ (Figure 2.10d-f), and shear strain λ_{21} (Figure 2.10g-i) at different loading rates $\dot{\lambda_{22}} =$ 0.1%/s, 1%/s and 10%/s for different initial directors are plotted as functions of the normal stretch λ_{22}. Obvious rate-dependent stress, director rotation, and shear deformation are observed. At a low loading rate, the director rotates more, providing more spontaneous strain, and the stress caused by the viscosity of the network (the dashpot in Figure 2.9) is smaller. As a result, the stress is lower at a lower loading rate. Generally, the stress-strain behavior predicted by the model exhibits a consistent agreement with the experimental observations.

For all applied rates, the director approaches the stretching direction ($\theta = 90°$) as the normal stretch λ_{22} increases (Figure 2.10d-f). However, it is evident that the director rotation is slower at higher loading rates, exhibiting a noticeable delay. Although we only consider the network viscosity in the model, we still observe time-dependent director rotation due to the strong influence of the network on the director in main-chain LCEs. When a uniaxial stress

oblique to the initial director is applied, the director tends to rotate instantaneously, but the slow extension of the network can impede the director rotation. As a result, at a high loading rate, the network deforms less under a given normal stretch, constricting the director rotation, and causing a pronounced delay in director rotation. Conversely, at a low rate, as the network deforms more, the director also rotates more.

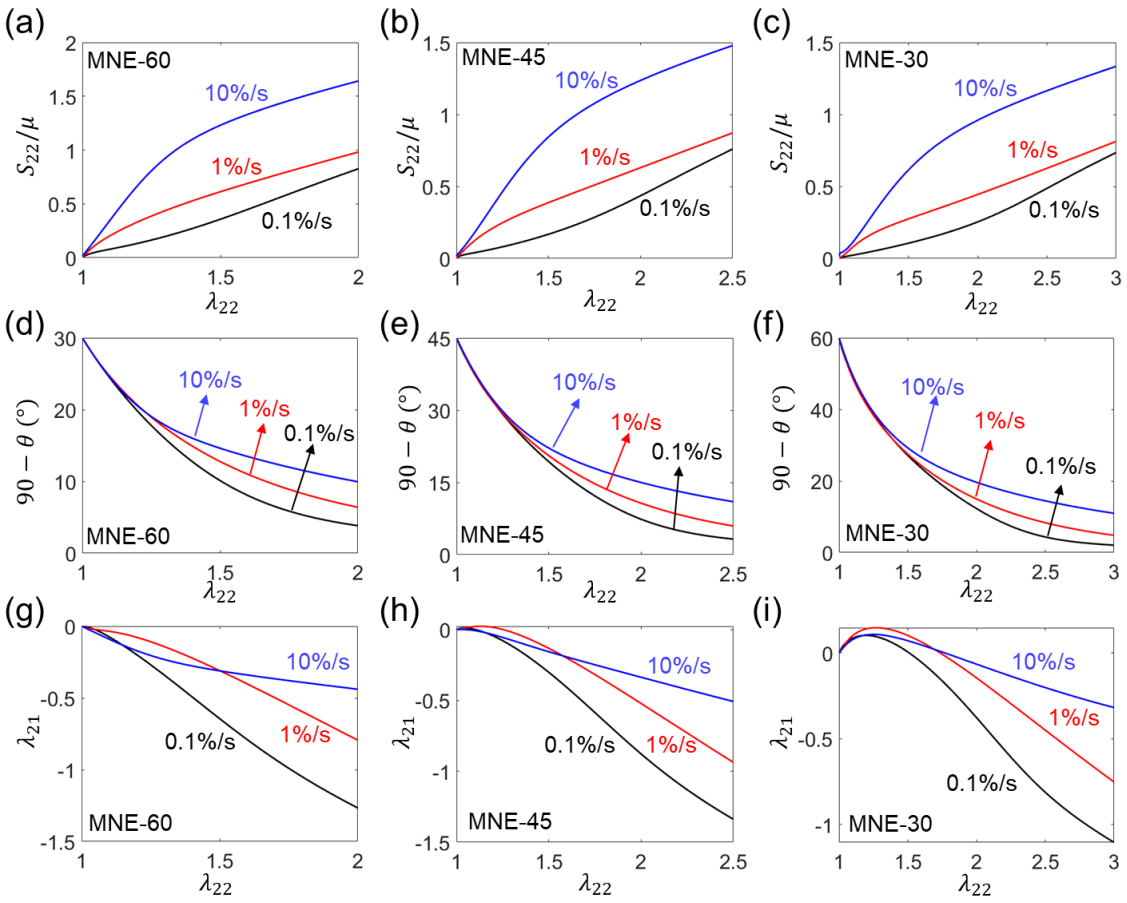

Figure 2.10 Analytical results of the (a)-(c) engineering stress S_{22}, (d)-(f) director angle $90-\theta$, and (g)-(i) shear strain λ_{21} as functions of the normal stretch λ_{22} at different loading rates of 10%/s, 1%/s, and 0.1%/s for MNE-60, MNE-45, and MNE-30, respectively.

Figure 2.10g-i show the shear strain λ_{21} as a function of the normal stretch λ_{22} at different loading rates. The occurrence of shear strain is a consequence of director rotation. In general, it is observed that an increase in λ_{22} leads to greater rotation of the director, and an increase in the magnitude of λ_{21} in MNE-60 and MNE-45. Particularly in the case of loading rates at 1%/s and 0.1%/s, the modeling results exhibit a high level of agreement with the experimental findings. However, the shear strain at 10%/s presents inconsistencies with the experimental observation, as it shows a lower value at a lower normal stretch compared to the 1%/s loading rate, which can be attributed to the omission of the viscosity of director rotation in the model. Experimental evidence has indicated that the director does not reach the equilibrium at 10%/s loading rate, and both the viscosity of the director rotation and network extension contribute to the delayed direction rotation.

Moreover, we observe non-monotonic shear strain λ_{21} with respect to the normal stretch λ_{22} in MNE-30. The shear strain initially grows to a positive value and then drops to a negative value with the increased normal stretch. Warner and Terentjev *et al*.[24,84,85] have discussed non-monotonic shear strain when the initial director ($\theta = 0°$) is perpendicular to the stretching direction. Without the viscous effect, the director and shear strain can be expressed as

$$\theta = \sin^{-1}\sqrt{\frac{r}{r-1}\left(1-\frac{{\lambda_{ss}}^2}{{\lambda_{22}}^2}\right)}, \tag{2.19}$$

$$\lambda_{21} = \sqrt{\frac{({\lambda_{22}}^2-{\lambda_{ss}}^2)(r{\lambda_{ss}}^2-{\lambda_{22}}^2)}{r{\lambda_{22}}^2{\lambda_{ss}}^3}}, \tag{2.20}$$

where $\lambda_{ss} = \left(\frac{r-1}{r-1-ar}\right)^{\frac{1}{3}}$ related to semi-soft elasticity. When a=0, $\lambda_{ss} = 1$, and the above equations reflect the case of soft elasticity.

Figure 2.11a and b illustrate the behavior of the director and shear strain based on eqn (2.19) and (2.20) for a=0.1. The director and shear strain start with $\theta = 0°$ and $\lambda_{21} = 0$ when $\lambda_{22} = 1$. As the director angle increases, the shear strain non-monotonically increases and then decreases. Then the director and shear strain end with $\theta = 90°$ and $\lambda_{21} = 0$ when $\lambda_{22} = \sqrt{r}\lambda_{ss} = 2.42$. After the director becomes parallel to the stretching direction, the network further extends with an elastic energy cost without director rotation, behaving the same as traditional neo-Hookean materials.

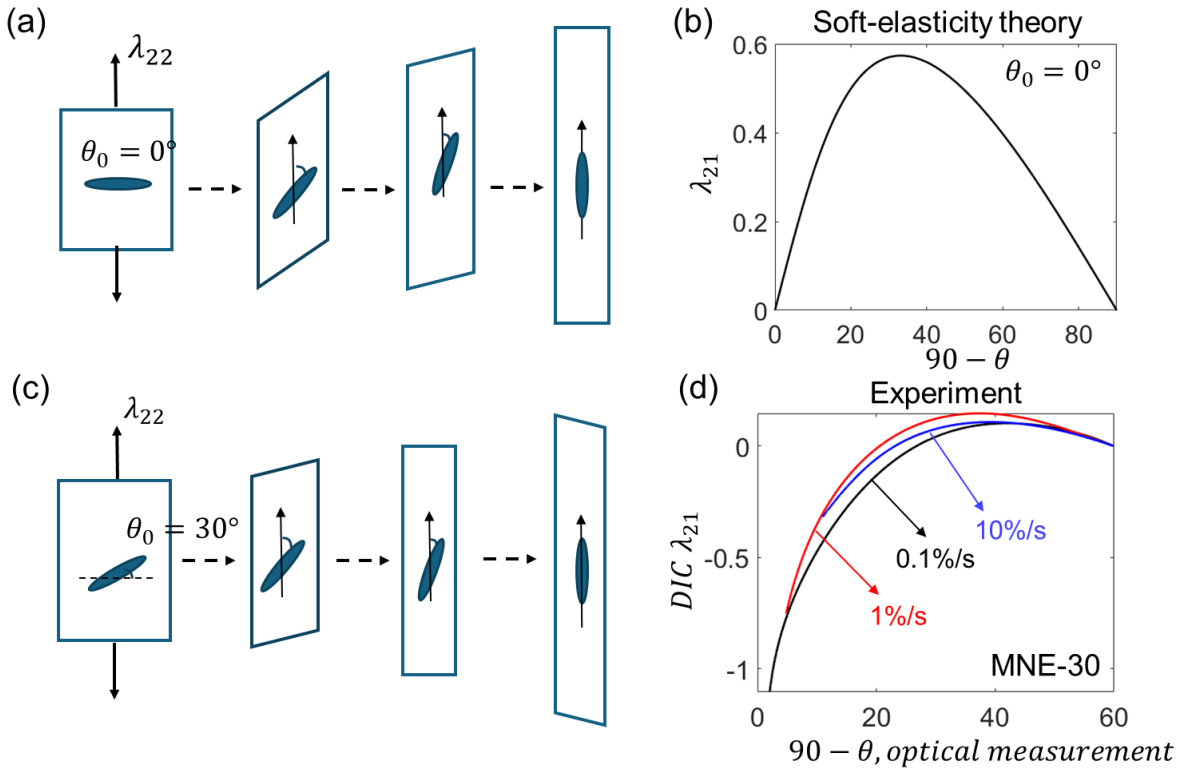

Figure 2.11 (a) Schematic of the deformation of a LCEs sample with the stretching perpendicular to the initial director ($\theta_0 = 0°$). (b) Shear strain as a function of the director rotation starts from $\theta_0 = 0°$ and ends at $\theta = 90°$ calculated from the soft-elasticity theory. (c) Schematic of the deformation of MNE-30 under uniaxial stress, exhibiting changes of the shear strain λ_{21} from a positive value to a negative value.

(d) Shear strain of MNE-30 as a function of the director rotation at loading rates of 0.1%/s, 1%/s, and 10%/s up to a strain of 200% from the experiment.

The experimental measurement of shear strain for MNE-30 is presented in Figure 2.11d as a function of the director. The macroscopic deformation under stretching is depicted in Figure 2.11c, illustrating the transition of shear strain from a positive value to a negative value induced by the director rotation. Based on the perpendicular loading discussed earlier, considering the shear strain at the initial director $\theta_0 = 30°$ as zero in Figure 2.11b, the shear strain exhibits non-monotonic behavior as the stretch increases and as the director θ changes from 30° to 90°. Consequently, the non-monotonic shear strain is expected when the initial director deviates much from the stretching direction.

2.5 Conclusion

To summarize, this chapter presents controlled experiments to manifest the relation among mechanical stress, director, and stretch for LCEs with different initial directors at different loading rates. Examined by dynamically uniaxial tension and relaxation tests, we find that the viscoelasticity of LCEs is a synergy of rate-dependent network deformation and mesogen rotation, giving rise to the unique mechanical responses of LCEs, which is further verified by a general continuum viscoelastic model.

We successfully measure the rate-dependent stress and director rotation in dynamic tension and relaxation tests. In the uniaxial tension tests, the loading rates range from 0.1%/s to 10%/s and the initial director ranges from 0° to 60° oblique to the stretching direction. We observe realignment of oblique directors to the stretching direction, and reorientation delay when the loading rate is high. A larger director rotation produces a higher spontaneous strain, which

leads to a higher stretchability and a more obvious stress plateau. By comparing the stress and director values in uniaxial tension and relaxation tests, we find the viscosity of director rotation is much smaller than that of the network extension. For all specimens, stress does not reach equilibrium even at the slow loading rate of 0.1%/s, while the director almost reaches equilibrium at around 1%/s. Moreover, the stress relaxation in a short time reflects the complicated synergy of quick director rotation and network extension, while in a long time, the stress relaxation can be fitted by a power law which is similar to traditional rubbers, suggesting that the relaxation is dominated by the network extension. Although the viscosity of director rotation is considerably small, in a long-term relaxation, the director continues to rotate as the viscous network extension further realigns the director, and the director relaxation could also be fitted by a power law.

We quantitatively measure the rate-dependent strain components via DIC for LCEs with different initial directors. Our DIC results under uniaxial tension tests reveal homogenous deformation in the middle parts of the LCE samples. At a lower rate, the macroscopic deformation is primarily originated from spontaneous deformation arising from director rotation, exhibiting the stress-strain relation closer to the plane strain case; conversely, at a higher rate, the macroscopic deformation is more attributed to network extension, leading the stress-strain relation closer to the plane stress case. DIC measurements present notable rate-dependent shear strain, where faster loading leads to smaller shear strain, and vice versa. Non-monotonic shear strain is observed when the angle between the initial director and the stretching is large.
We further use a general continuum viscoelastic model to explain the rate-dependent stress, director, and strain. The model incorporates the effect of the viscous network deformation via

applying multiplicative decomposition of the deformation gradient to elastic and viscous parts. No director viscosity is considered in this analysis. The analytical solution elucidates the strong coupling between the macroscopic deformation and microscopic director rotation – on one hand, the director rotation provides additional spontaneous deformation, reducing the network extension and corresponding stress levels; on the other hand, the observation of the director reorientation delay indicates that the rate-dependent network deformation influences the rate-dependent director rotation. Furthermore, the analytical results indicate the possibility of non-monotonic shear strain when the angle between the initial director and the stretching direction is large enough.

This work provides a comprehensive investigation into and mechanistic understanding of the rate-dependent behavior of LCEs. The utilization of crossed-polarized optical measurement and DIC allows us to dynamically probe the director and deformation fields for LCEs of different directors under different loading conditions. We conduct experiments to characterize the distinct relaxation time scales of the director rotation and network extension and explain the rate-dependent results using a general viscoelastic continuum model, which enhances our understanding of the director-stress coupling effect. However, it is important to note that a much lower loading rate needs to be applied in order to reach the full equilibrium stress-strain behavior of LCEs [29]. Moreover, the efficacy of the model diminishes at high loading rates, where the viscosity of both the director and network needs to be accurately accounted for [72,74].

Chapter 3 Exceptional Stress-director Coupling Effect at the Crack Tip

A liquid crystal elastomer (LCE) presents a highly promising material utilized in the realm of soft robotics primarily attributed to its unique capability of spontaneous strain achieved through changes in ordering and director. To achieve durable applications of LCEs, it becomes imperative to thoroughly understand and characterize their fracture behavior. Despite extensive exploration of the stress-director coupling effect of LCEs under uniaxial tension, the influences of such coupling on the stress/strain behavior in the vicinity of a crack tip remains inadequately understood. In this chapter, we for the first time undertake a comprehensive theoretical and experimental analysis of the displacement and director fields in edge-cracked LCE specimens with various initial director orientations. Our results reveal that the directors undergo significant and inhomogeneous rotation at the crack tips, leading to very different stress/strain distributions from traditional elastomers. Particularly, when the initial director is tilted to the loading direction, the stress/strain distributions are asymmetrical about the crack plane. Notably, we discover the unexpected occurrence of opposite director rotation in two adjacent domains along the circumferential direction at the crack tip, leading to opposite shear strain in the domains, and thereby a sharp crack surface at the domain wall. As a result, LCEs with an initial director tilted to the loading exhibit much smaller crack openings and energy release rates than those of neo-Hookean materials, while LCEs with a parallel director exhibit higher values. This study provides an understanding of how the stress-director coupling of LCEs triggers their unique crack-tip fields, and insights into strategies to enhance the fracture properties of LCEs for future applications. The findings and methodology presented in this work also lay a solid foundation for further investigation of crack propagation in LCEs.

3.1 Introduction

The intricate stress-director coupling behavior in LCEs poses challenges in understanding the mechanism of their deformation and fracture. Attributed to the unique stress-director coupling effect, we expect significant and highly non-uniform director rotation near the crack tip of a LCE, which can dramatically influence its corresponding stress/strain distribution and fracture behavior.

Several studies have already demonstrated the pronounced impact of stress-director coupling on the fracture behavior of LCEs, which deviates considerably from that of traditional neo-Hookean materials. The reorientation of the director near the crack tip exerts remarkable influences on the fracture energy. Specifically, polydomain LCEs exhibit higher fracture energy than that of monodomain, and monodomain LCEs under stretching parallel to the director display higher fracture energy than that under perpendicular loading [54,61]. The difference in the fracture energy among the different samples was attributed to the director rotation in polydomain LCEs and monodomain LCEs subjected to perpendicular stretching, although no further understanding of the numbers was provided. To investigate the director rotation due to stress concentration, a monodomain LCE sheet containing a circular or an elliptical hole subject to remote tension was analyzed by finite element method (FEM) [51–53]. It was found that when the initial director around the hole edge forms a tilted angle with the stretching, the stress concentration factor is lower than that in the parallel case, and reaches the minimum at the tilted angle of 45°. However, studying stress concentration solely is insufficient to fully comprehend the crack growth resistance in LCEs, and the intricated interplay of stress and the director around

a sharp crack remains elusive. Moreover, the crack-tip fields of LCEs have not been experimentally characterized.

Characterizing the deformation fields around a crack tip under various loading plays an important role in validating crack-tip fields predicted computationally and analytically in highly deformable soft materials [48–50]. It becomes particularly crucial when it is challenging to develop an asymptotic solution for the stress/strain fields near a crack tip. Digital image correlation (DIC) has been proven effective in mapping the nonlinear deformation in the vicinity of a crack in highly deformable soft materials [86–88]. Zehnder et al. [88] utilized DIC to measure the strain distribution for a hydrogel specimen with an edge crack in the presence of large strain and strain gradients. In addition to DIC, the particle tracking method is an alternative method to probe inhomogeneous deformation fields. Long et al. [48,50] successfully utilized the particle tracking method to measure the deformation history near a crack in a rubber-like material subjected to tensile loading with different angles between the initial crack and the tension direction, equivalent to combined loading of tension and shear. Distinct from a common soft elastic material [89–91], LCEs can have significant and highly inhomogeneous director rotation at the crack tip, which can induce a highly inhomogeneous spontaneous strain field. Characterizing the microscopic director field near a crack is essential to understanding the crack-tip and fracture behavior of LCEs.

In this chapter, we analyze the fracture behavior of LCEs with a single-edge crack subjected to remote strain, see Figure 3.1a. Motivated by the pronounced stress-director coupling of LCEs, we anticipate that the crack-tip fields and fracture behavior of LCEs are very different from those of traditional elastomers. On one hand, the highly inhomogeneous and concentrated

stress at a crack tip can reorient the directors to different levels, inducing large and inhomogeneous spontaneous strain; on the other hand, different rotation capability of the directors around the crack tip gives rise to different levels of stress softening, influencing the stress distribution and energy release rate, and consequently leading to distinct crack opening shapes from traditional elastomers, see Figure 3.1b and c. Moreover, the angle between the initial director and stretching can dramatically vary the crack-tip fields and crack opening. In particular, when the angle is oblique, the adjacent directors exhibit opposite rotation around the crack tip, forming a domain wall, and the stress/strain field is highly asymmetric about the crack plane, as shown in Figure 3.1c. To demonstrate the unique crack-tip behavior, we simulate the stress, displacement and director fields in the vicinity of a sharp crack in LCEs with different initial directors, and subsequently evaluate their energy release rates. Moreover, experimental data capturing the deformation field by the DIC method and the director field by the crossed-polarized optical measurement will be acquired to validate the simulation results. Through combining numerical modeling and experimental observations, we aim to gain a comprehensive understanding of the crack-tip fields and fracture behavior of LCEs. Notably, this study represents the first instance of observing the director and deformation fields in the vicinity of a crack in LCEs.

This chapter is organized as follows. In section 3.2, we introduce the detailed modeling and experimental methodology. In section 3.3, we report the FEM analysis of the stress-director coupling around the crack-tip field. We present the experimental measurement of the director and displacement in section 3.4. Section 3.5 shows fracture evaluation. Section 3.6 concludes the Chapter.

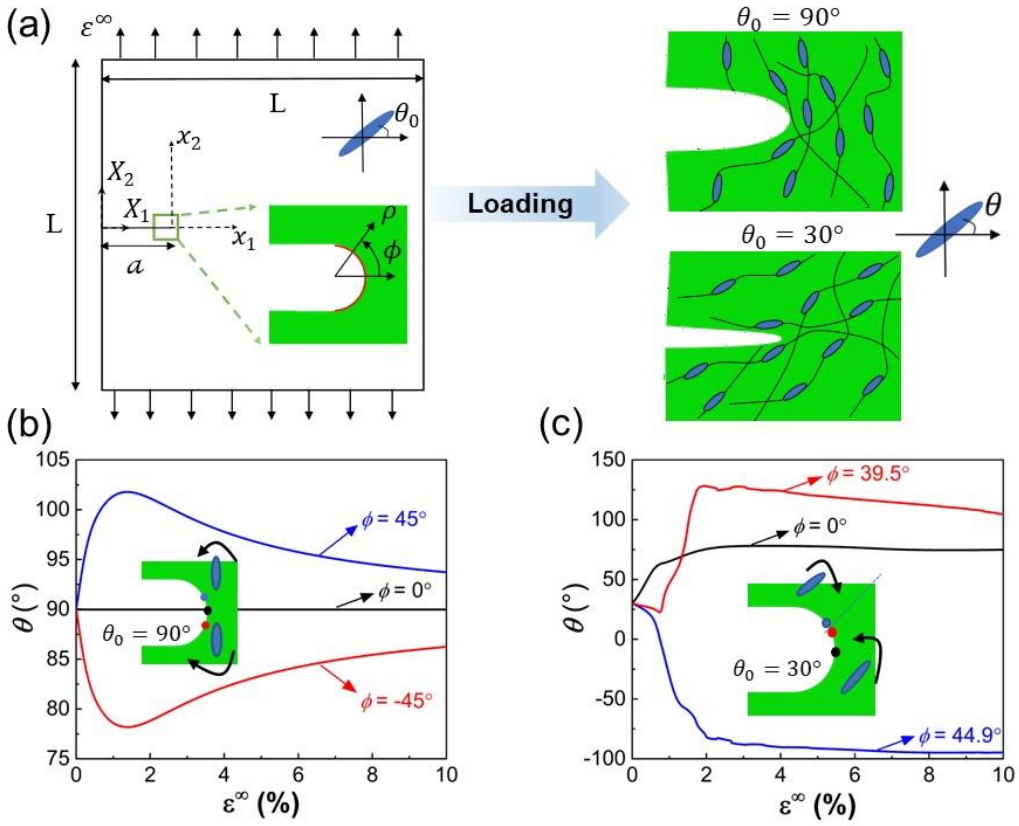

Figure 3.1 Director rotation in edge-cracked LCEs under external tension. (a) Schematic illustration of an edge-cracked LCE sample subjected to remote strain ε^{∞}. Different initial directors, as shown for $\theta_0 = 90°$ and $\theta_0 = 30°$, lead to different crack openings due to director rotation. The director evolution at selected points on the crack surface as a function of the remote strain in the LCE with (b) $\theta_0 = 90°$ and (c) $\theta_0 = 30°$.

3.2 FEM and Experimental Methodology

3.2.1 Constitutive Model and FEM

To model the constitutive behavior of a LCE, we consider a material particle labeled by a position vector $\mathbf{X}$ in the stress-free reference configuration Ω_0 ($\mathbf{X} \in \Omega_0$) moves to the position $\mathbf{x}$ at time t in the current configuration Ω_c ($\mathbf{x} \in \Omega_c$). The deformation gradient is defined as $F_{iK} =$

$\partial x_i(\mathbf{X},t)/\partial X_K$. A unit vector $\boldsymbol{d}$ is used to describe the director orientation in the current configuration. Under the isothermal condition, the free energy density of nematic LCEs in the reference configuration is assumed [24,72]:

$$f_r(\boldsymbol{F},\boldsymbol{d},\nabla\boldsymbol{d}) = f_{el}(\boldsymbol{F},\boldsymbol{d}) + f_{ss}(\boldsymbol{F},\boldsymbol{d}) + f_{Frank}(\nabla\boldsymbol{d}) + f_c(\boldsymbol{d}). \quad (3.1)$$

The first term in Eqn. (3.1),

$$f_{el}(\boldsymbol{F},\boldsymbol{d}) = \mu(Tr(\boldsymbol{l_0 F l^{-1} F^T}) - 3 - 2ln\,(J))/2 + B(J-1)^2/2, \quad (3.2)$$

describes the entropic elasticity of the LCE network, which is also called the neo-classical free energy [81], where μ is the shear modulus, B is the bulk modulus and $J = \det(\boldsymbol{F})$. The first part of the energy, $\mu Tr(\boldsymbol{l_0 F l^{-1} F^T})/2$, is a function of both $\boldsymbol{F}$ and $\boldsymbol{d}$, incoporating the coupling effect of the network deformation and the director rotation. $\boldsymbol{l}$ and $\boldsymbol{l_0}$ are the step length tensors in the current and reference configurations, respectively, $\boldsymbol{l} = (l_\parallel - l_\perp)\boldsymbol{d}\otimes\boldsymbol{d} + l_\perp\boldsymbol{I}$ and $\boldsymbol{l_0} = (l_\parallel^0 - l_\perp^0)\boldsymbol{d_0}\otimes\boldsymbol{d_0} + l_\perp^0\boldsymbol{I}$, with $\boldsymbol{d_0}$ the director in the reference configuration. Since we consider the isothermal condition, the effective lengths along or perpendicular to the director in the current configuration ($l_\parallel$ and $l_\perp$) remain the same as those in the reference configuration ($l_\parallel^0$ and $l_\perp^0$), and we can denote the ratio $r = l_\parallel/l_\perp = l_\parallel^0/l_\perp^0$ as the anisotropy of the backbone. The second part, $B(J-1)^2/2$, is the energy associated with volume changes, with B the bulk modulus. We employ a large ratio of the bulk modulus to shear modulus, $B/\mu = 10^3$, to represent incompressibility. The second term in Eqn. (3.1),

$$f_{ss}(\boldsymbol{F},\boldsymbol{d}) = \mu Tr(\alpha(\boldsymbol{I} - \boldsymbol{d_0}\otimes\boldsymbol{d_0})\boldsymbol{F^T}\cdot\boldsymbol{d}\otimes\mathbf{d}\cdot\mathbf{F})/2 \quad (3.3)$$

describes the inevitable variation of the anisotropy r among chains, called the semi-soft elasticity [92], with α a parameter describing the level of such fluctuation. The third term in Eqn. (3.1),

$$f_{Frank}(\nabla \boldsymbol{d}) = K\nabla \boldsymbol{d}\colon \nabla \boldsymbol{d}/2 \tag{3.4}$$

is a simplified form of the Frank energy, which describes energy associated with the spatial variation of the director [93]. The parameters of the Frank energy and network elasticity, $\sqrt{K/\mu}$, defines a length scale, which is typically on the order of 10 nm [24]. The last term in Eq. (3.1),

$$f_c(\boldsymbol{d}) = \gamma_d(\boldsymbol{d}\cdot\boldsymbol{d} - 1) \tag{3.5}$$

enforces the constraint of the unit vector $\boldsymbol{d}$, $\boldsymbol{d}\cdot\boldsymbol{d} \equiv 1$, where γ_d is a Lagrange multiplier.

Consider the deformation of a LCE as an equilibrium isothermal process. The thermodynamic condition requires the variation of the free energy of the LCE over a small time increment should always equal the external power, $\int_{\Omega_0} \dot{f}_r dV = \dot{W}$, where $\dot{W} = \int_{\Omega_c} \boldsymbol{b}\cdot\dot{\boldsymbol{u}} dv + \int_{\Gamma_c} \boldsymbol{t}\cdot\dot{\boldsymbol{u}} da$ represents the power done by the body force $\boldsymbol{b}$ and surface traction $\boldsymbol{t}$ at the velocity $\dot{\boldsymbol{u}}$, respectively, in the current configuration, with Γ_c the prescribed traction boundary, and $\dot{} = \delta/\delta t$ in $\dot{f}_r$, $\dot{\boldsymbol{u}}$, $\dot{W}$ etc. represents a small variation over a small time increment. Using the relation $\dot{f}_r = \partial f_r/\partial \boldsymbol{F}:\dot{\boldsymbol{F}} + \partial f_r/\partial \boldsymbol{d}:\dot{\boldsymbol{d}} + \partial f_r/\partial \nabla \boldsymbol{d}:(\nabla\dot{\boldsymbol{d}})$, we can derive two governing equations related to $\dot{\boldsymbol{u}}$ and $\dot{\boldsymbol{d}}$,

$$div(\boldsymbol{\sigma}) + \boldsymbol{b} = \boldsymbol{0}, \tag{3.6}$$

$$J^{-1}\mu\left(\left(l_{\parallel}^{-1} - l_{\perp}^{-1}\right)\boldsymbol{F}\boldsymbol{l}_{\boldsymbol{0}}\boldsymbol{F}^{\boldsymbol{T}}\boldsymbol{d} + \alpha\boldsymbol{F}(\boldsymbol{I} - \boldsymbol{d}_{\boldsymbol{0}}\otimes\boldsymbol{d}_{\boldsymbol{0}})\boldsymbol{F}^{\boldsymbol{T}}\boldsymbol{d}\right)\times\boldsymbol{d} - J^{-1}K\nabla^{\boldsymbol{2}}\boldsymbol{d}\times\boldsymbol{d} = \boldsymbol{0}, \tag{3.7}$$

where the Cauchy stress $\boldsymbol{\sigma}$ is

$$\boldsymbol{\sigma} = J^{-1}\mu\left(\boldsymbol{l}^{-1}\boldsymbol{F}\boldsymbol{l}_{\boldsymbol{0}}\boldsymbol{F}^{\boldsymbol{T}} + \alpha\boldsymbol{d}\otimes(\boldsymbol{I} - \boldsymbol{d}_{\boldsymbol{0}}\otimes\boldsymbol{d}_{\boldsymbol{0}})\boldsymbol{F}^{\boldsymbol{T}}\boldsymbol{d}\cdot\boldsymbol{F}^{\boldsymbol{T}} - \boldsymbol{I}\right) + 2B(J-1)\boldsymbol{I} - J^{-1}K(\nabla\boldsymbol{d})^{T}\nabla\boldsymbol{d}. \tag{3.8}$$

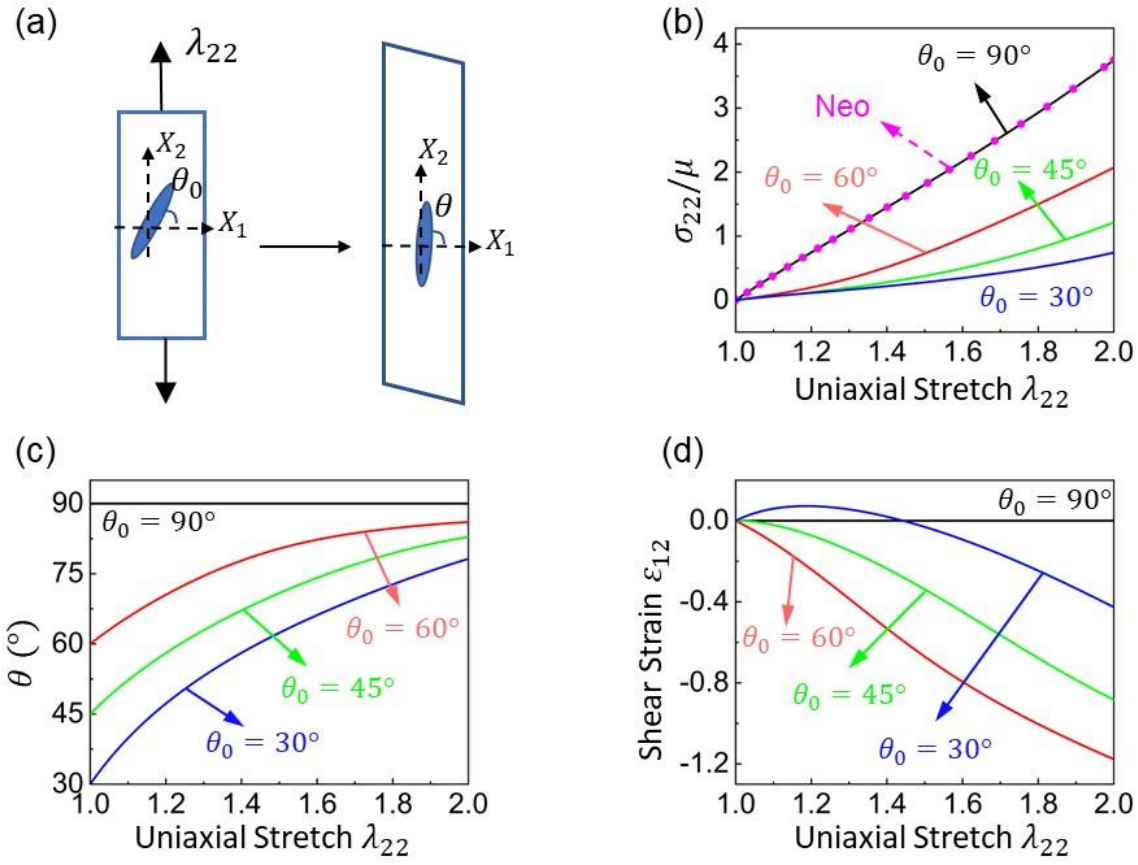

Figure 3.2 Theoretical prediction of the uniaxial response of LCEs with different initial directors θ_0. (a) Schematic of the uniaxial stretch with θ defined as the angle between the director and the $X_1 - axis$. (b) Stress, (c) director, and (d) shear strain as functions of uniaxial stretch for different initial directors.

The constitutive model generally provides a comprehensive description of the properties exhibited by LCEs under uniaxial tension (Figure 3.2a). It is observed that when the initial director aligns with the stretching direction ($\theta_0 = 90°$), the stress-stretch behavior resembles that of a neo-Hookean material (Figure 3.2b) without director rotation and shear strain (Figure 3.2c and d). In contrast, when the initial director is tilted away from the stretching direction ($\theta_0 = 60°, 45°, 30°$), stress softening occurs, accompanied by director reorientation and non-zero shear strain.

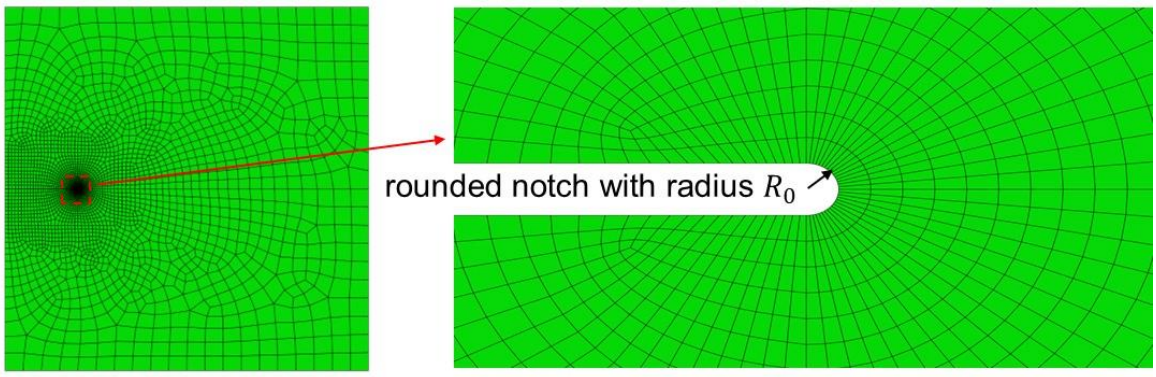

Figure 3.3 Setup of the FEM model of a LCE specimen with a rounded notch tip with a radius $R_0/a = 5e-4$.

Appendix A.2. To accommodate nearly incompressible solids and mitigate volumetric locking behavior, we implemented the F-bar method [94,95] and utilized 2D plane-strain 4-node linear quadrilateral elements in this study. We simulate a 2D rectangular LCE sample of an initial director θ_0 with an edge crack, as shown in Figure 3.1a. The top and bottom boundaries are controlled by a displacement in the X_2 direction, and fixed in the X_1 direction with a zero displacement, $u_1 = 0$. To prevent element distortion due to the strain concentration around the crack tip, a rounded notch is utilized, where the radius of the notch is $R_0/a = 5 \times 10^{-4}$ and the ratio of the crack length to the sample length is $a/L = 0.2$, with $L = 1\ mm$ (Figure 3.3). To resolve the crack-tip fields and to ensure the element size in the vicinity of the crack tip comparable to $\sqrt{K/\mu}$, we set the size of the elements around the tip about 0.1 times of the notch size R_0, i.e. about $5e-5$ times of the crack length a, and $1e-5$ times of the model size L. We analyze fracture behavior when the crack opens much larger than the notch width so that the results are independent of the crack-tip shape [96,97]. As we consider the plane strain condition,

the director is described by the unit direction $\boldsymbol{d} = (cos(\theta), sin(\theta), 0)$ with θ the angle between the current director and the X_1-axis. The material properties are chosen as

$$\frac{B}{\mu} = 10^3, r = 5, \alpha = 0.1, \sqrt{\frac{K}{\mu}} = 10\ nm, \quad (3.9)$$

where the bulk modulus over the shear modulus is set large to represent incompressibility; the material anisotropic parameter r and semi-soft elasticity parameter α are based on our previous study [62]; the value of the Frank energy parameter with respect to shear modulus is estimated based on the previous report [24]. To ensure convergence of the simulations, small viscosity of the network and director rotation is added to the model. Moreover, the solution control parameters in ABAQUS are adjusted to allow an excessive number of increments and iterations to address the convergence issue. In particular, we set the maximum number of line search iteration to be 10. More details about the viscoelastic model and UEL implementation could be found in Appendix A.1 and A.2.

3.2.2 Experimental Methods

3.2.2.1 LCEs Fabrication

In this study, the main-chain monodomain LCEs were synthesized via a two-stage thiol-acrylate Michael addition-photopolymerization (TAMAP) reaction. The method is described in Section 2.2.1.

3.2.2.2 Tension Tests

Rectangular strips with a width of 25 mm and length of 75 mm were cut out of a LCE sheet with angles $0°, 30°, 45°$, and $60°$ between the director and the longitudinal direction of the strips (Figure 3.4a). The solid rod-like mesogen represents the director in the whole LCE sheet

and the tilted red dashed line represents the cut LCE specimen with an initial director θ_0, which was measured by a protractor and further verified by the optical polariscopy method. In the specimens, 25 mm was left on each of the two ends for clamping and the middle region of 25 mm by 25 mm was used for fracture testing. We used a sharp blade to cut an edge crack of 5 mm in the middle of the height. The tension test was performed in an Instron universal testing machine (Model 5944) with a 50 N load cell. The specimens were uniaxially stretched up to 10% strain with steps of 0.5% of the gauge length imposed. In each step, the loading rate was 0.01%/s and we waited for another 5 mins to ensure the specimen reaches quasi-equilibrium before any measurements were taken. No crack propagation occurred during tension tests and all the specimens could be reused for multiple measurements.

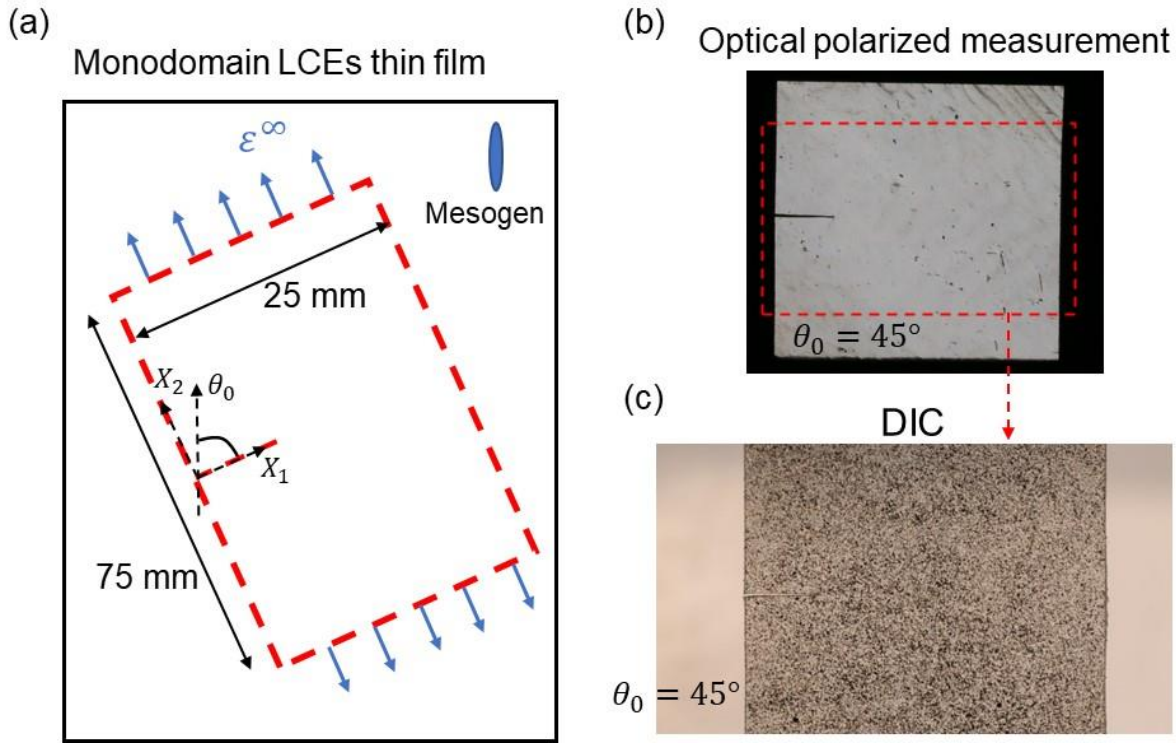

Figure 3.4 (a) Schematic of a LCE specimen cut from a fabricated monodomain LCE thin film with the initial director angle θ_0 away from the transverse X_1 direction. (b) Image of a LCE specimen with initial

director $\theta_0 = 45°$ at $\varphi = 0°$ and $\varepsilon^{\infty} = 0\%$ in an optical polarized measurement. (c) Image of the marked part of a LCE specimen in Figure 3.4b with sprayed patterns for DIC tests.

3.2.2.3 Crossed-polarized Optical Measurements

Director rotation driven by stretching was characterized by crossed-polarized optical measurements. A light source, a polarizer, a specimen stretched by the Instron universal testing machine, an analyzer with the polarization perpendicular to the polarizer, and a camera were set up in the order as described in Section 2.2.3 (Figure 2.2). The appearance change of the specimen under uniaxial tension was recorded by a Canon ESO 6D DSLR camera along with a Canon 100mm F/2.8L macro lens. The recorded images per 0.5% strain were used to measure the transmitted light intensity via ImageJ. We measured the transmitted light intensity for different orientations of the crossed-polarizers by rotating them every $10°$ from $0°$ to $90°$ to determine the director as a function of stretch. The details are elaborated in Section 2.2.3. Figure 3.4b shows an example of an LCE specimen during optical polarized measurement at $\varphi = 0°$ and $\varepsilon^{\infty} = 0\%$. At this moment, the specimen exhibits a uniform and brightest appearance. This observation validates the monodomain nature of the LCE specimen with the initial director $\theta_0 = 45°$.

3.2.2.4 DIC Measurements

We use the 2D digital image correlation (DIC) method to measure displacement distributions as described in Section 2.2.4. Figure 3.4c shows an example of a sprayed sample with the initial director $\theta_0 = 45°$ at $\varepsilon^{\infty} = 0\%$.

3.3 FEM Analysis of the Coupled Stress-director Effect on the Crack-tip Fields

We analyze the crack-tip fields of different initial directors $\theta_0 = 30°, 45°, 60°$, and $90°$. The FEM results have revealed highly inhomogeneous director rotation near the crack tip. When the initial director is parallel to the loading direction ($\theta_0 = 90°$; Figure 2.11b), the director on the crack surface at $\phi = 45°$ rotates counter-clockwise and the director at $\phi = -45°$ rotates clockwise, where ϕ is the polar angle defined in the reference state, while the director remains unchanged at $\phi = 0°$. Intriguingly, when the initial director is inclined with respect to the loading direction ($\theta_0 = 30°$; Figure 2.11c), the directors positioned in close proximity ($\phi = 39.5°$ and $44.9°$) exhibit opposite rotation, i.e. the director at $\phi = 44.9°$ rotates clockwise, but the director at $\phi = 39.5°$ first rotates clockwise and then counter-clockwise, following a non-monotonic trend as the applied strain increases. Such unexpected and inhomogeneous director rotation triggers a question: how does it influence fracture behavior in LCEs? To answer this question, we will next systematically investigate the stress, displacement and director fields, and subsequently the energy release rate.

3.3.1 Stress and Strain Distributions Around A Crack-tip

To begin with, we consider a LCE with a parallel initial director to the remote tension direction ($\theta_0 = 90°$). We present the distributions of the normalized maximum principal Cauchy stress σ_p and the maximum principal Lagrangian strain E_p, where the Lagrangian strain is defined as $\boldsymbol{E} = (\boldsymbol{F}^T\boldsymbol{F} - \boldsymbol{I})/2$, in the region near the crack tip of size $0.01a$ under $\varepsilon^\infty = 10\%$ (Figure 3.5a and b). We observe significant stress/strain concentration at the crack tip. The stress and strain are both symmetrically distributed about the X_1-axis with the contour lines exhibiting an elliptical shape, where a considerably smoother stress/strain gradient aligns in X_2 than that in

X_1. LCEs present very different stress and strain distributions compared to those of neo-Hookean materials, corresponding to $r = 1$, $\alpha = 0$ and $K = 0$ in Eqns. (3.6)(3.7), which show nearly concentric circular stress and strain contour lines (Figure 3.5c and d). Further looking at the stress and strain distributions on the rounded notch surface, we find that while the locations of the maximum principal stress and strain are coincident at the polar angle $\phi = 0°$ in neo-Hookean materials, this is not the case in LCEs (Figure 3.5e and 5f). Although the maximum stress occurs at $\phi = 0°$, consistent with that of neo-Hookean materials, strain peaks at two locations at around $\phi = \pm 50°$. Moreover, on the crack surface the maximum principal stress and strain in LCEs are both larger than those of neo-Hookean materials, which is consistent with the findings reported by Jiang et al. [52] for a monodomain LCE sheet with an elliptical hole. It is worth noting that as indicated by the stress contour lines, in the region a little far from the rounded notch at $\rho/a = 1.5e-3$ and $2.5e-3$ (Figure 3.5e and f), the location of the maximum principal stress is not at $\phi = 0°$ but shifts to around $\phi = 90°$ due to smoother reduction of stress concentration caused by director rotation that will be discussed later. The location of the maximum principal strain also shifts towards $\phi = 90°$.

When the initial director is tilted away from the stretching direction (Figure 3.6 and Figure 3.7), although the stress/strain is still highly concentrated at the crack tip, their distributions exhibit notable distinctions from the case of $\theta_0 = 90°$. Around the crack tip, the fields of stress and strain are no longer symmetrical about the X_1-axis, instead showing elliptic-like contour lines with a smoother gradient nearly along the initial director (Figure 3.6). Moreover, the stress and strain values are significantly smaller than those of $\theta_0 = 90°$, and so is the normalized elastic energy density (Supplementary Fig. S1). For a LCE with $\theta_0 = 30°$, on the

rounded notch surface, the peak maximum principal stress $\log(\sigma_p/\mu) = 1.26$ occurs at around $\phi = -22°$, while the peak maximum principal strain $\log(E_p) = 1.34$ occurs at around $\phi = 5°$ (Figure 3.7a and d). The values are much smaller than those of neo-Hookean materials ($\log(\sigma_p/\mu) = 2.20$, and $\log(E_p) = 1.91$) and LCEs with $\theta_0 = 90°$ ($\log(\sigma_p/\mu) = 2.22$, and $\log(E_p) = 2.13$); see Figure 3.5e and 5f. Such asymmetrical stress and strain distributions lower than those of neo-Hookean materials are also found in other LCEs with tilted initial director $\theta_0 = 45°$ (Figure 3.6(b, e) and Figure 3.7(b, e)) and 60° (Figure 3.6 (c, f) and Figure 3.7(c, f)). Similar to the case of $\theta_0 = 90°$, at the region a little far from the rounded notch at $\rho/a = 1.5e-3$ and $2.5e-3$, the location of the peak maximum principal stress/strain shifts towards the smoothest stress/strain gradient (Figure 3.7).

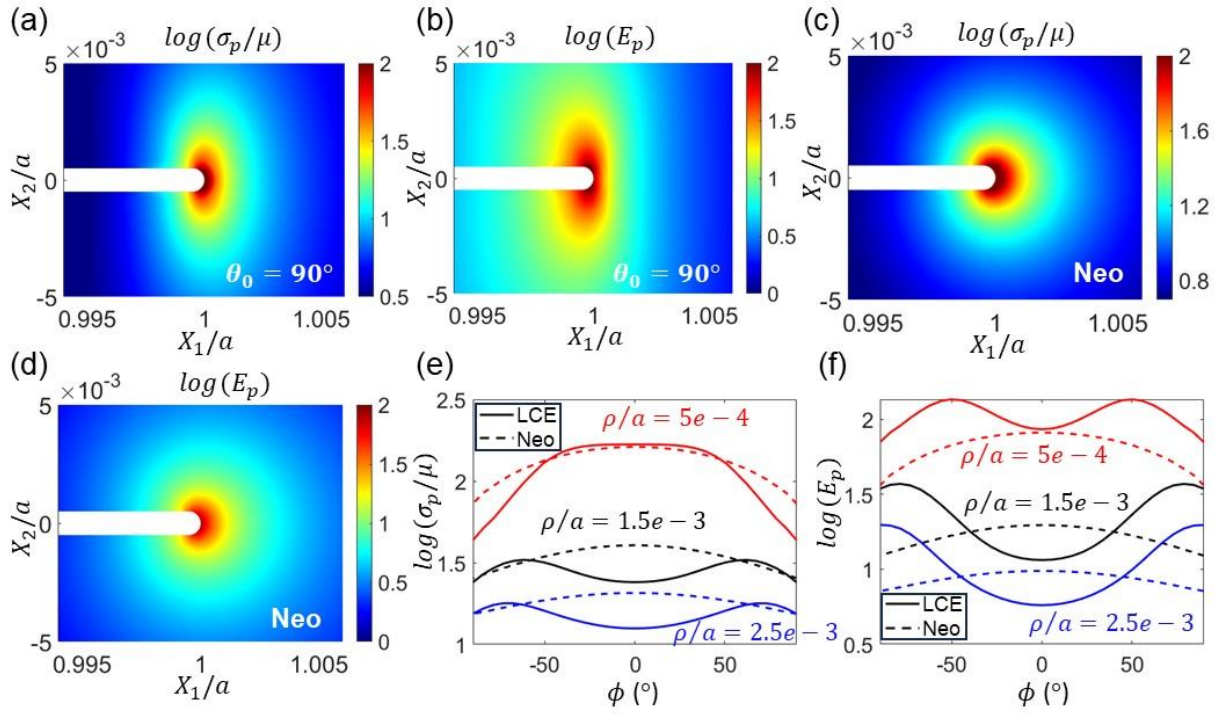

Figure 3.5 FEM results of the stress and strain distributions around the crack tip at remote strain $\varepsilon^{\infty} =$ 10%. (a, c) Normalized maximum principal stress and (b, d) maximum principal Lagrangian strain

around the crack tip in (a, b) a LCE with the initial director $\theta_0 = 90°$ and (c, d) a neo-Hookean material, respectively. The distribution of (e) normalized maximum principal Cauchy stress, and (f) maximum principal Lagrangian strain at different distances ρ/a around the crack tip at remote strain $\varepsilon^{\infty} = 10\%$ for a LCE with $\theta_0 = 90°$ and a neo-Hookean material. Note that on the crack surface, $\rho/a = 5e-4$.

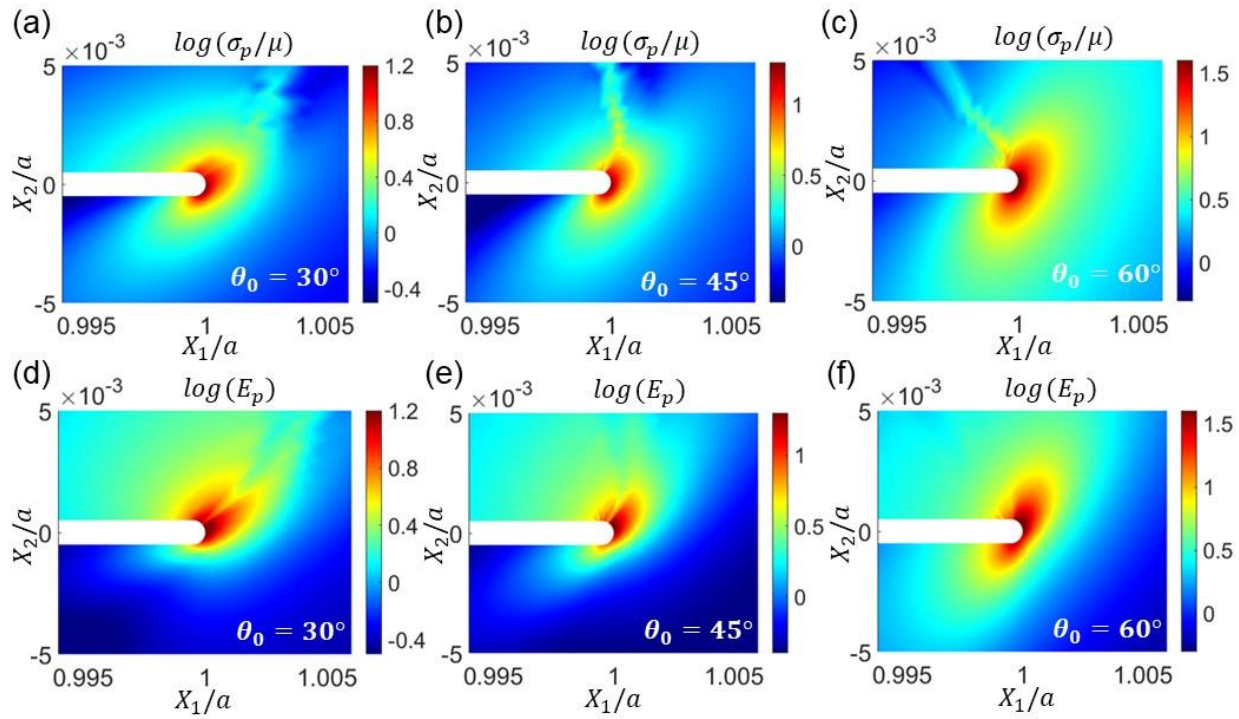

Figure 3.6 FEM results of the stress and strain distributions around the crack tip at remote strain $\varepsilon^{\infty} = 10\%$. (a, b, c) Normalized maximum principal stress and (d, e, f) maximum principal Lagrangian strain around the crack tip in a LCE with the initial director (a, d) $\theta_0 = 30°$, (b, e) 45° and (c, f) 60°.

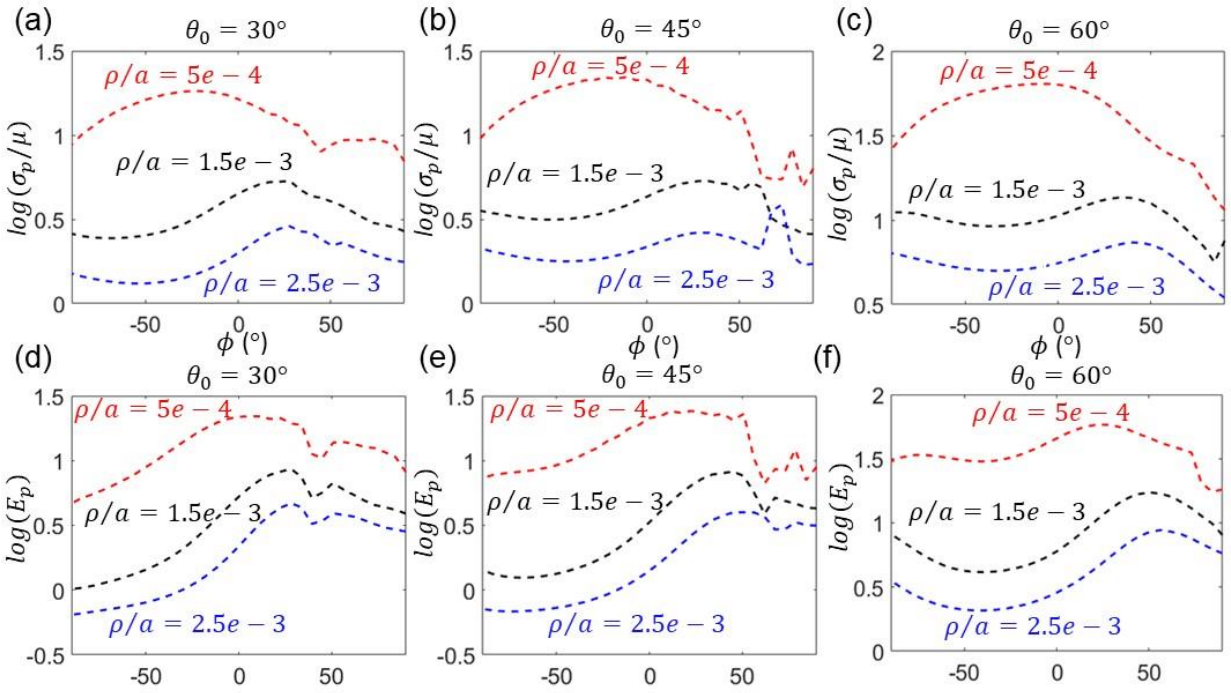

Figure 3.7 FEM results of the stress and strain distributions at different distances ρ/a around the crack tip at remote strain $\varepsilon^{\infty} = 10\%$. (a, b, c) Normalized maximum principal stress, and (d, e, f) maximum principal Lagrangian strain at different distances ρ/a around the crack tip for a LCE with (a, d) $\theta_0 = 30°$, (b, e) 45° and (c, f) 60°. Note that on the crack surface, $\rho/a = 5e-4$.

3.3.2 Director Distribution Around the Crack-tip Field

The observed unusual stress and strain distributions can be attributed to the inhomogeneous and high director rotation at the crack tip. For the LCE with $\theta_0 = 90°$ (Figure 3.8 a), the director at $\phi = 0°$ near the crack tip remains almost unrotated, as the director always aligns with the stretching in this region. In contrast, the director rotates clockwise at $\phi < 0°$ and counter-clockwise at $\phi > 0°$. Correspondingly, when we plot the director change, $\delta\theta = \theta - \theta_0$, we observe negative $\delta\theta$ at $\phi < 0°$ and positive $\delta\theta$ at $\phi > 0°$ (Figure 3.8b). Further away from $\phi = 0°$, the director deviates more from $\theta = 90°$. Interestingly, non-monotonic director rotation

with the applied strain is found around the crack surface. Figure 3.8b shows the change of the director at $\varepsilon^{\infty} = 2\%$ is higher than that at $\varepsilon^{\infty} = 10\%$. To be specific, we select two representative points at $\phi = \pm 45°$ (Figure 3.3b), where the director gradually deviates from $\theta_0 = 90°$, reaches the maximum rotation at $\varepsilon^{\infty} \approx 1.4\%$, and then gradually returns to the initial direction. We also plot the director change at different applied strains as shown in Supplementary Fig. S2a. In general, the maximum director change, $\delta\theta = \theta - \theta_0$, is around $\pm 20°$ at $\phi = \pm 90°$ at $\varepsilon^{\infty} = 2\%$, but decreases to $\pm 8°$ at $\varepsilon^{\infty} = 10\%$.

Such non-monotonic director rotation can be explained based on the director alignment. Figure 3.8c shows that at $\varepsilon^{\infty} = 10\%$ the director (red curve) in the vicinity of the crack surface aligns with the direction of the principal stress (blue crosses) and the tangent direction of the crack surface (green dots), while deviating from the direction of the principal Lagrangian strain (black curve) attributed to the spontaneous strain. The principal stress direction always aligns with the tangent direction of the crack surface, giving the absence of surface traction around the crack surface. When ϕ is larger or smaller than $0°$, the directions of the principal stress are larger or smaller than $90°$, respectively, and thereby the directors rotate toward the corresponding directions. However, the alignment becomes different when the applied strain is small; see Figure 3.8d when $\varepsilon^{\infty} = 0.1\%$. The director (red curve) deviates much from the direction of the principal strain (black curve), principal stress (blue crosses) and the tangent direction of the crack surface (blue dots). At $-45° < \phi < 45°$, the directions of the principal stress and principal strain are coincident as the director undergoes limited rotation, while at $\phi < -45°$ and $\phi < 45°$, the directions of the principal stress and principal strain deviate more from each other as the director far from the crack tip undergoes more rotation, and the resultant higher spontaneous

strain leads to the difference. Plotting these directions at different applied strains (Supplementary Fig. S3a) allows us to unravel that the non-monotonic director change is contributed by the two stages of director reorientation. At small ε^{∞} ($< \sim 2\%$), the director has not aligned with the direction of the principal stress or tangent direction of the crack surface yet, and exhibits rapid and significant rotation towards the principal stress, so $|\delta\theta|$ increases with ε^{∞}; see the dashed curves in Supplementary Fig. S3a at $\varepsilon^{\infty} = 0.1\%$ (red curves) to 2% (blue curves). This substantial director rotation changes the stress and strain concentration around the notch. As ε^{∞} further increases ($> \sim 2\%$) after the director aligns with the principal stress direction, the crack is greatly opened and blunted, and the director rotates back towards 90°, following the deformation, so $|\delta\theta|$ decreases with ε^{∞}; see the dashed curves in Supplementary Fig. S3a at $\varepsilon^{\infty} = 2\%$ (blue curves) to 10% (black curves).

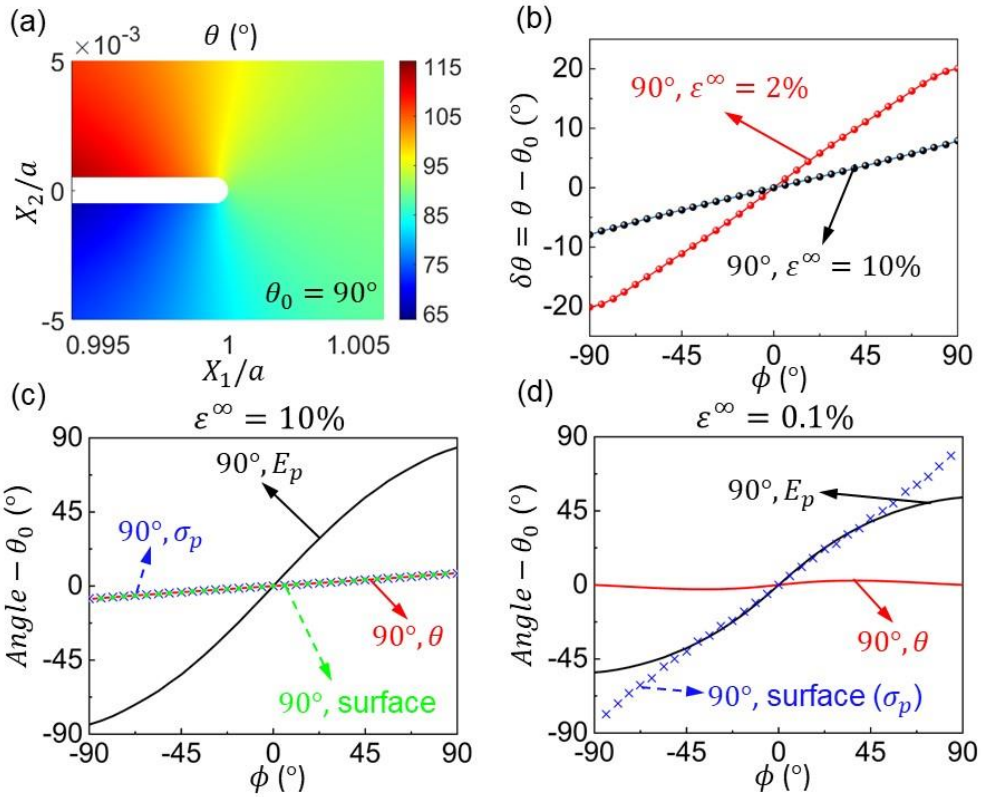

Figure 3.8 FEM results of the director distributions around the crack tip for a LCE with $\theta_0 = 90°$. (a) Distributions of the director at remote strain $\varepsilon^\infty = 10\%$. (b) The change of director around the crack tip at remote strain $\varepsilon^\infty = 10\%$ and 2%. Relative directions of the director, maximum principal stress, maximum principal Lagrangian strain and the tangent direction of the crack opening surface with respect to the initial director $\theta_0 = 90°$ at (c) $\varepsilon^\infty = 10\%$, and (d) $\varepsilon^\infty = 0.1\%$ on the crack surface.

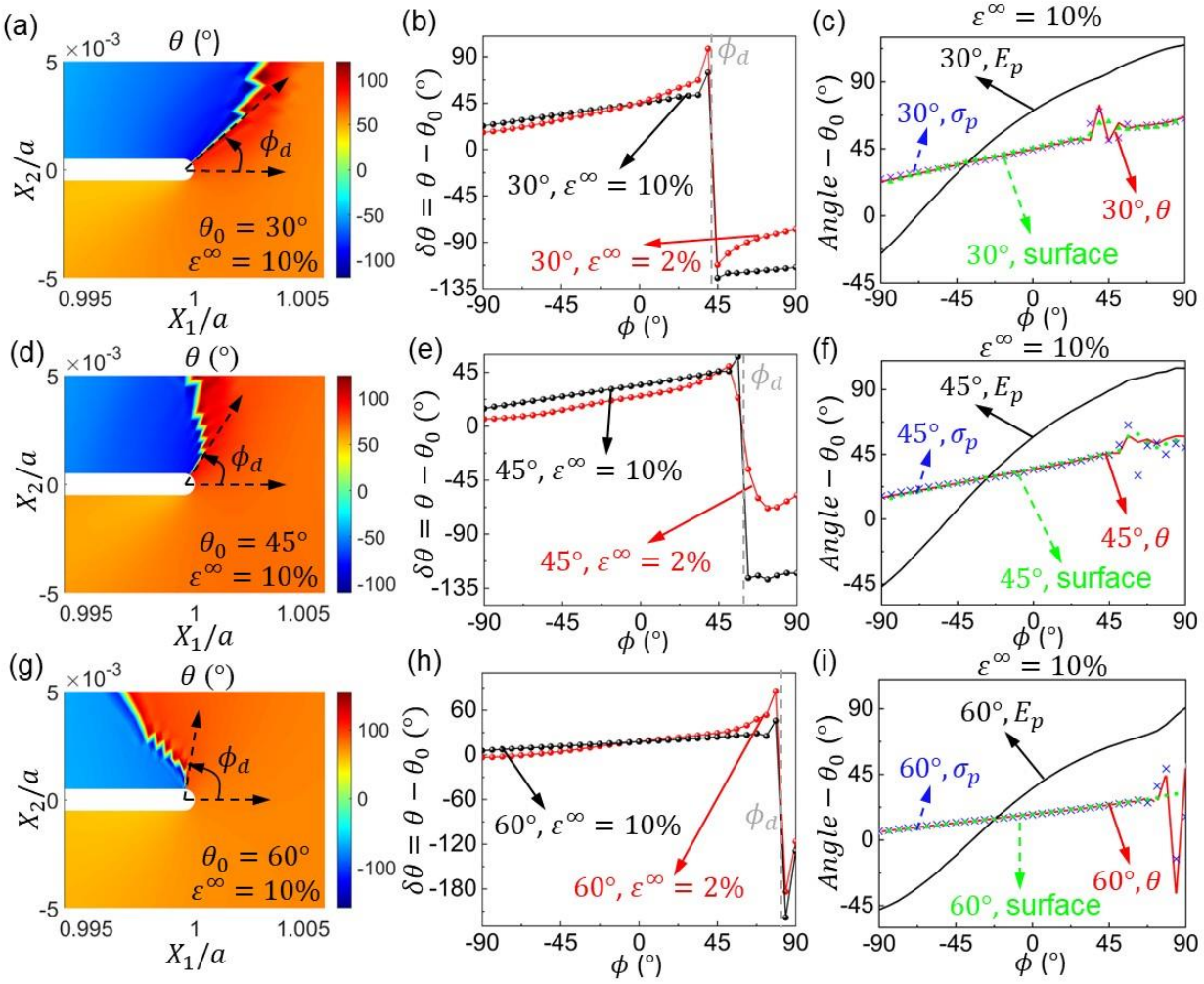

Figure 3.9 FEM results of the director distributions around the crack tip for a LCE with $\theta_0 = 30°$, 45° and 60°. Director fields around the crack tip in LCEs with the initial director (a) $\theta_0 = 30°$, (d) $\theta_0 = 45°$, and (g) $\theta_0 = 60°$ at $\varepsilon^\infty = 10\%$ in the reference configuration. Changes of director on the crack surface in

LCEs with the initial director (b) $\theta_0 = 30°$, (e) 45°, and (h) 60° at $\varepsilon^\infty = 2\%$ and 10%. Relative directions of the director, maximum principal stress, maximum principal Lagrangian strain and the tangent direction of the crack opening surface with respect to the initial director θ_0 for LCEs with (c) $\theta_0 = 30°$, (f) 45°, and (i) 60° on the crack surface at $\varepsilon^\infty = 10\%$. Note that in Figure 3.9(c,f,i) the clockwise director rotation at one side of the domain wall is added by $180°$ due to the symmetry of the director.

For the LCEs with $\theta_0 = 30°$, 45° and 60°, we observe a domain wall at a specific angle $\phi = \phi_d > 0°$, where the adjacent director rotates to opposite directions — clockwise at $\phi > \phi_d$ and counter-clockwise at $\phi < \phi_d$, as depicted in Figure 3.9. As a result, near the domain wall, a sharp jump of the director is observed (Figure 3.9 (b,e,h) and Supplementary Fig. S2(b-d)). The angle ϕ_d monotonically increases with θ_0; when $\theta_0 = 30°$, 45° and 60°, ϕ_d equals around 42°, 53°, and 81.5°, respectively, at $\varepsilon^\infty = 10\%$ (Figure 3.9 (a,d,g)). Note that in Figure 3.9(c,f,i), the clockwise director rotation at one side of the domain wall at $\varepsilon^\infty = 10\%$ is added by $180°$ due to the symmetry of the director. The formation of the domain wall is caused by the nearly perpendicular director to the principal stress direction at ϕ_d, and consequently the directors on the two sides of the domain wall undergo large rotations toward each other to nearly align with the crack surface. Similar formation of domain walls was reported for monodomain LCEs under uniaxial perpendicular stretching, where strip domains, i.e. adjacent domains with directors rotating in opposite directions, are shown to reduce the overall elastic energy [84]. The director around the crack tip also undergoes two stages of reorientation as in the case of $\theta_0 = 90°$ (Figure 3.9 (b,e,h), Figure 3.9(c,f,i) and Supplementary Fig. S3(b-d)): at the beginning, the director did not align with the principal stress direction or the tangent direction of the crack surface, and the

director exhibits considerable rotation until it aligns with the principal stress at $\varepsilon^{\infty} = \sim 2\%$; see the dashed curves in Supplementary Fig. S3(b-d) from $\varepsilon^{\infty} = 0.1\%$ (red curves) to 2% (blue curves). As the remote strain increases to $\varepsilon^{\infty} > \sim 2\%$, the crack tip surface is significantly blunted and opened to nearly 90°, and thereby, the director rotates more slowly following the deformation and approaches 90°; see the dashed curves in Supplementary Fig. S3(b-d) from $\varepsilon^{\infty} = 2\%$ (blue curves) to 10% (black curves). Therefore, for LCEs with tilted initial directors, non-monotonic director rotation only occurs at approximately $0 < \phi < \phi_d$. For example, at $\phi = 39.5°$ for the LCE with $\theta_0 = 30°$, the director angle increases to around $\theta = 127°$ at $\varepsilon^{\infty} = 2\%$, but decreases to around $104°$ at $\varepsilon^{\infty} = 10\%$ (Figure 3.3c).

3.3.3 Elucidating the Effect of Stress-director Coupling

Understanding the inhomogeneous director field at the crack tip can shed further light to the stress and strain distributions. The director rotation for the LCE with $\theta_0 = 90°$ induces compressive spontaneous strain normal to the crack surface, consequently facilitating the crack opening. The director rotation also causes stress softening, resulting in a lower stress/strain gradient towards $\phi = \pm 90°$, and thereby, the elliptical-shaped stress/strain contour lines; see Figure 3.6a and b. To explicitly compute the spontaneous strain, we define the spontaneous Lagrangian strain $\boldsymbol{E_s}$ as the difference between the Lagrangian strain and elastic Lagrangian strain, $\boldsymbol{E}_s = \boldsymbol{E} - \boldsymbol{E}_{elas}$, where $\boldsymbol{E}_{elas} = (\boldsymbol{R^T B}_{elas}\boldsymbol{R} - \boldsymbol{I})/2$ and $\boldsymbol{B}_{elas} := \boldsymbol{l^{-1} F l_r F^T} + \alpha \boldsymbol{d} \otimes (\boldsymbol{I} - \boldsymbol{d_0} \otimes \boldsymbol{d_0}) \boldsymbol{F^T d} \cdot \boldsymbol{F^T}$, and $\boldsymbol{R}$ is the rigid rotation matrix in the polar decomposition of the deformation gradient $\boldsymbol{F} = \boldsymbol{RU}$ [51]. The principal spontaneous Lagrangian strain E_{sp} for the LCE with $\theta_0 = 90°$ distributes symmetrically about $\phi = 0°$ (Supplementary Fig. S4a), consistent with the director changes - the more director rotation indicates more spontaneous strain.

Similarly, for LCEs with tilted directors, the significant director rotation induces large spontaneous strain, and causes sharp changes in stress and strain at ϕ_d (Figure 3.7). In particular, when ε^{∞} is small, the directors rotate in the opposite direction on the two sides of the domain wall, so the shear strain is opposite, consequently resulting in sharp shape changes on the crack surface; see the significant difference of the adjacent directors (represented by blue and red solid cylinders) in Figure 3.10a. On the other hand, when ε^{∞} is large ($> \sim 2\%$), the director difference on the two sides of the domain wall gets close to $180°$, and the director distribution becomes almost continuous across the domain wall again because the directors $\boldsymbol{d} = -\boldsymbol{d}$ are symmetric (Figure 3.10b). Therefore, we added $180°$ to the clockwise director rotation when the director angle difference is more than $150°$ in Figure 3.9(c,f,i). As a result, when the remote strain is high, the crack opening surface becomes smooth again. Similar to the case of $\theta_0 = 90°$, the spontaneous strain also causes stress softening, resulting in similar elliptical-shaped stress/strain contour lines, but with the axis of the smoother gradient aligning around the direction of $\phi = \phi_d$ (Figure 3.6). Due to the much higher director rotation and softening effect, the stress/strain concentration for a tilted θ_0 is much lower than that of $\theta_0 = 90°$.

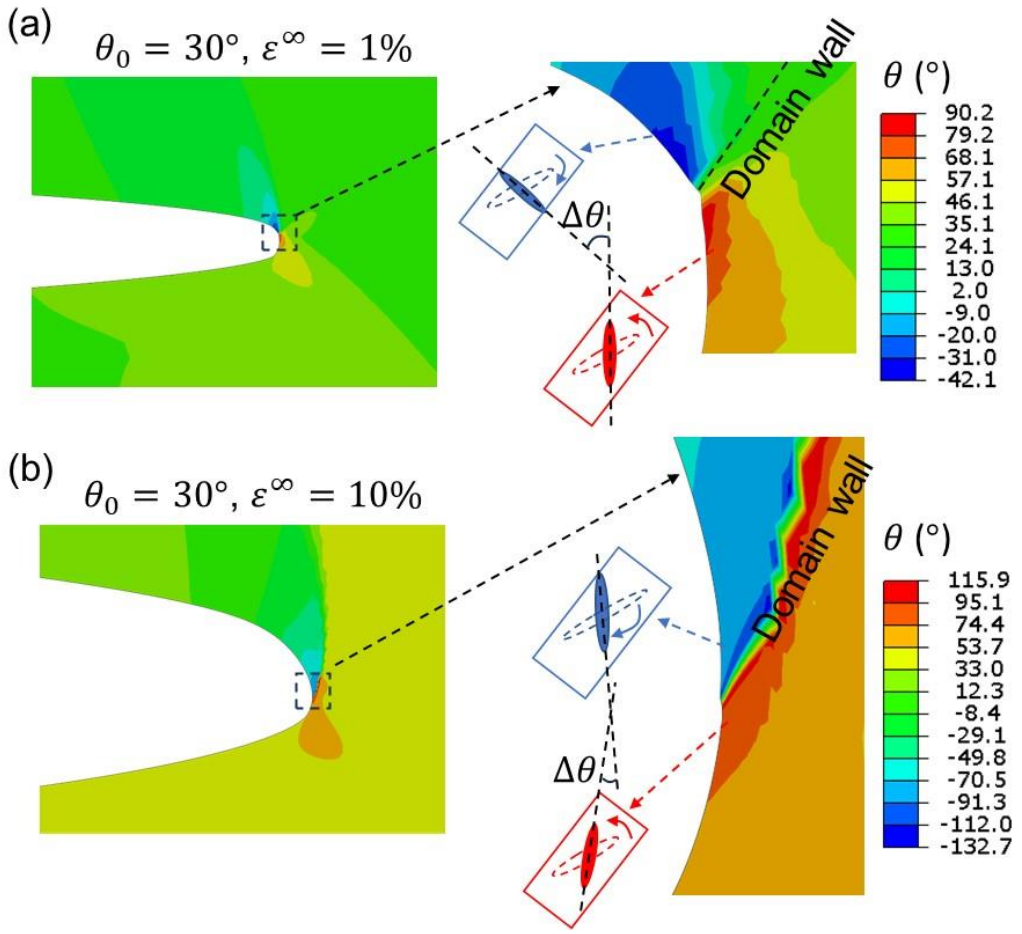

Figure 3.10 FEM results of the director distribution around the crack tip showing the formation of a domain wall. (a) Distribution of the director near the domain wall for the LCE with $\theta_0 = 30°$ at (a) $\varepsilon^\infty = 1\%$ and (b) $\varepsilon^\infty = 10\%$, along with schematics showing the directors adjacent to the domain wall before (dashed hollow cylinders) and after (solid cylinders) deformation. An obvious crack surface discontinuity is observed at $\varepsilon^\infty = 1\%$, accompanied by a large difference in the director alignment across the domain wall, $\Delta\theta$, while the discontinuity is reduced with the difference almost vanishing at $\varepsilon^\infty = 10\%$.

Such strong stress-director coupling in LCEs results in their director rotation distinct from the realignment of fibers in fiber-reinforced elastomer [98]. We denote the portion of director rotation simply following the deformation gradient, similar to fiber realignment, as

$\left(\cos\left(\theta_{Fd_0}\right), \sin\left(\theta_{Fd_0}\right), 0\right) = \boldsymbol{Fd_0}/|\boldsymbol{Fd_0}|$, and plot the angle difference $\left|\theta - \theta_{Fd_0}\right|$ in Figure 3.11. Although the difference is relatively small in remote regions due to limited deformation, and at the crack tip, where exceptionally large deformation prevails, the difference becomes considerably pronounced around and behind the crack tip, see Figure 3.11(a,d,g,j) and Figure 3.11(b,e,h,k). This difference becomes increasingly obvious as the applied strain grows from 2% to 10%. In contrast to the condition in the remote and crack tip areas, the large angle difference in these regions is attributed to the moderate deformation the material experiences. Consequently, the directors in these regions still need to undergo further rotation in order to align with the principal stress direction. The difference between the director rotation and fiber reorientation indicates the distinctively strong stress-director coupling in LCEs.

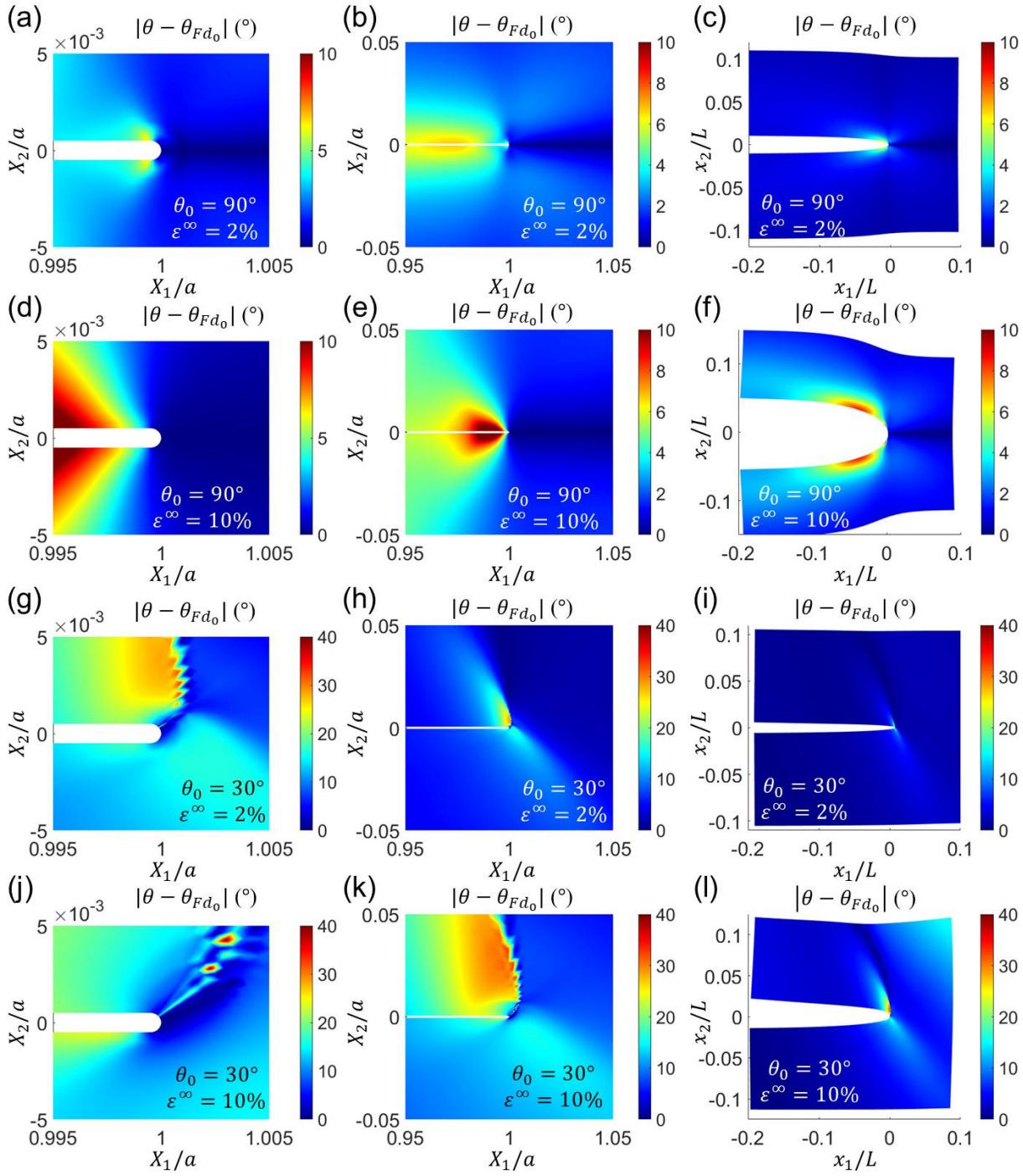

Figure 3.11 FEM simulation results of the angle difference $|\theta - \theta_{Fd_0}|$. θ_{Fd_0} is defined as $(\cos(\theta_{Fd_0}), \sin(\theta_{Fd_0}), 0) = \boldsymbol{Fd_0}/|\boldsymbol{Fd_0}|$, denoting the portion of the director rotation following the

deformation gradient. The angle difference $\left|\theta - \theta_{Fd_0}\right|$ for LCEs with (a-f) $\theta_0 = 90°$ and (g-l) $\theta_0 = 30°$ at (a-c, g-i) $\varepsilon^{\infty} = 2\%$ and (d-f, j-k) $\varepsilon^{\infty} = 10\%$, respectively, shown in different regions.

3.4 Experimental Measurement of Director and Displacement

3.4.1 Director Measurement via the Crossed-polarized Optical Measurement

To validate our simulations, we fabricated LCEs and characterized the director rotation driven by slow stretching sufficiently close to equilibrium. The crossed-polarized optical measurement was employed to measure the transmitted light intensity, which was used to calculate the director; see Section 3.2.2.3. More details about the experimental method were elaborated in our previous study [62]. Figure 3.12 shows the measured director contour from the experiment in comparison with the corresponding FEM simulation results at $\varepsilon^{\infty} = 10\%$. In general, the director near the crack tip exhibits a significantly larger rotation compared to the remote regions.

The experimental observations confirm the occurrence of opposite director rotation near the crack tip. In the case of a LCE with $\theta_0 = 90°$ (Figure 3.12a and b), near the crack tip, the director rotates clockwise at $\phi < 0°$ and counter-clockwise at $\phi > 0°$; far behind the crack tip, the director rotates counter-clockwise at $\phi < 0°$ and clockwise at $\phi > 0°$; in remote regions, the director remains close to $90°$ due to the parallel loading. For the cases of LCEs with $\theta_0 = 30°$, $45°$ and $60°$ (Figure 3.12(c-h)), a sharp transition in director is observed near the crack tip at a critical ϕ angle, verifying the existence of a domain wall. When ϕ is larger than the critical angle, the director rotates clockwise, while when ϕ is smaller than the critical angle, the director rotates counter-clockwise, contrary to the behavior exhibited by LCEs with $\theta_0 = 90°$. Comparison between the optical measurement and simulations reveals a high level of agreement

of the director near the crack tip. The simulations show higher maximum values, which is attributed to the different resolutions of the experimental and simulation tools, i.e. the optical measurement has a resolution of ~0.047 mm/pixel, whereas the element size at the crack tip in the simulations is around 0.0025 mm. Therefore, our simulations provide results in closer proximity to the tip, naturally yielding higher maximum values.

We also find non-monotonic director distributions along the distance from the crack tip, ρ/a, at $\phi = 0°$ (Figure 3.13). The LCE with $\theta_0 = 90°$ shows little director rotation ahead of the crack tip due to the parallel loading. Conversely, in the LCE with $\theta_0 = 60°$, the director rotation decreases monotonically with the distance ρ/a. However, in the LCEs with $\theta_0 = 30°$ and $45°$, the director rotation non-monotonically decreases and then increases with ρ/a. This peculiar observation can be attributed to the inhomogeneous principal stress distribution at the crack tip and the remote region, which is significantly influenced by the initial director. Close to the crack tip, the director aligns tangentially to the crack opening surface resulting in a substantial director reorientation. Consequently, the observed decrease in the director rotation with increasing ρ/a is ascribed to the reduction of stress concentration, and as a result, the director deviates from the tangent direction of the crack surface. As one moves farther away from the crack tip, the director rotation increases again primarily because the director undergoes considerable reorientation to align itself with the remote stretching direction ~$90°$.

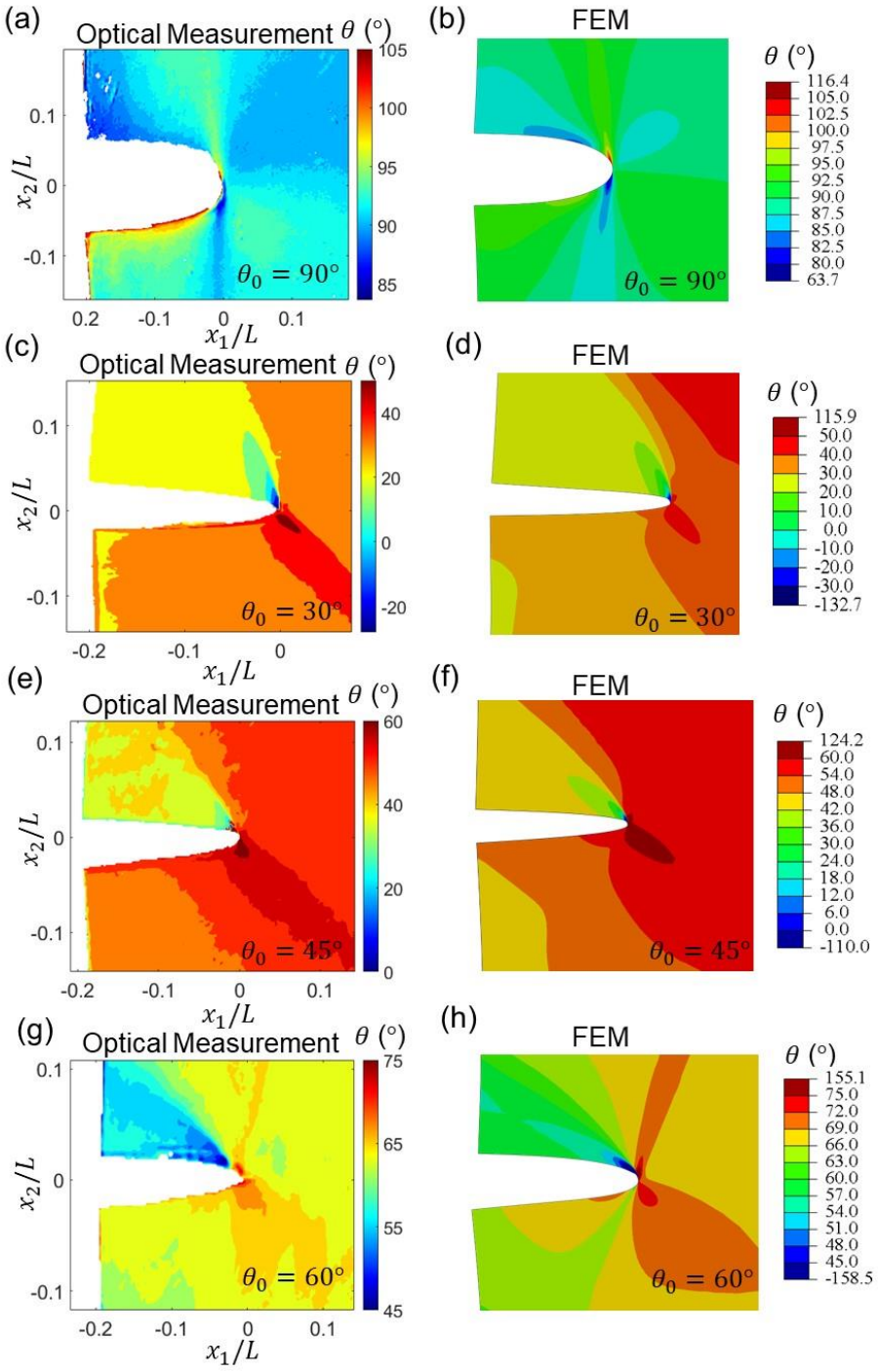

Figure 3.12 Comparing the director fields obtained from the crossed-polarized optical measurements and FEM at $\varepsilon^{\infty} = 10\%$. Director distributions (a, c, e, g) measured by the crossed-polarized optical

measurement and (b, d, f, h) calculated by FEM for LCEs with (a, b) $\theta_0 = 90°$ (c, d) 30°, (e, f) 45°, and (g, h) 60°, respectively.

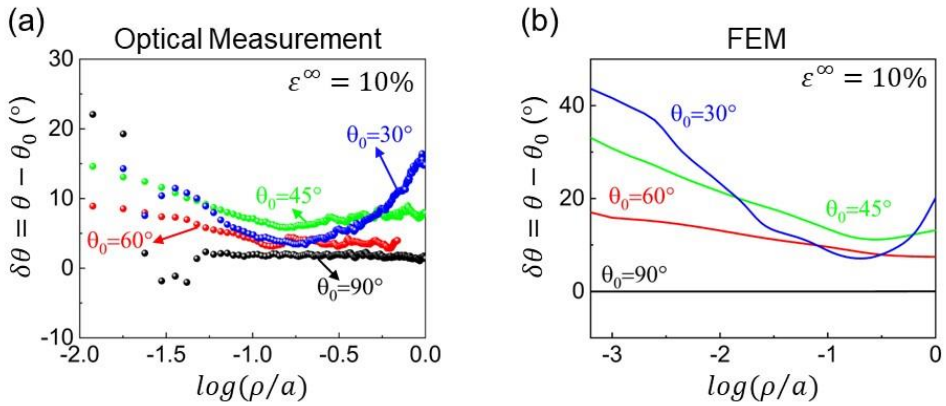

Figure 3.13 Director distributions ahead of the crack tip for LCEs with $\theta_0 = 90°, 60°, 45°, 30°$ obtained by (a) optical measurement and (b) FEM under $\varepsilon^\infty = 10\%$.

3.4.2 Displacement Measurement via Digital Image Correlation (DIC)

The displacement distribution in the edge-cracked LCE samples subjected to external loading was measured using DIC. Figure 3.14a and b illustrate the normalized displacement u_2/L along X_2 with respect to the bottom boundary of the specimen near the crack tip for the LCE with $\theta_0 = 90°$ at $\varepsilon^\infty = 10\%$. Both experimental and FEM simulation results show a symmetrical deformation about $\phi = 0°$, which is consistent with the symmetrical rotation of the director, and in line with the symmetrical deformation of neo-Hookean materials [91]. Not surprisingly, near the crack tip, the maximum deformation, $u_2/L \approx 0.1$, occurs behind the crack tip in the LCE with $\theta_0 = 90°$ due to rigid-body motion on the free surface, while at the crack tip, the displacement is $u_2/L = 0.05$. However, when the initial director is tilted away from the remote strain, u_2/L is no longer symmetrical (Figure 3.14(c-h)). This asymmetric deformation pattern has been indicated in the preceding section to be caused by the asymmetric director

rotation, and consequently the asymmetric spontaneous strain, including the shear components. As θ_0 decreases, the displacement u_2 near the crack becomes smaller due to the bulk director rotation, but meanwhile the location of the maximum displacement shifts to the top-right corner due to severe shear deformation under the confinement of a clamped boundary condition. Figure 3.15 exhibits the displacement u_1/a and u_2/a ahead of the crack tip from DIC and FEM. Upon comparing the DIC and FEM results (Figure 3.14 and Figure 3.15), it is evident that the displacement contours from the simulations closely resemble the experimental findings, thereby validating the theoretical modeling approach.

The crack tip opening displacement is dramatically influenced by the rotation of the director (Figure 3.16). To compare the crack-tip opening displacement, we calculate the difference in movement between the top and the bottom crack surfaces, $\delta u_2 = u_2^{top} - u_2^{bot}$ for LCEs with different θ_0. For the LCE with $\theta_0 = 90°$, the director rotation mainly occurs near the crack ($\phi \neq 0°$, $\rho \to 0$). The spontaneous strain induced by director rotation leads to additional compressive strain normal to the crack surface, so the crack tends to open more than that of a neo-Hookean material. Conversely, for the LCEs with $\theta_0 = 60°$, $45°$ and $30°$, the crack opening is notably smaller than that exhibited by a neo-Hookean material. There are two reasons for the reduced crack opening in LCEs with tilted initial directors. First, the overall director rotation leads to bulk softening. Second, the local director rotation at the crack tip, inducing opposite shear strain around the domain wall, leads to sharp changes on the crack surface and asymmetrical crack opening pattern; see Figure 3.12, where a sharp turning occurs, constraining the extent of the opening. Meanwhile, the director rotation direction is reversed in comparison to the case of $\theta_0 = 90°$, and consequently, the associated spontaneous strain constrains the opening.

This phenomenon can be proved by examining the deformed FEM elements near the crack tip (Figure 3.17). It becomes evident that the elements in the case of $\theta_0 = 90°$ distort greater than that of a neo-Hookean material, indicating that the associated spontaneous strain facilitates the deformation, while in the case of $\theta_0 = 30°$, the elements display reduced distortion at the same small applied strain ($\varepsilon^{\infty} = 2\%$), suggesting that the different directions of director rotation from those of $\theta_0 = 90°$ impose spontaneous strain that limits deformation. As the director near the crack tip rotates mainly following the deformation at $\varepsilon^{\infty} > 2\%$, the bulk softening starts to dominate the crack opening, resulting in a smaller crack opening for a smaller initial director θ_0. The corresponding deformation of the FEM elements at $\varepsilon^{\infty} = 4\%$ (Supplementary Fig. S5) also reveals that in the case of $\theta_0 = 30°$, the elements exhibit significantly less deformation than that of the neo-Hookean material and LCE with $\theta_0 = 90°$ due to the combined contribution of bulk softening and local director rotation.

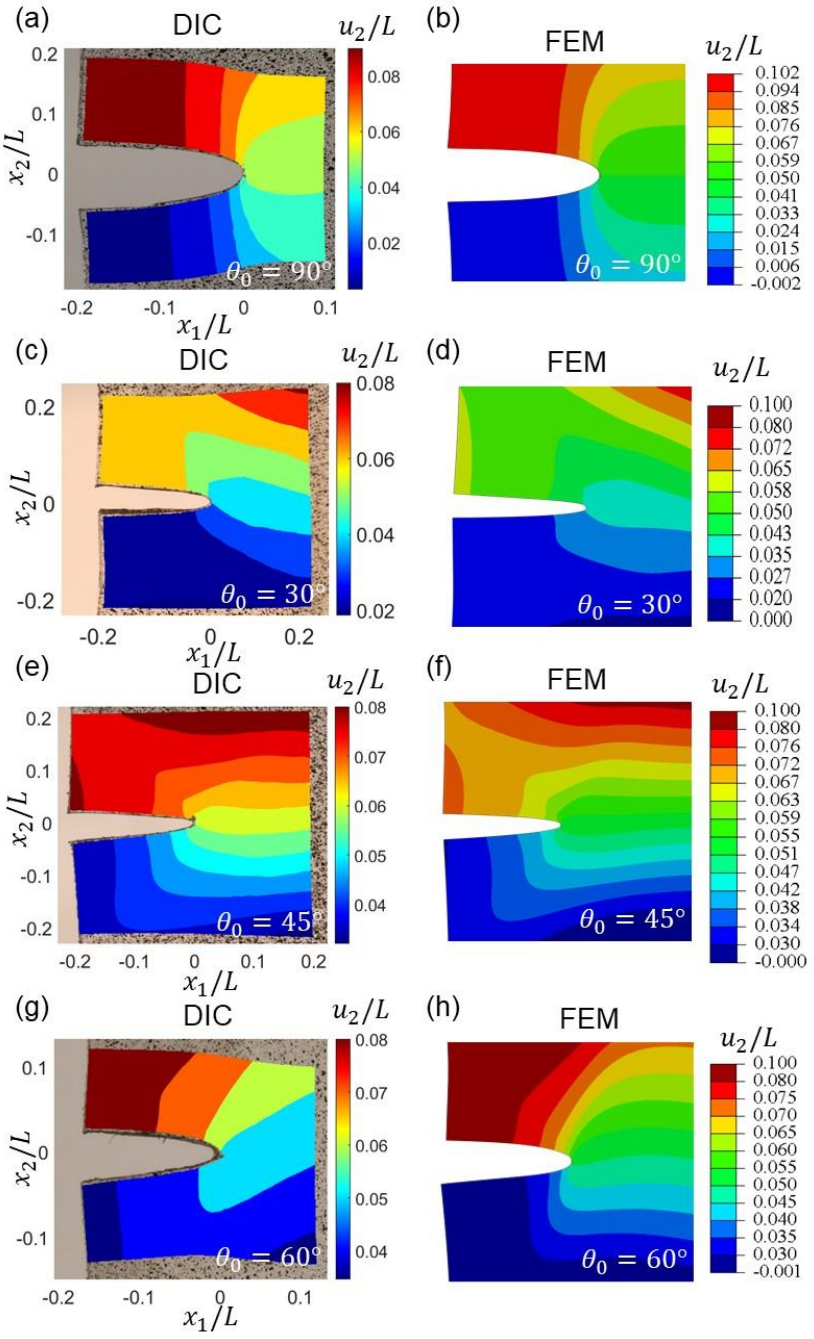

Figure 3.14 Comparing the displacement fields from DIC and FEM. The distribution of the normalized displacement u_2/L around the crack of the LCEs with (a, b) $\theta_0 = 90°$, (c, d) 30°, (e, f) 45° and (g, h) 60° at $\varepsilon^{\infty} = 10\%$ from (a, c, e, g) DIC and (b, d, f, h) FEM.

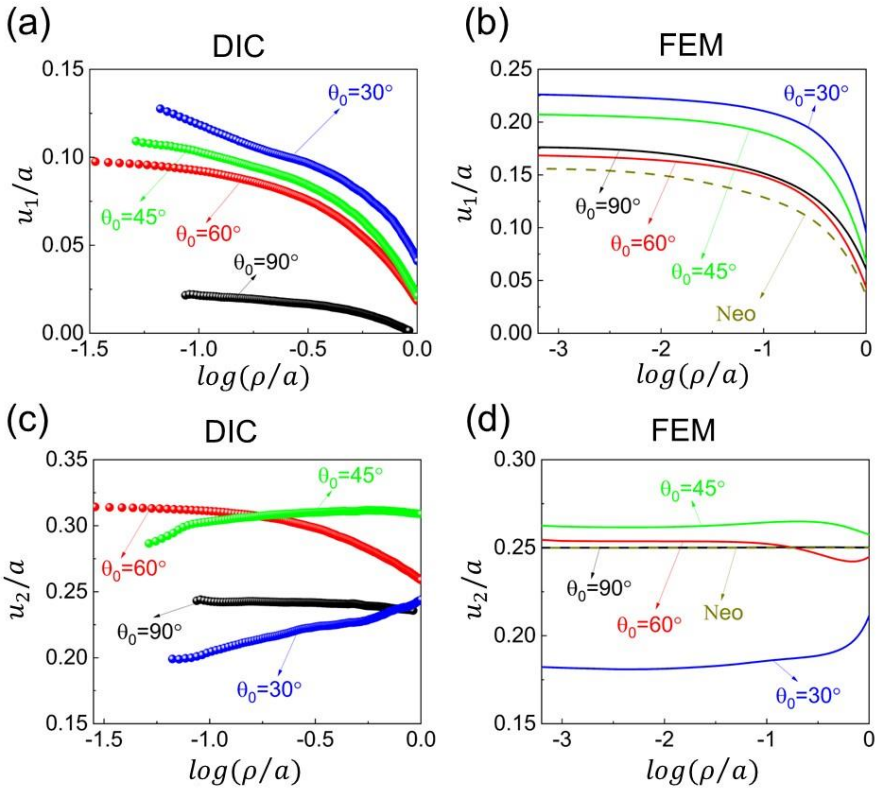

Figure 3.15 Displacement distributions ahead of the crack tip at $\varepsilon^{\infty} = 10\%$. Normalized displacement (a, b) u_1/a and (c, d) u_2/a ahead of the crack tip for LCEs with $\theta_0 = 90°, 60°, 45°, 30°$ obtained from (a, c) DIC and (b, d) FEM. The simulation and experiment results show a consistent trend for LCEs with different initial directors.

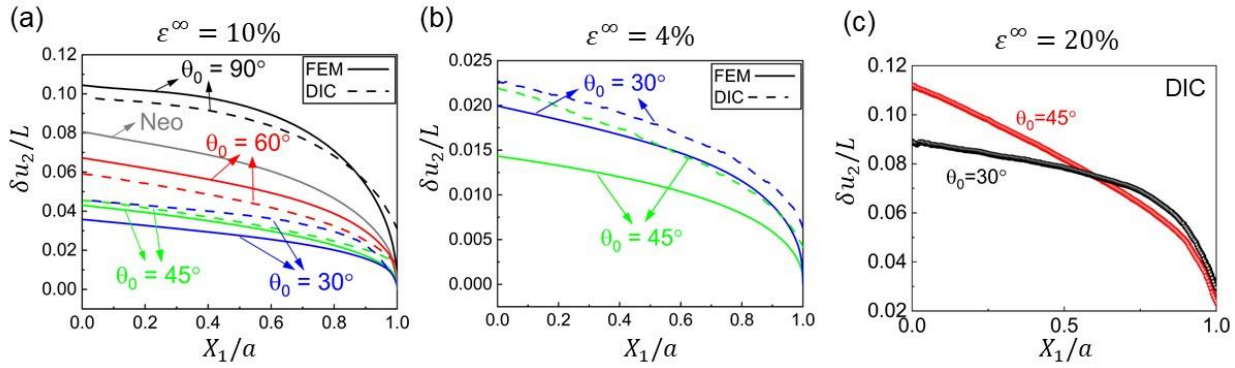

Figure 3.16 Crack opening displacement. Normalized crack tip opening displacement $\delta u_2/L$ from the DIC (dashed lines) and FEM (solid lines) for the LCEs with different θ_0 at (a) $\varepsilon^\infty = 10\%$ and (b) 4%. (c) Normalized crack tip opening displacement $\delta u_2/L$ measured from DIC for the LCEs with $\theta_0 = 30°$ and $45°$ at $\varepsilon^\infty = 20\%$.

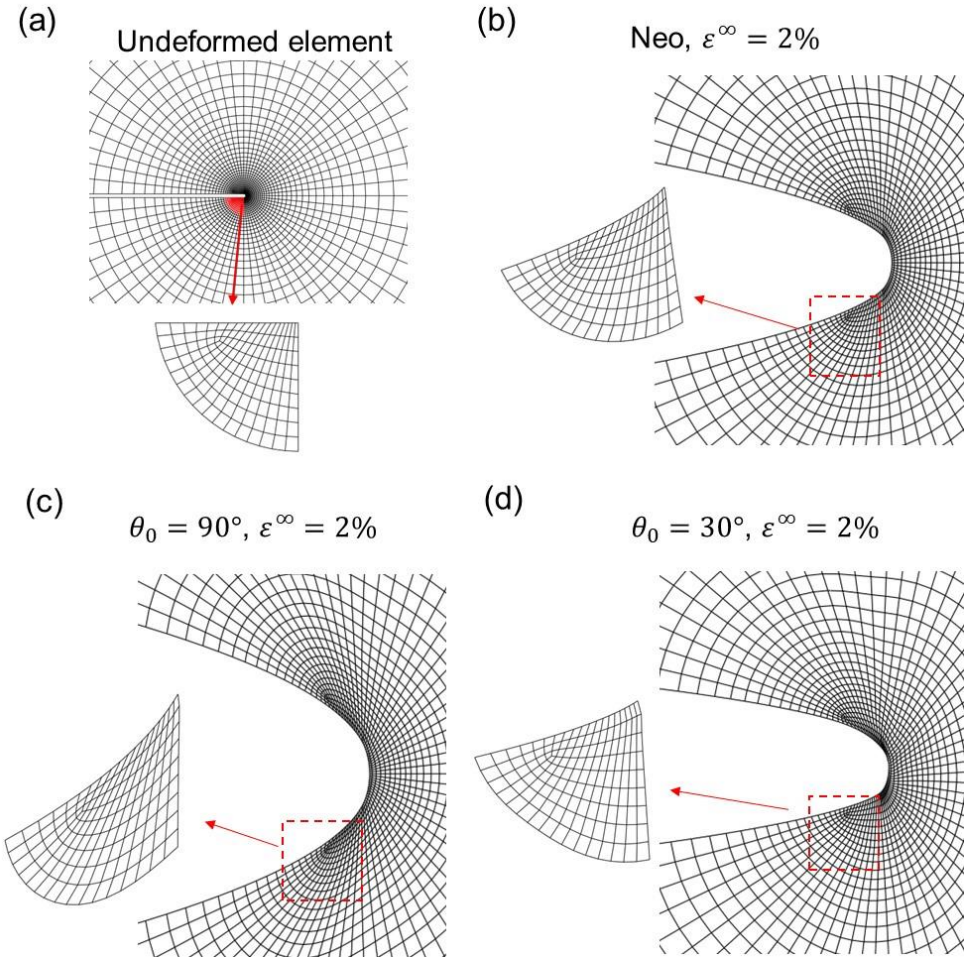

Figure 3.17 Comparing the deformation of the FEM elements around the crack tip for LCEs and neo-Hookean materials at $\varepsilon^\infty = 2\%$. (a) Undeformed elements. Crack opening and element deformation at $\varepsilon^\infty = 2\%$ for (b) a neo-Hookean material and a LCE with (c) $\theta_0 = 90°$ and (d) $\theta_0 = 30°$.

It is evident that the crack opening displacement measured for the LCE with $\theta_0 = 30°$ is smaller than that of $\theta_0 = 45°$ at a high remote strain $\varepsilon^\infty = 20\%$ (Figure 3.16c and

Supplementary Fig. S6), but interestingly, it is larger than that of $\theta_0 = 45°$ at a relatively low remote strain $\varepsilon^\infty = 10\%$ and 4% (Figure 3.16b). The simulation results present the same trend as the experiment, although in the simulations the crack opening displacement for the LCE with $\theta_0 = 45°$ surpasses that of $\theta_0 = 30°$ at a smaller strain between 4% and 10%. Drawing upon the findings by Peng et al. [53] that LCEs with $\theta_0 = 45°$ exhibits the minimized stress concentration factor, we postulate that at a small strain the magnitude of the crack opening is predominantly influenced by the director near the crack tip, and consequently, the director rotation in the LCE with $\theta_0 = 45°$ reduces its crack opening more compared to LCEs with other initial directors. As the remote strain increases, the bulk softening plays a more dominant role in affecting the crack opening, and therefore, the LCE with $\theta_0 = 30°$, which has a stronger bulk softening due to director rotation, has a smaller crack opening than that of $\theta_0 = 45°$. The competition of the two factors leads to the positive-to-negative transition of the difference in the crack opening between the LCEs with $\theta_0 = 30°$ and $\theta_0 = 45°$ as the remote strain increases.

3.5 Evaluation of Fracture Behavior

To evaluate the fracture behavior, we analyze the stress ahead of the crack tip and the energy release rate for LCEs with different initial directors. We plot the Cauchy stress σ_{22} as a function of the distance from the crack tip, ρ/a, at $\varepsilon^\infty = 10\%$ in Figure 3.18a, and compare with that of a neo-Hookean material and a linearly elastic material [99]. In general, LCEs present a similar stress distribution to that of a neo-Hookean material. The LCE with $\theta_0 = 90°$ displays slightly lower stress values compared to the neo-Hookean case. We postulate that this discrepancy arises from the stress redistribution caused by the reorientation of the director in the LCE. Specifically, the director along $\phi = 0°$ undergoes limited rotation, while more director

rotation occurs at $\phi > 0°$ and $\phi < 0°$. Consequently, the material along $\phi = 0°$ behaves stiffer than the surrounding regions, leading to stress redistribution, and resulting in lower stress values compared to those of a neo-Hookean material. For LCEs with tilted initial directors, significant director rotation occurs, inducing large spontaneous strain, resulting in considerably lower stress values. It is important to note that when the initial director is tilted relative to the applied strain, the maximum stress may not be located at $\phi = 0°$ as described in the previous sections. Therefore, the crack propagation may not follow the direction of $\phi = 0°$. To gain a deeper understanding of the fracture behavior, further investigations are required to observe and analyze the crack propagation, which will be discussed in the next Chapter.

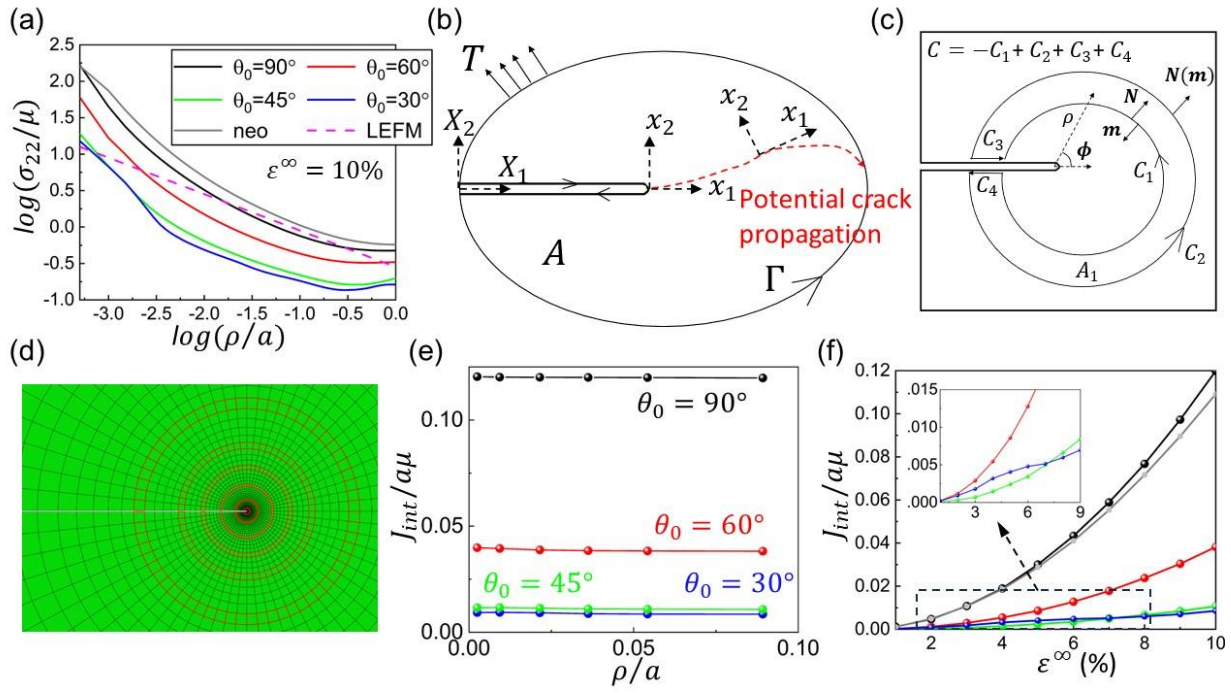

Figure 3.18 Stress distribution ahead of crack tips and J-integral. (a) Normalized Cauchy stress distribution ahead of the crack tips for the LCEs of $\theta_0 = 30°, 45°, 60°$ and 90°, a neo-Hookean material, and a linearly elastic material at $\varepsilon^{\infty} = 10\%$. (b) Schematics of a contour to evaluate the J integral and potential crack trajectory in the reference configuration. (c) Region A_1 enclosed by the contour $C =$

$-C_1 + C_2 + C_3 + C_4$ and (d) five different integral paths around the crack tip are highlighted in the FEM model to calculate the J-integral. (e) Normalized J-integral based on six paths of different ρ/a, verifying its path-independency for LCEs. (f) Normalized J_{int} as a function of the remote strain ε^{∞} for the LCEs with $\theta_0 = 30°, 45°, 60°$ and 90°, and a neo-Hookean material. (f) shares the same legend as (a).

Under the plane strain condition, we further calculate the energy release rate in a two-dimensional LCE. Consider a 2D deformed LCE body, as shown in Figure 3.18b. We eliminate the dissipation energy while calculating the energy release rate due to extremely small values of viscosity. In the absence of the body force, the energy release rate G is defined as the change in the total potential energy per area of the crack growth:

$$G = -\frac{dU}{da} = -\int_A \frac{df_r}{da} dA + \int_\Gamma T_i \frac{du_i}{da} dS, \quad (3.10)$$

where U is the total potential energy defined as $U = \int_A f_r dA - \int_\Gamma \boldsymbol{T} \cdot \boldsymbol{u} dS$, with $f_r(\boldsymbol{F}, \boldsymbol{d}, \nabla \boldsymbol{d})$ the elastic energy density of a LCE, $\boldsymbol{T}$ the prescribed surface traction on the boundary Γ in the reference configuration, and A the total area of the body in the reference configuration. Introduce a coordinate system $x_i = X_i - a\delta_{i1}$ (i =1, 2), where the origin of $\boldsymbol{x}$ locates at the crack tip in the current configuration Figure 3.18b. Although for a LCE with a tilted director, the crack trajectory may not conform to the horizontal direction, we assume it is smooth, so at the onset of propagation, the crack direction still aligns with the $x_1 -$ axis [50]. Based on the chain rule, we get

$$\frac{d}{da} = \frac{\partial}{\partial a} + \frac{\partial x_1}{\partial a}\frac{\partial}{\partial x_1} = \frac{\partial}{\partial a} - \frac{\partial}{\partial x_1} = \frac{\partial}{\partial a} - \frac{\partial}{\partial X_1}. \quad (3.11)$$

Substituting Eqn. (3.11) into Eqn. (3.10) we can calculate G as

$$G = -\int_A \left(\frac{\partial f_r}{\partial \boldsymbol{F}}\frac{\partial \boldsymbol{F}}{\partial a} + \frac{\partial f_r}{\partial \boldsymbol{d}}\frac{\partial \boldsymbol{d}}{\partial a} + \frac{\partial f_r}{\partial \nabla \boldsymbol{d}}\frac{\partial \nabla \boldsymbol{d}}{\partial a} - \frac{\partial f_r}{\partial X_1}\right) dA + \int_\Gamma T_i \left(\frac{\partial u_i}{\partial a} - \frac{\partial u_i}{\partial X_1}\right) dS. \quad (3.12)$$

Then applying the divergence theorem, we can rewrite Eqn. (3.12) to

$$G = -\int_A \left(\frac{\partial f_r}{\partial \boldsymbol{F}}\frac{\partial \boldsymbol{F}}{\partial a} + \frac{\partial f_r}{\partial \boldsymbol{d}}\frac{\partial \boldsymbol{d}}{\partial a} - div_X\left(\frac{\partial f_r}{\partial \nabla \boldsymbol{d}}\boldsymbol{F}^{-\boldsymbol{T}}\right)\frac{\partial \boldsymbol{d}}{\partial a} - \frac{\partial f_r}{\partial X_1}\right)dA - \int_\Gamma \left(\frac{\partial f_r}{\partial \nabla \boldsymbol{d}}\boldsymbol{F}^{-\boldsymbol{T}}\right)\boldsymbol{N}\frac{\partial \boldsymbol{d}}{\partial a}dS + \int_\Gamma T_i\left(\frac{\partial u_i}{\partial a} - \frac{\partial u_i}{\partial X_1}\right)dS. \quad (3.13)$$

As $\nabla \boldsymbol{d}$ only exists in the Frank energy, which is considerably small compared to the total elastic energy [24,51]. To simplify the calculation, we eliminate the term associated with $\nabla \boldsymbol{d}$ when evaluating the energy release rate. Using the governing equations (3.6) and (3.7), we can rewrite Eqn. (3.13) as the following Eqn. (3.14), which recovers the classical form of the J-integral, although now $\boldsymbol{d}$ is a new independent variable in the free energy density of LCEs

$$G = J_{int} = \int_\Gamma \left(f_r N_1 - S_{iJ}N_J\frac{\partial u_i}{\partial X_1}\right)dS, \quad (3.14)$$

where $\boldsymbol{N}$ is the outward normal to the path Γ in the reference configuration and $\boldsymbol{S} = \partial f_r/\partial \mathbf{F}$ is the first Piola–Kirchhoff stress. Eqn. (3.14) not only holds true for the boundary of the body in the path integration, but also remains valid for any arbitrary path from the bottom crack surface to the top crack surface [96,100], so Γ can be denoted as an arbitrary path.

In FEM, it is more convenient to conduct an area integration than a line integration, so we convert Eqn. (3.14) to an area integration [101]. Now consider a closed curve denoted by $C = -C_1 + C_2 + C_3 + C_4$ that bounds an area A_1 with a outward normal vector $\boldsymbol{m}$ (Figure 3.18c). Based on the divergent theorem, the line integration of the J-integral, Eqn. (3.14), over the contour C can be rewritten as

$$J_{int} = \int_{A_1}\left(-f_r\frac{\partial q}{\partial X_1} + S_{iJ}\frac{\partial u_i}{\partial X_1}\frac{\partial q}{\partial X_J}\right)dA, \quad (3.15)$$

where q is a sufficiently smooth function varying from unity on C_1 to zero on C_2; $\boldsymbol{m}$ is the outward unit vector normal to C. Therefore, $\boldsymbol{m} = -\boldsymbol{N}$ on C_1 and $\boldsymbol{m} = \boldsymbol{N}$ on C_2. The integrals

along C_3 and C_4 are zero as no surface traction on the crack surface and $m_1 = 0$. Therefore, Eqn. (3.15) and Eqn. (3.14) are equivalent. Applying the divergence theorem, we get an area integral J_{int}

$$J_{int} = \int_{A_1}(-f_r \frac{\partial q}{\partial X_1} + S_{iJ} \frac{\partial u_i}{\partial X_1} \frac{\partial q}{\partial X_J})dA. \quad (3.16)$$

The path-independency of the J-integral is presented in Figure 3.18e, where the domain integral is computed at $\varepsilon^{\infty} = 10\%$ for various contours C_1 of different distances ρ/a (Figure 3.18d). We calculate the J-integral for LCEs with different initial directors (Figure 3.18f). Generally, a smaller θ_0 leads to a lower J_{int}. However, the LCE with $\theta_0 = 30°$ shows higher J_{int} than that of $\theta_0 = 45°$ at a small remote strain $\varepsilon^{\infty} < \sim 7\%$; conversely, it shows a lower J_{int} at a large remote strain $\varepsilon^{\infty} > \sim 7\%$, similar to the trend of the crack opening displacement. We propose that a combined effect of bulk softening in the remote region and the director rotation near the crack tip influences both the J-integral value and crack displacement opening. Specifically, at a small remote strain, the energy release rate is dominated by the substantial director rotation occurring around the crack tip; conversely, at a high remote strain, the energy release rate is dominated by the overall director rotation. Compared to the behavior of neo-Hookean materials, LCEs under parallel loading present slightly higher J_{int}, while LCEs with tilted stretching consistently show significantly smaller J_{int}. The deviation of J_{int} of LCEs from that of neo-Hookean materials is primarily attributed to the inhomogeneous stress redistribution caused by the director rotation to the direction of the local principle stress around the crack tip and in the remote region. As previously demonstrated in Chapter 2, LCEs exhibit softer behavior as the initial director deviates more from the loading direction. As a result, the stress distribution becomes intricate, as LCEs exhibit different levels of softening around the crack tip due to

varying director reorientation. This phenomenon gives rise to highly inhomogeneous stress, strain and director in the vicinity of a crack tip, leading to higher ($\theta_0 = 90°$) or lower ($\theta_0 = 30°, 45°$ and $\theta_0 = 60°$) J_{int} than that of neo-Hookean materials.

3.6 Conclusion

In this work, we combine simulations and experiments to provide a comprehensive investigation of the unique crack-tip fields of LCEs with various initial directors induced by their stress-director coupling behavior. We limit ourselves to obvious crack blunting but without crack propagation in this study. From FEM simulations, we predict inhomogeneous and significant director reorientation of LCEs, which leads to unique stress and strain distributions in contrast to those in traditional neo-Hookean materials; in experiments, we successfully measure the displacement field by the DIC and the inhomogeneous director reorientation by the optical polariscopic method, validating the findings in the FEM simulations. Based on the consistent results from the FEM and experiments, we reveal the unexpected occurrence of opposite director rotation near the crack tip of LCEs, and dramatically different energy release rates and crack opening displacements of LCEs from traditional elastomers.

Since the unique mechanical responses of a LCE are mainly governed by its director rotation, we demonstrate that the initial director can significantly influence its crack-tip fields and fracture behavior. For an edge-cracked LCE subjected to stretching parallel to its director, the director near the crack tip rotates clockwise at the polar angle $\phi < 0°$ and counter-clockwise at $\phi > 0°$, inducing a spontaneous strain field symmetric about the crack, and resulting in smooth and elliptical-shaped stress/strain contour lines. In contrast, for an edge-cracked LCE with a tilted initial director with respect to the loading, the director undergoes rotation throughout

the bulk sample, while exhibiting more substantial rotation near the crack tip. A domain wall is observed along a critical polar angle; the director rotates clockwise in the region with a larger polar angle and counter-clockwise in the region with a smaller polar angle. The director rotates significantly in the vicinity of the domain wall, resulting in elliptical stress/strain contour lines with the smoothest gradient direction close to the critical polar angle, and consequently, the stress/strain is no longer symmetrical about the crack. As the tilted angle θ_0 increases, the critical polar angle of the domain wall increases, and the crack opening decreases. Compared to a neo-Hookean material, a LCE with a director parallel to stretching, $\theta_0 = 90°$, exhibits a higher energy release rate and larger crack opening, while a LCE with a tilted director presents a much lower energy release rate and smaller crack opening primarily caused by bulk softening induced by overall director rotation. Interestingly, director rotation around the crack tip can be non-monotonic, because at a small strain the director undergoes rapid rotation and tends to align to the local principal stress direction; after the director aligns with the principal stress direction, the director rotates gradually following the macroscopic deformation as the strain further increases.

This work provides a valuable understanding on the director, stress and strain distributions in the vicinity of a crack tip of LCEs, which offers insights into designing LCEs with enhanced fracture properties for long-time applications. The findings and methodology presented in this work lay a solid foundation for further investigation of fracture behavior in LCEs, taking into account their viscoelasticity and crack propagation. Although in this work we load LCEs slowly enough to reach quasi-equilibrium states, LCEs are highly viscoelastic [24,39,47], involving multiple relaxation time scales of network relaxation and director rotation. It will be intriguing to investigate the rate-dependent crack-tip fields and fracture behavior for

LCEs with different initial directors. Furthermore, based on the stress/strain contour lines obtained from this work, it is conceivable to predict that the crack propagation paths in LCEs with different θ_0 can be quite different. Specifically, it is expected that a tilted crack path occurs when the initial director is tilted from the loading direction, which will be discussed in the next chapter.

Chapter 4 Crack Propagation in Post-cut Experiments

Crack growth is a pivotal topic in failure analysis. Most studies on the dynamics of crack propagation in LCEs have focused on polydomain or monodomain under parallel or perpendicular loading, where the crack propagates perpendicular to the precut. However, the feasibility to apply traditional pure shear tests to LCEs with initial directors inclined to the loading direction is questionable, given the observation of tilted crack propagation paths. There is limited information on how the stress-director coupling effect influences crack propagation. To address these challenges, we use a post-cut method in this chapter to report intriguing stress-director crack propagation behavior of LCEs with varying initial directors under different pre-stretching levels. The results show the director-dependent propagation direction, with cracks typically propagating perpendicular to the director ahead of the crack tip, verifying the previous assumptions by Yu et al.[55]. Notably, in a LCE with the initial director $\theta_0 = 30°$ and a 30% pre-stretch, the crack initially propagates in an opposite direction, preferentially initiating at the site of the strip domains. It then reorientates perpendicular to the director. We attribute this unexpected phenomenon to the lower fracture energy of the strip domains compared to monodomain regions. Additionally, the initial crack growth is delayed, which becomes more significant when the director is tilted and the pre-stretching level is low, followed by steady-state growth. As pre-stretching increases, crack rates increase at a steady stage. Furthermore, a phase-field model is utilized to elucidate the underlying mechanism. This study provides valuable insights into the relationship between crack propagation and various initial directors. The sophisticated nature of fracture growth, particularly involving the tilted initial director and the

emergence of strip domains, challenges the characterization capabilities of traditional measurement techniques.

4.1 Introduction

The unique rate-dependent fracture energy of LCEs under different loading directions has been reported [54,60,61,102]. Through pure-shear tests, a polydomain LCE exhibits higher fracture energy than a monodomain LCE. Furthermore, in monodomain LCEs, the fracture energy is lower under perpendicular loading compared to parallel loading. However, when the initial director is inclined relative to the loading direction, the crack path could become tilted [55,63]. Wei et al.[63] studied asymmetric stress/strain distributions ahead of the crack tip in LCEs with tilted directors. Later Yu et al. [55] reported tilted crack propagation in a LCE with an inclined angle between the initial director and the loading direction. These findings suggest that the traditional 'pure shear' method [90] could not be universally applicable to LCEs. Moreover, due to the complex stress-director coupling, conventional methods such as J-integral under mixed-mode tension or crack tip opening displacement fail to provide accurate assessment [50,103]. In response, our focus shifts to analyzing crack growth rates and trajectories, aiming to offer valuable guidance to further develop the fracture criteria of LCEs.

The post-cut method, frequently employed in studies of viscoelastic soft materials [104–107], is used to capture the crack propagation rates. This method offers several advantages: it reduces the impact of bulk dissipation and allows the samples to be stretched further compared to a pre-cut sample. In most soft materials, a sudden increase in velocity with increasing pre-stretching is observed, along with a characteristic power-law relationship between the crack growth rates and energy release rate [105,108,109]. Despite the extensive research on the

fracture behavior of other soft materials, the crack growth mechanics in LCEs remain underexplored. In this study, we will explore if the crack propagation behavior of LCEs under post-cut distinguishes from these typical patterns. Particularly, we will experimentally validate the assumption by Yu et al.[55], which posits that crack propagation in LCEs perpendicular to the director.

The phase-field model is a widely adopted method for numerically predicting crack propagation, offering a smooth transition between intact and fractured material by introducing a damage variable, thereby avoiding discontinuities associated with sharp cracks [110–116]. This approach enables the prediction of rate-dependent crack growth by incorporating the intrinsic viscoelastic material constitutive model and rate-dependent fracture energy [117]. Furthermore, post-fracture behavior has been analyzed within the phase-field framework by tuning the damage variable [118]. Recently, Yu et al. [55] developed a phase-field model to describe a LCE with different initial directors and loading rates, accurately predicting crack paths by assuming that cracks propagate perpendicular to the director. In this study, we utilize a phase-field model following the work of Yu et al.[55], to investigate the post-cut fracture behavior of LCEs with different initial directors.

In this chapter, we examine the crack growth of LCEs with varying directors and pre-stretching levels in post-cut experiments. The unique stress-director coupling in LCEs results in crack propagation patterns that differ significantly from those in conventional soft materials, exhibiting a heavy dependence on the director reorientation. Our results find that the crack typically propagates perpendicular to the director ahead of the crack tip. At low pre-stretching levels and with a substantial deviation between the initial director and the loading direction, an

obvious strip domain forms near the crack tip. In this special case, the crack initiates in the strip domain and then turns perpendicular to the director, a phenomenon likely due to the lower fracture energy in the strip domain compared to the monodomain. We document the crack rates at the steady stage, observing an increase in velocity with higher pre-stretching levels. An initial crack growth delay is observed and the phenomena become more obvious when the pre-stretching level is low and the initial director deviates from the loading direction a lot. To further elucidate the fracture mechanism, we utilize a simplified phase-field model. This study provides critical insights into the relationship between crack propagation and the directors, aiming to advance the development of fracture criteria specific to LCEs.

This chapter is organized as follows. In section 4.2, we introduce experimental methodology including material preparation, the post-cut method, and the measurement for crack propagation. We present the experimental results of crack propagations in section 4.3. In section 4.4, we report a simplified phase-field model and the numerical simulation results. Section 4.5 concludes the chapter.

4.2 Experimental Methodology

4.2.1 Sample Fabrication

In this study, the main-chain monodomain LCEs were synthesized via a two-stage thiol-acrylate Michael addition-photopolymerization (TAMAP) reaction [66]. The crosslinker, pentaerythritol tetrakis(3-mercaptopropionate) (PETMP, 95%) was obtained from Sigma-Aldrich and chain extender, 2,2-(ethylenedioxy) diethanethiol (EDDET, 95%) was purchased from TCI. The chemicals were used as received. The diacrylate mesogen, 1,4-Bis-[4-(3-arcyloyoxypropyloxy) benzoyloxy]-2-methylbenzene (RM257, 95%), was purchased from

Daken Chemical Limited company. Dipropylamine (DPA, 98%) and (2-hydroxyethoxy)-2-methylpropiophenone (HHMP, 98%) were selected as the catalyst and photoinitiator to enable the second-stage photopolymerization reaction, respectively. Additional butylated hydroxytoluene (BHT) was obtained from Sigma-Aldrich to slow down the first polymerization process. Toluene (98%) was used as the solvent for RM257.

To prepare a sample, 8 g RM257 and 0.06 g BHT were fully dissolved in a vial with 3.2 g toluene at 80 ℃. Then, 0.4332 g PETMP, 1.8314 g EDDET, and 0.0514 g HHMP were poured into the solution and mixed using a vortex mixer for 90 s to obtain a uniform solution. After the solution cooled down to room temperature, 1.136 g DPA solution (DPA: toluene = 1:50) was added to the solution and mixed for another 60 s. The molar ratio of thiol functional groups between PETMP and EDDET was 15:85, corresponding to a ratio of 15 mol% PETMP. The molar ratio of DPA with respect to the thiol functional group was 1 mol%, while the molar ratio of HHMP was 1 mol%. The solution was degassed for about 2 minutes to remove all bubbles and then poured into a mold. Then the samples were cured at room temperature for 12 hours and put into an oven at 80 ℃ for 24 hours. At this stage, thiol-acrylate formed a loose network and the sample showed an opaque appearance at room temperature. There would be an excess of 15 mol% acrylate groups for a second-stage photo-crosslinking reaction. In the second stage, the LCE sample was stretched uniaxially to 110% strain by a tension machine. The pre-stretch forced mesogens to reorientate to the tension direction, and the sample became transparent, indicating a monodomain LCE. The pre-stretched sample was exposed to UV light for 1 hour to photopolymerize the excessive acrylate groups, forming a denser network. After releasing the samples from the stretcher, a thin film of monodomain LCE sheet remains.

4.2.2 Post-cut Method

LCEs specimens were cut in a dogbone shape with various initial directors θ_0 relative to $X_1 - axis$ as shown in Figure 4.1a. We did not use a conventional 'pure shear' shape, characterized by a high aspect ratio of length over height, due to the inherent difficulties in accurately determining the fracture energy like traditional soft materials [90]. One difficulty comes from the tilted crack propagation direction due to director reorientation. Another reason is even in cases of monodomain LCEs under perpendicular loading, where crack propagation is horizontal, the samples experience significant contraction during tension, necessitating a considerably greater width than that needed for conventional soft materials to fulfill pure-shear testing conditions. Instead, we focus on the crack propagation velocities and trajectories. We prepared samples with a height of 20 mm and a width of 30 mm at the central region (Figure 4.1a). The terminal ends of the samples are designed with an expanded profile, featuring a radius of 10 mm, to mitigate the risk of rupture at the clamping ends during testing. The stress concentration at the two ends is more pronounced compared to traditional soft materials due to the spontaneous strain arising from LCs' reorientation. This effect is particularly significant for LCEs with initial directors close to $\theta_0 = 45°$ (Figure 4.1a): under tension in the X_2 direction, the principal stress direction is perpendicular to the LCs alignment at the upper left and lower right corners, allowing significant rotation of LCs and inducing substantial spontaneous strain; conversely, at the lower left and upper right corners, where the principal stress direction is closer to the initial director, failure is more likely to happens due to the limited contribution from spontaneous strain.

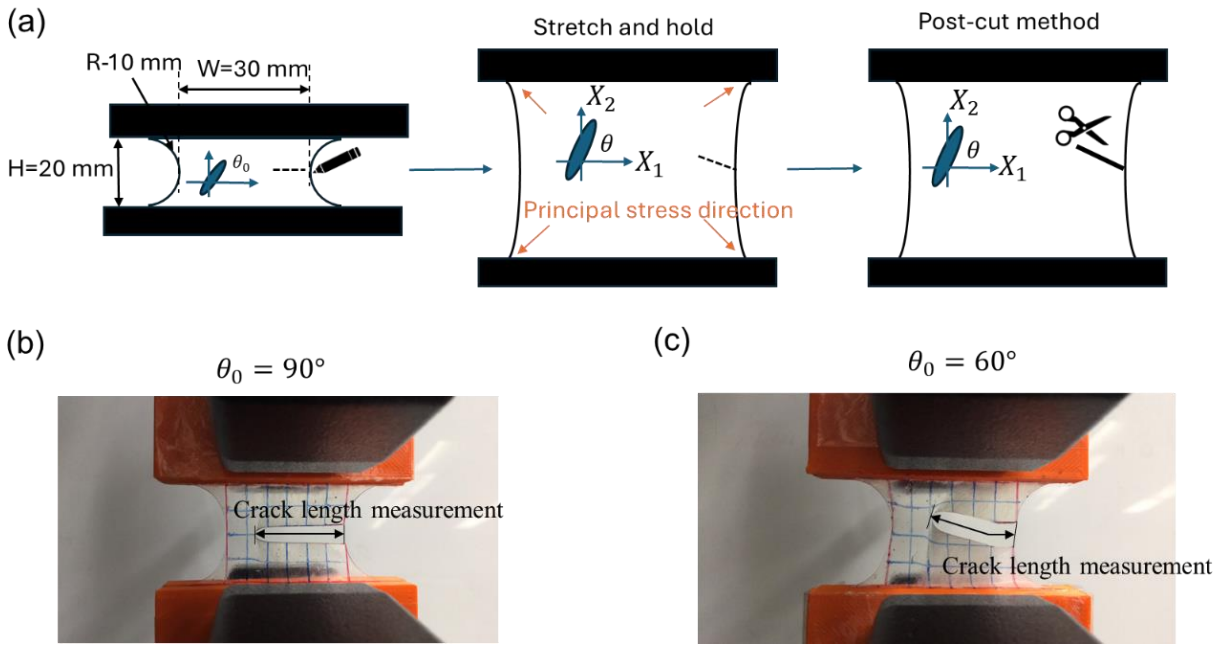

Figure 4.1 (a) Schematic of the post-cut method. Pictures of crack propagation and schematic of crack length measurement of LCEs with the initial director (b) $\theta_0 = 90°$ and (c) $\theta_0 = 60°$

Figure 4.1a shows the post-cut process. At first, we marked a 5 mm horizontal cutting line along $X_1 - axis$ at the middle of the edge, ensuring the initial crack is identical for all cases in the undeformed configuration. Secondly, the sample was glued onto the ABS (Acrylonitrile butadiene styrene) plates via a superglue, and the plates were clamped onto the grip of an Instron universal testing machine (Model 5944) equipped with a 50 N load cell. Then, the sample was stretched at the rate of 0.5 mm/s to the predetermined strain along $X_2 - axis$ and held. The pre-stretching levels were carefully controlled to ensure that crack initiation occurs only after cutting while preventing failure in the clamping. In this study, pre-stretching levels of 20%, 25%, and 30% were applied for $\theta_0 = 90°$ and $\theta_0 = 60$, while 30%, 40%, 50%, and 60% were used for $\theta_0 = 30°$. After 1 hour, we used scissors to cut along the marked line. This duration is based on the previous study that LCEs reach a near-equilibrium after 1 hour [62], even though evidence

has shown that complete equilibrium is not achieved even after several days of relaxation [39]. The cutting line could be tilted due to shear strain induced by LCs' reorientation.. A slow-motion video setup records the crack propagation. Crack length is measured from the camera captures the image at a rate of 30 frames per second. Figure 4.1b and Figure 4.1c present examples of crack length measurement when the crack propagates horizontally and tiltedly, respectively.

4.2.3 Crossed-polarized Optical Measurement

Director rotation driven by stretching was characterized by crossed-polarized optical measurements. A light source, a polarizer, a specimen stretched by the Instron universal testing machine, an analyzer with the polarization perpendicular to the polarizer, and a camera were set up in the order described in Section 2.2.3 (Figure 2.2).

4.3 Experimental Results and Discussion

4.3.1 Crack Growth Rate

We first investigate a LCE with the initial director parallel to the loading direction ($\theta_0 = 90°$), as depicted in Figure 4.2. Figure 4.2a shows the stress response as a function of time. After one hour of holding, the stress curve becomes flat, indicating the material has nearly relaxed. A sharp drop of stress is observed upon introducing a post-cut, after which the stress gradually decreases to zero. The rate of stress decline accelerates with higher pre-stretching levels, reflecting faster crack propagation. Figure 4.2b presents the normalized crack length following the cut, with the slope of the curves representing the crack growth rates. LCEs exhibit delayed initial growth, resulting in an initial flat segment in the crack length. The phenomena become more pronounced under low pre-stretching levels. This delay crack may be attributed to the long-

time relaxation of LCEs, viscous fracture energy [119,120], and crack nucleation [121]. Then crack grows at a faster and constant rate. With the pre-stretching levels set at 30%, 25%, and 20%, the crack rate decreases from approximately 0.0098 mm/s to 0.0048 mm/s and finally to 0.0015 mm/s. For a lower pre-stretching level (20%), the crack rate decreases at the end due to the boundary effects.

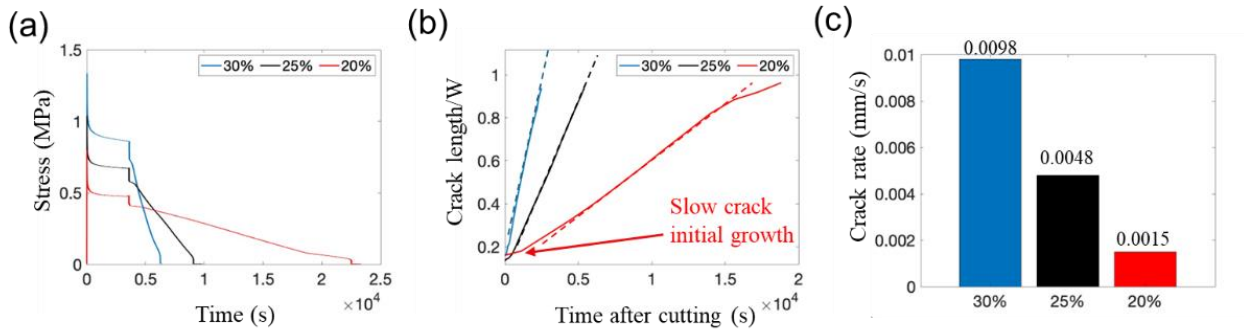

Figure 4.2 The stress and crack growth for a LCE with $\theta_0 = 90°$ after pre-stretching at 30%, 25% and 20%. (a) Stress as a function of time. (b) The normalized crack length as a function of time after cutting. (c) the crack rates at a constant growth stage.

When the initial director is inclined to the loading direction, as shown in Figure 4.3, stress-director coupling results in distinct crack growth dynamics. For LCEs with $\theta_0 = 60°$, the crack propagation rate is slower compared to the parallel case ($\theta_0 = 90°$) at the same pre-strethcing levels. Specifically, at pre-stretching levels of 30%, 25%, and 20%, the crack growth rates are 0.0058 mm/s, 0.0028 mm/s, and 0.0012 mm/s, respectively. While at the low pre-stretching level (20%), the crack rate is pretty close in these two cases. Crack propagation occurs in two distinct stages: - an initial slow phase followed by a faster, steady growth phase. The delayed initial crack growth becomes more obvious compared to parallel cases. This phenomenon is more pronounced at $\theta_0 = 30°$ (Figure 4.3e).

Such intriguing behavior is likely attributed to two factors. First, it arises from the highly viscous nature of director rotation and network deformation. When a crack is introduced, the redistribution of stress and strain around the crack tip requires time. In cases where the initial director significantly deviates from the loading direction, the director at the crack tip undergoes substantial rotation, forming a domain wall that restricts the crack opening [63]. Additionally, the reorientation of the director induces extra energy dissipation compared to the parallel case, thereby reducing the available energy to overcome surface energy and slowing crack growth. The second factor could be the effect of the strip domain, particularly at low pre-stretching levels. Around the crack tip, strip domains and monodomains, with different material properties, coexist. This coexistence leads to a complex stress/strain distribution at the crack tip, slowing down the crack propagation. A more detailed discussion is provided in section 4.3.3.

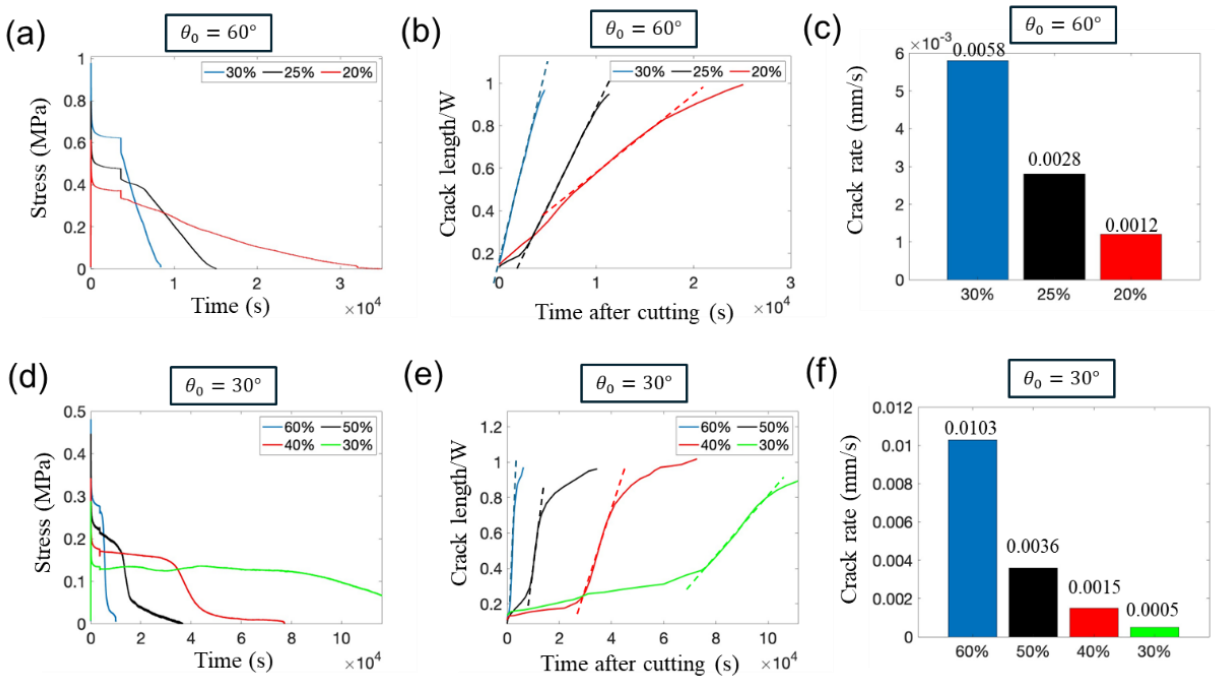

Figure 4.3 The stress and crack growth for a LCE with (a)-(c) $\theta_0 = 60°$ and (d)-(f) $\theta_0 = 30°$ after pre-stretching. (a)(d) Stress as a function of time, (b)(e) the normalized crack length as a function of time after

cutting, and (c)(f) the crack rates at a constant growth stage, in LCEs with $\theta_0 = 60°$ and $\theta_0 = 30°$, respectively.

For LCEs with $\theta_0 = 60°$ (Figure 4.3(d-e)), greater pre-stretch is required due to the global spontaneous strain, necessitating a higher stretch to initiate the crack growth. The crack growth process in these cases can be categorized into three stages: delayed crack growth at the beginning, constant crack growth, and a deceleration phase due to the boundary effect. At pre-stretching levels of 60%, 50%, 40%, and 30%, the crack growth rates are approximately 0.0103 mm/s, 0.0036 mm/s, 0.0015 mm/s, and 0.0005 mm/s, respectively. Interestingly, these rates follow a near power-law relationship with the pre-stretching levels, resembling the behavior observed in conventional soft materials, where crack growth rates exhibit a power-law dependency on the energy release rate [106,107]. However, further experimental investigation is required to confirm the relationship.

4.3.2 Crack Propagation Direction

The stress-director coupling in LCEs results in a remarkably different crack propagation trajectory compared to conventional soft materials. In typical soft materials, the crack generally follows the path of the pre-existing horizontal crack upon initiation. However, in LCEs, the presence of stress-director coupling leads to deviations from the expected crack path.

Figure 4.4 presents the crack trajectory of LCEs with varying initial directors in the undeformed configuration. In all cases, the initial crack is cut horizontally along $X_1 - axis$ in the reference status. Figure 4.4a exhibits the crack propagation along $X_1 - axis$ in LCEs under parallel loading ($\theta_0 = 90°$), which is similar to the normal soft materials.

In contrast, while the initial director is inclined to the loading direction, as illustrated in Figure 4.4b and c, the crack deflected from the pre-existing horizontal path, tilting toward the positive $X_2 - axis$. In LCEs with $\theta_0 = 60°$, the crack trajectories at pre-stretching levels of 30%, 25%, 20% are nearly identical. For LCEs with $\theta_0 = 30°$, the crack trajectories exhibit variation across different stretching levels. The deviation angles are computed between the crack path and the negative X_1 direction at the middle region of the sample, i.e. steady stage, as an example shown in Figure 4.4c. Figure 4.4d reveals decreasing deviated angles with pre-stretching levels increasing, with values of approximately $27.2°$, $23.6°$, and $22.7°$, for pre-stretching levels of 40%, 50%, and 60%, respectively. Notably, at a pre-stretching level of 30% and $\theta_0 = 30°$, the crack follows an atypical trajectory, initially propagating downward before redirecting upward, which will be discussed in Section 4.3.3.

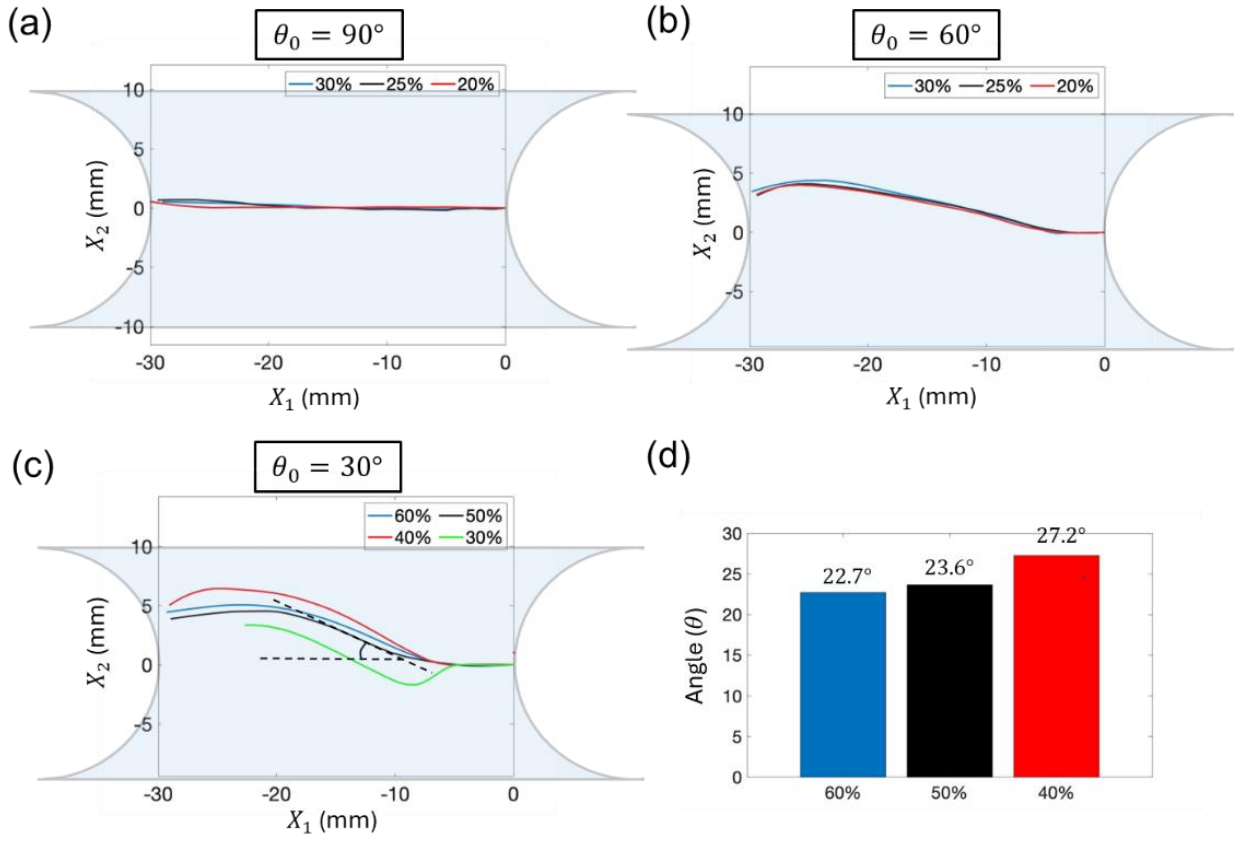

Figure 4.4 The crack trajectories of LCEs in the undeformed configuration with an initial director (a) $\theta_0 = 90°$, (b) $\theta_0 = 60°$ and (c) $\theta_0 = 30°$. (d) The relative crack propagation angle as a function of prestretch strain in LCE with $\theta_0 = 30°$.

To elucidate the intriguing crack propagation path, we record the director distribution during crack propagation through the crossed-polarized optical method, as shown in Figure 4.5. When the initial director is parallel to the loading direction and the pre-stretching level is 25% (Figure 4.5a), the director rotates towards the principal stress direction at four corners during the holding stage. We select two representative moments after cutting. As elaborated in the previous study [63], the director exhibits a clockwise rotation above the crack tip and a counter-clockwise

rotation below the crack tip. Ahead of the crack tip, the director remains $\theta = 90°$, where crack propagates perpendicular to the director, i.e. along $X_1 - axis$.

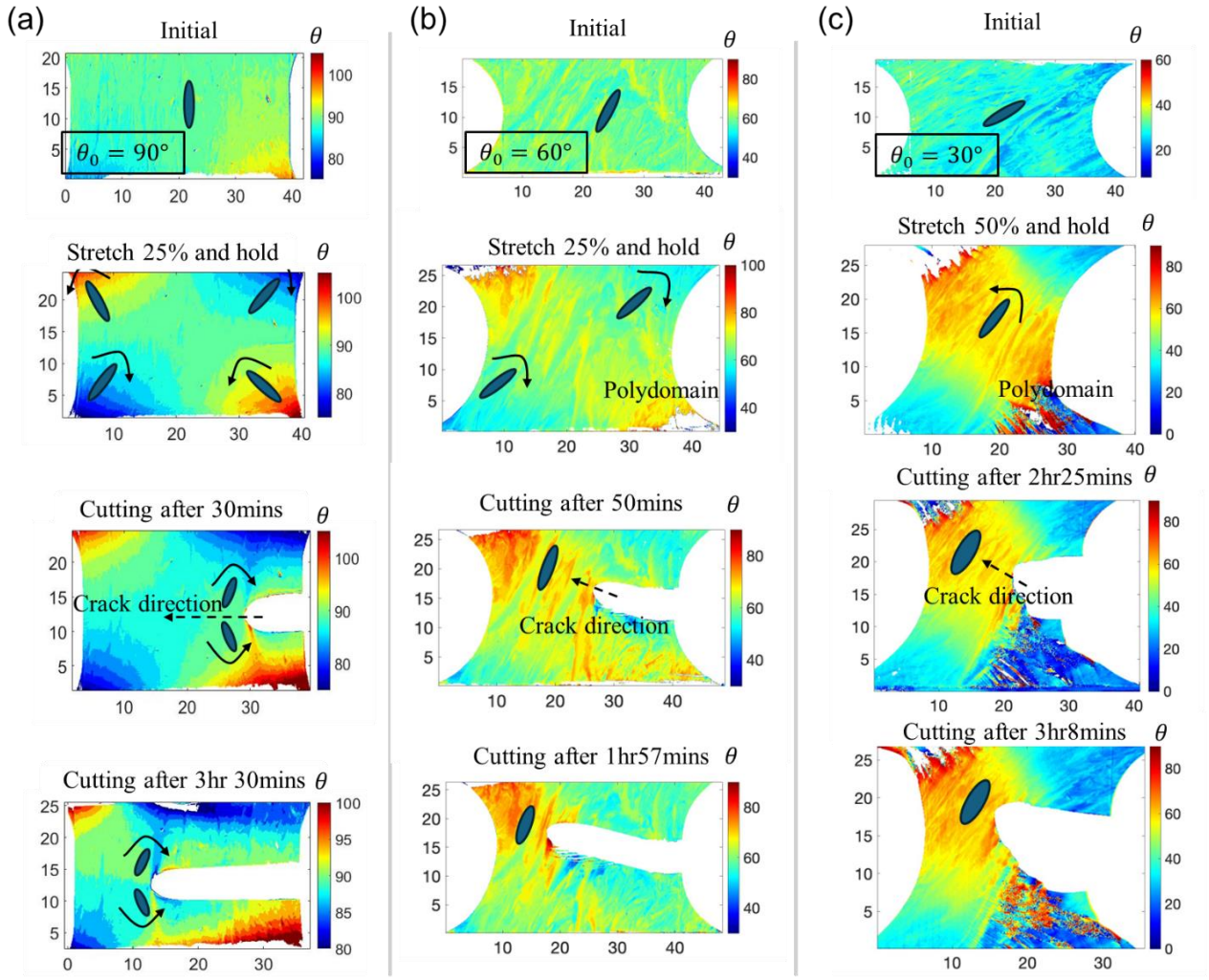

Figure 4.5 Director rotation of LCEs with initial directors (a) $\theta_0 = 90°$, (b) $\theta_0 = 60°$ and (c) $\theta_0 = 30°$ at the stage of initial, holding before cutting, and holding after cutting.

In scenarios where the initial director is tilted relative to the loading direction, as shown in Figure 4.5b and c. At the left top and right bottom corners, the principal stress direction is nearly perpendicular to the initial director, resulting in strip domains during the holding stage. These regions appear opaque, precluding the collection of data due to the absence of light

transmission. At the right top and left bottom corners, the director rotates slightly as the principal stress direction is nearly aligned with the initial director. In the central region, the director rotates counter-clockwise, approaching the alignment with the loading direction, leading to notable sample contraction. After cutting, two representative moments are selected. In the case of $\theta_0 = 60°$, the director ahead of the crack tip is around $70°$, and crack propagates at an angle of about $20°$ relative to the negative $X_1 - axis$; For $\theta_0 = 30°$, the director ahead of the crack tip is around $60°$, and the crack propagates at an angle of about $30°$ relative to the negative $X_1 - axis$. These observation indicate that in both cases, the crack propagates nearly perpendicular to the director ahead of the crack tip.

In general, the observations reveal that the crack typically advances perpendicular to the director orientation ahead of the crack tip, validating the assumption proposed by Yu et al.[55]. This explains the variations in crack trajectories at different pre-stretching levels. In the case of $\theta_0 = 30°$, significant discrepancies arise among the different pre-stretching levels. Higher pre-stretching levels lead to the director rotating to the loading direction, consequently larger deviated angles from the $X_1 - axis$. Given that the crack propagates perpendicular to the director orientation ahead of the crack tip, the crack trajectory becomes more flat with a higher pre-stretching level. In contrast, for LCEs with $\theta_0 = 60°$ and $90°$, the crack trajectories are nearly identical due to limited differences in director rotation across the pre-stretching levels, as the initial director is closely aligned with the loading direction.

4.3.3 The anomalous crack path in a LCE with $\theta_0 = 30°$

In the case of $\theta_0 = 30°$ at a pre-stretching level of 30%, the crack presents anomalous growth, diverging from the typical perpendicular trajectory relative to the director ahead of the

crack tip in other cases. We hypothesize this deviation arises from the formation of a strip domain at the crack tip. The crack initiates in the strip domain, where the fracture energy is comparatively lower.

Figure 4.6 illustrates the crack propagation in a LCE with $\theta_0 = 30°$ at pre-stretching level of 30%. Shortly after cutting (Figure 4.6a), the crack tip, highlighted in a red dot, comprises both monodomain and strip domain regions, which are characterized by their transparent and opaque appearances, respectively. This heterogeneous composition at the crack tip suggests the presence of inhomogeneous mechanical properties. According to the previous study [54,61], the formation of a strip domain ahead of the crack tip during perpendicular loading implies that the fracture energy within a strip domain is reduced compared to the monodomain region. Consequently, the crack initiates within the strip domain.

After a long-time relaxation, the crack tip transitions from the strip domain to the monodomain region (Figure 4.6b and c). This behavior is likely due to the redistribution of stress and strain as the crack approaches the bottom boundary, leading to a shift of stress and strain concentration towards the monodomain regions. Consequently, the crack begins to propagate within the monodomain region, following a path perpendicular to the director, as shown in Figure 4.6d. Notably, no strip domains are observed at the crack tip during propagation perpendicular to the director, see the red dot positioned outside the strip domain regions.

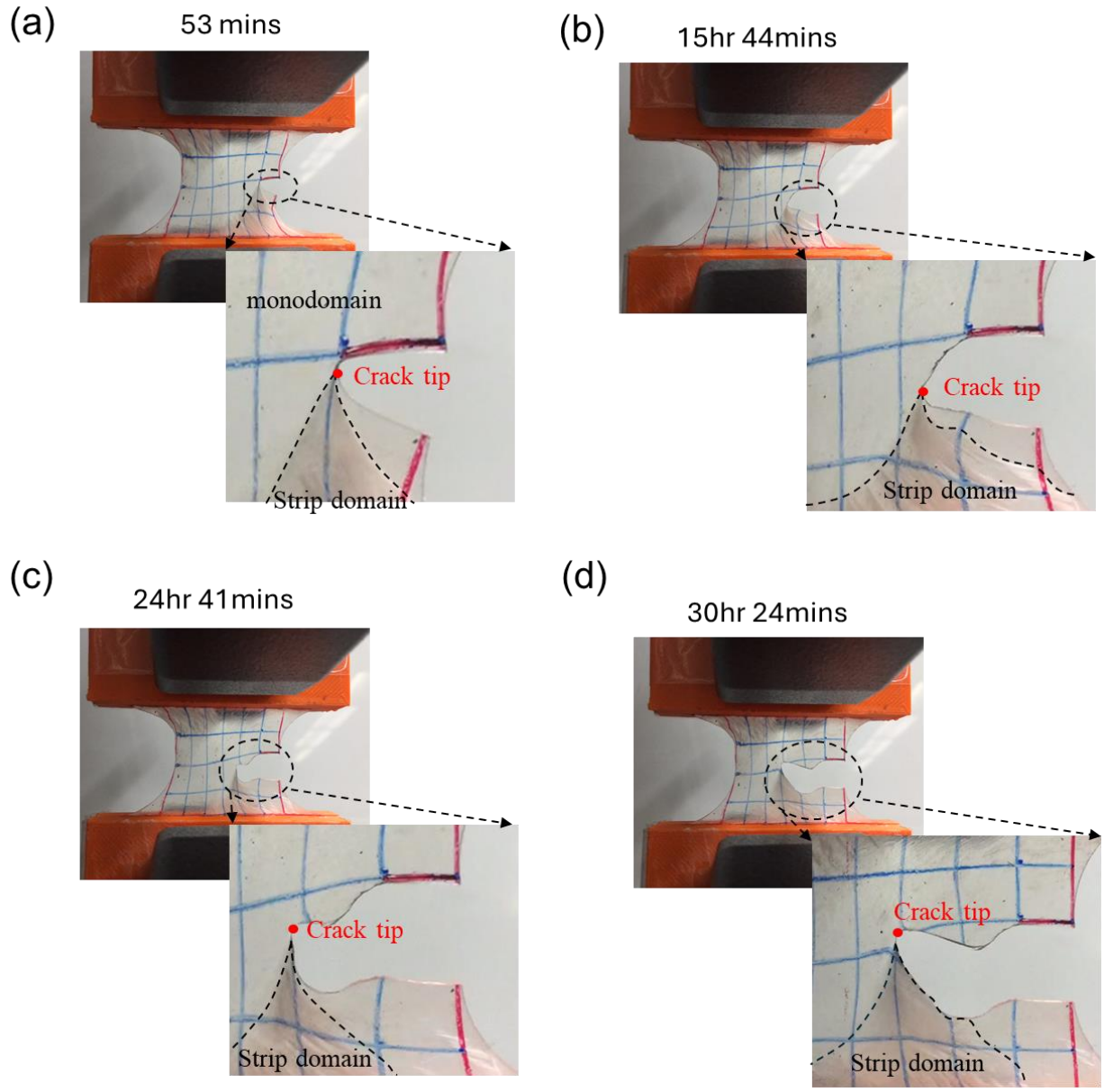

Figure 4.6 Pictures of crack propagations in a LCE with $\theta_0 = 30°$ at pre-stretching level of 30% after (a) 53 mins, (b) 15hr 44 mins, (c) 24hr 41 mins, and (d) 30hr 24 mins cutting.

For $\theta_0 = 30°$ at a higher pre-stretching level, such as 60% shown in Figure 4.7, the crack grows as expected, aligning perpendicularly to the director. Although a strip domain is observed around the crack, it is absent at the crack tip and is restricted to smaller regions due to the higher

pre-stretching. As a result, the crack tip consists entirely of monodomain material, from which the crack initiates. In cases of $\theta_0 = 60°$, a smaller strip domain region (domain wall) also forms near the crack tip but is absent at the tip. Therefore, the strip domains hardly affect the crack propagation direction.

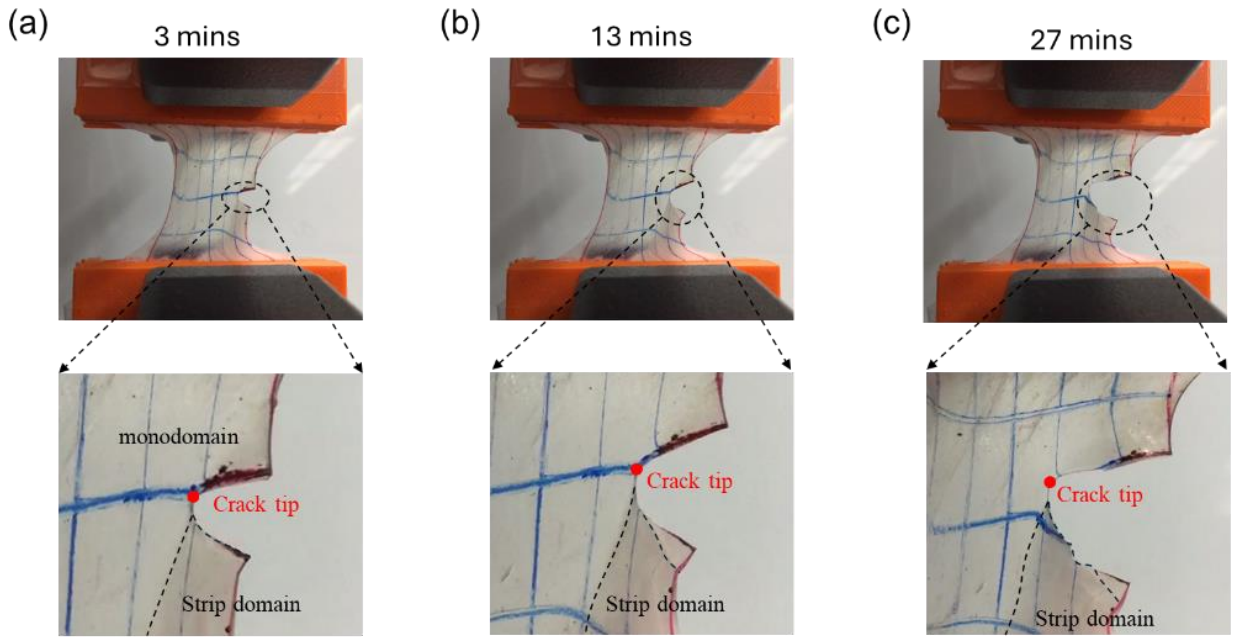

Figure 4.7 Pictures of crack propagations in a LCE with $\theta_0 = 30°$ at pre-stretching level of 60% after (a) 3 mins, (b) 13 mins, and (c) 27 mins.

The formation of strip domains is identified as a potential factor contributing to a more pronounced delay in the onset of crack growth when the initial directors are inclined to the loading direction. In these cases, the materials near the crack tip comprise a combination of strip domains and monodomains. In monodomain regions, the director almost aligns with the principal stretching direction [63], whereas in strip domains, the alignment is absent. As a result, strip domains have more ability to be stretched, which may mitigate stress concentration at the crack tip during their formation, thereby resulting in a more significant delay.

The above findings highlight the need for a more rigorous approach to analyzing the fracture behavior of LCEs. First, the formation of a strip at the crack tip, which may transition into a monodomain as the crack progresses, complicates the prediction of crack growth direction. Particularly when the crack tip consists of both strip domains and monodomain regions at low pre-stretching levels, minor material variation – referred to as natural experimental error - can significantly influence the crack path. Secondly, the fracture criteria may vary depending on the pre-stretching levels and the presence of a strip domain at the crack tip, given different fracture energies in strip domains and monodomain regions. Third, it is a significant challenge to develop accurate models due to the lack of clarity regarding the transition in fracture energy between strip domains to monodomain regions. Further research is required to address these issues and improve our understanding of fracture behavior in LCEs.

4.4 Phase-field Model and Numerical Simulation Results

4.4.1 A phase-field model of LCEs

Following the work by Yu et al.[55], we develop a phase-field model for LCEs. We define a material particle labeled by a position vector $\mathbf{X}$ in the stress-free reference configuration Ω_0 ($\mathbf{X} \in \Omega_0$) moves to the position $\mathbf{x}$ at time t in the current configuration Ω_c ($\mathbf{x} \in \Omega_c$). The deformation gradient is defined as $F_{iK} = \partial x_i(\mathbf{X}, t)/\partial X_K$. A unit vector $\boldsymbol{d}$ is used to describe the director orientation in the current configuration. $\boldsymbol{d} = (cos(\theta), sin(\theta), 0)$ with an angle θ between the director and $X_1 - axis$. As the director relaxes much faster than the network [62], we only consider the viscoelasticity of the network. In this way, the rheological model is composed in parallel of an equilibrium spring, representing the elasticity after viscoelastic relaxation, a Maxwell unit with a non-equilibrium spring and a dashpot connected in series,

describing non-equilibrium behavior, and an additional dashpot (Figure 4.8). In the Maxwell unit, we assume the total deformation gradient $\boldsymbol{F}$ can be decomposed into an elastic part $\boldsymbol{F}_e$ and a viscoelastic part $\boldsymbol{F}_v$, $\boldsymbol{F} = \boldsymbol{F}_e\boldsymbol{F}_v$.

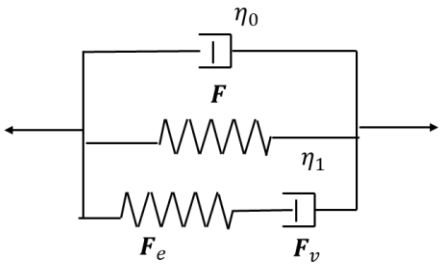

Figure 4.8 Schematic of the rheological model with a viscous branch, an equilibrium branch, and one nonequilibrium branch

Based on the Griffith theory [122], the formation of a crack involves the additional dissipation energy, i.e. fracture energy, to create a new surface. For the isothermal condition, we can write the thermodynamics requirement as

$$\dot{W}_e + \dot{W}_v + \dot{W}_f - \dot{W_{ext}} - \int \gamma_d \boldsymbol{d} \cdot \dot{\boldsymbol{d}}\, dV = 0, \tag{4.1}$$

where W_e, W_v, W_f, W_{ext} are the elastic energy, bulk dissipation energy relative to the viscous network, the fracture energy, and the potential of external work, respectively. $\dot{} = \delta/\delta t$ in $\dot{W}_e, \dot{W}_v$ etc. represents a small variation over a small time increment. γ_d is a Lagrange multiplier to enforce the unit vector constraint of $\boldsymbol{d}$, $\boldsymbol{d} \cdot \boldsymbol{d} \equiv 1$. In the phase field model, we introduce a degradation function $g(\varphi)$ with a scalar variable $\varphi \in [0,1]$ to describe damaged material. We adopt a quadratic degradation function $g(\varphi) = (1-\varphi)^2$ [123]. When $\varphi = 1$, the material is totally ruptured; when $\varphi = 0$, the material is intact. In this way, the elastic energy can be written as

$$W_e = g(\varphi)\int f_r(\boldsymbol{F},\boldsymbol{F_e},\boldsymbol{d})\,dV = g(\varphi)\int (f_r^{eq}(\boldsymbol{F},\boldsymbol{d}) + f_r^{neq}(\boldsymbol{F_e},\boldsymbol{d}))\,dV \tag{4.2}$$

where f_r, f_r^{eq} and f_r^{neq} represent the total, equilibrium, and nonequilibrium free energy density in the reference state, respectively. The equilibrium and nonequilibrium free energy density functions are

$$f_r^{eq} = \frac{\mu^{eq}}{2}(tr\big(\boldsymbol{F}^{eq}\boldsymbol{F}^{eqT} + a(\boldsymbol{I} - \boldsymbol{d_0}\otimes\boldsymbol{d_0})\boldsymbol{F^T}\cdot\boldsymbol{d}\otimes\mathbf{d}\cdot\mathbf{F}\big) - 3 - 2ln(J)) + B(J-1)^2/2, \tag{4.3}$$

$$f_r^{neq} = \frac{\mu^{neq}}{2}\big(tr\big(\boldsymbol{F}^{neq}\boldsymbol{F}^{neqT} + a(\boldsymbol{I} - \boldsymbol{d_0}\otimes\boldsymbol{d_0})\boldsymbol{F_e}^{\boldsymbol{T}}\cdot\boldsymbol{d}\otimes\mathbf{d}\cdot\boldsymbol{F_e}\big) - 3 - 2ln(J^e)\big) + B_e(J^e-1)^2/2, \tag{4.4}$$

where μ^{eq} and μ^{neq} are the shear modulus of the equilibrium and non-equilibrium; B and B_e are the bulk modulus controlling incompressibility. $J = \det(F)$; $J^e = \det(\boldsymbol{F}_e)$; $\boldsymbol{F}^{eq} \coloneqq \boldsymbol{l}^{-1/2}\boldsymbol{F}\boldsymbol{l_0}^{1/2}$; $\boldsymbol{F}^{neq} \coloneqq \boldsymbol{l}^{-1/2}\boldsymbol{F}_e\boldsymbol{l_0}^{1/2}$; a represents the semi-soft parameter, the value of which is kept the same for the equilibrium and non-equilibrium free energy; $\boldsymbol{d}$ and $\boldsymbol{d_0}$ represent the director in the current and reference states, respectively. $\boldsymbol{l}$ and $\boldsymbol{l_0}$ are the corresponding dimensionless shape (metric) tensor, $\boldsymbol{l} = \frac{1}{l_\parallel}((l_\parallel - l_\perp)\boldsymbol{d}\otimes\boldsymbol{d} + l_\perp\boldsymbol{I})$ and $\boldsymbol{l_0} = \frac{1}{l_\parallel^0}\big(\big(l_\parallel^0 - l_\perp^0\big)\boldsymbol{d_0}\otimes\boldsymbol{d_0} + l_\perp^0\boldsymbol{I}\big)$. The effective lengths along or perpendicular to the director ($l_\parallel\ and\ l_\perp$) are assumed to remain constant during deformation. We set ratio $r = \frac{l_\parallel}{l_\perp} = 5.5$ based on the previous study [62].

The dissipation energy comes from two dashpots in Figure 4.8. The dissipation energy is written as

$$W_v = g(\varphi)(\int D_0\,dV + \int D_1\,dV) = g(\varphi)(\int\tfrac{1}{2}\eta_0 J tr(\dot{\boldsymbol{\varepsilon}}^2)\,dV + \int\tfrac{1}{2}\eta_1\dot{\boldsymbol{F}}_v\boldsymbol{F_v^{-1}}\colon\dot{\boldsymbol{F}}_v\boldsymbol{F_v^{-1}}\,dV), \tag{4.5}$$

where the first term (D_0) in the paratheses represents an external dissipation [82], with strain rate tensor $\dot{\boldsymbol{\varepsilon}} = \dot{\boldsymbol{F}}\boldsymbol{F}^{-1}$. The second term ($D_1$) represents the dissipation from the dashpot ($\boldsymbol{F}_v$) in the branch of the Maxwell model (Figure 4.8).

Based on the Griffith energy principles and the crack density function of the phase-field model [111], the fracture energy is approximated as

$$W_f = \int G_c \, d\Gamma \cong \int G_c \gamma(\varphi; \nabla\varphi) \, dV, \tag{4.6}$$

where G_c is the intrinsic fracture energy, which is the same rate-dependent formula as Yu et al.[55] $G_c = [\sqrt{G_{c0}} + \beta \log (r_d/r_{d0})]^2$, where $r_d = \frac{1}{2}\sqrt{(\dot{\boldsymbol{F}}\boldsymbol{F}^{-1} + \boldsymbol{F}^{-T}\dot{\boldsymbol{F}}^T) : (\dot{\boldsymbol{F}}\boldsymbol{F}^{-1} + \boldsymbol{F}^{-T}\dot{\boldsymbol{F}}^T)}$ and β is a scaling factor, and G_{c0} is the reference fracture energy with respect to the reference deformation rate r_{d0}. γ is the surface density function expressed a generic form [124,125] as

$$\gamma = \frac{3}{8}[\frac{1}{b_0}\varphi + b_0 \nabla\varphi \cdot \boldsymbol{A} \cdot \nabla\varphi], \tag{4.7}$$

where $\boldsymbol{A} = \boldsymbol{I} + \alpha_{ani}\boldsymbol{F}^{-1}\boldsymbol{n}_\perp \otimes \boldsymbol{F}^{-1}\boldsymbol{n}_\perp$, with unit vector $\boldsymbol{n}_\perp$ perpendicular to the director and α_{ani} illustrating the coefficient of anisotropy of the fracture energy, is the second-order structural tensor related to the director reorientation derived in a previous study Yu et al. [55]. It controls the crack propagates perpendicular to the director. b_0 is a phase-field length scale, describing the crack dispersion width.

The potential energy of the external work is expressed as

$$W_{ext} = \int \boldsymbol{B}\boldsymbol{u} \, dV + \int \boldsymbol{T}\boldsymbol{u} \, dA. \tag{4.8}$$

Implement eqns (4.2)-(4.8) into eqn (4.1), we obtain

$$\int(\boldsymbol{B}+div_X\left(g(\varphi)\cdot(\frac{\partial f_r}{\partial \boldsymbol{F}}+\frac{\partial f_r}{\partial \boldsymbol{F_e}}\boldsymbol{F_v^{-T}}+\frac{\partial D_0}{\partial \dot{\boldsymbol{\varepsilon}}}\boldsymbol{F^{-T}})\right))\dot{\boldsymbol{u}}dV+\int(\boldsymbol{T}-g(\varphi)\cdot(\frac{\partial f_r}{\partial \boldsymbol{F}}+\frac{\partial f_r}{\partial \boldsymbol{F_e}}\boldsymbol{F_v^{-T}}+$$

$$\frac{\partial D_0}{\partial \dot{\boldsymbol{\varepsilon}}}\boldsymbol{F^{-T}})\cdot\boldsymbol{N})\dot{\boldsymbol{u}}dA+\int(\gamma_d\boldsymbol{d}-g(\varphi)\frac{\partial f_r}{\partial \boldsymbol{d}})\dot{\boldsymbol{d}}dV+\int g(\varphi)\cdot((\boldsymbol{F_e}^T\frac{\partial f_r}{\partial \boldsymbol{F_e}}\boldsymbol{F_v^{-T}}-\frac{\partial D_1}{\partial \dot{\boldsymbol{F}}_{\boldsymbol{v}}}):\dot{\boldsymbol{F}}_{\boldsymbol{v}})dV+ \quad (4.9)$$

$$\int\frac{\partial g(\varphi)}{\partial\varphi}(f_r+D_0+D_1)\dot{\varphi}+G_c\dot{\gamma}\,dV=0,$$

where $\boldsymbol{N}$ is the unit vector normal to any given surface at the reference state. To satisfy the equilibrium equation, every term has to be zero. We define the first Piola-Kirchhoff stress as $\mathbf{S}=g(\varphi)\cdot(\frac{\partial f_r}{\partial \boldsymbol{F}}+\frac{\partial f_r}{\partial \boldsymbol{F_e}}\boldsymbol{F_v^{-T}}+\frac{\partial D_0}{\partial \dot{\varepsilon}}\boldsymbol{F^{-T}})$. Assume no body force and surface force, we can get the force balance equation and traction relation from the first two terms in eqn (4.9) as

$$div_X(\boldsymbol{S})=\mathbf{0}, \quad (4.10)$$

$$-\boldsymbol{S}\cdot\boldsymbol{N}=\mathbf{0}, \quad (4.11)$$

where

$$\boldsymbol{S}=(1-\varphi)^2\cdot\{\mu^{eq}\left(\left(\boldsymbol{l^{-1}Fl_0}\right)+a\boldsymbol{d}\otimes(\boldsymbol{I}-\boldsymbol{d_0}\otimes\boldsymbol{d_0})\boldsymbol{F^T}\mathbf{d}-\boldsymbol{F^T}\right)+BJ(J-$$

$$1)\boldsymbol{F^{-T}}+\mu^{neq}\left(\left(\boldsymbol{l^{-1}F_el_0F_v}^{-T}\right)+a\boldsymbol{d}\otimes(\boldsymbol{I}-\boldsymbol{d_0}\otimes\boldsymbol{d_0})\boldsymbol{F_e}^{\boldsymbol{T}}\mathbf{d}\boldsymbol{F_v}^{-T}-\boldsymbol{F^{-T}}\right)+B_eJ^e(J^e- \quad (4.12)$$

$$1)\boldsymbol{F^{-T}}+\eta_0J\dot{\boldsymbol{\varepsilon}}\boldsymbol{F^{-T}}\},$$

The third term in eqn (4.9) indicates that $\frac{\partial f_r}{\partial \boldsymbol{d}}$ should be in the same direction as $\boldsymbol{d}$, requiring $\boldsymbol{d}\times\frac{\partial f_r}{\partial \boldsymbol{d}}=\mathbf{0}$. Implement eqns (4.3)(4.4), the governing equation for the director field can be expressed as

$$\boldsymbol{s}^{eqd}\times\boldsymbol{d}+\boldsymbol{s}^{neqd}\times\boldsymbol{d}=\mathbf{0}, \quad (4.13)$$

where $\boldsymbol{s}^{eqd}\coloneqq(1-\varphi)^2\mu^{eq}(\left(l_{\parallel}^{-1}-l_{\perp}^{-1}\right)\boldsymbol{Fl_0F^Td}+a\boldsymbol{F}(\boldsymbol{I}-\boldsymbol{d_0}\otimes\boldsymbol{d_0})\boldsymbol{F^Td})$ and $\boldsymbol{s}^{neqd}\coloneqq(1-\varphi)^2\mu^{neq}(\left(l_{\parallel}^{-1}-l_{\perp}^{-1}\right)\boldsymbol{F_el_0F_e}^{\boldsymbol{T}}\boldsymbol{d}+a\boldsymbol{F_e}(\boldsymbol{I}-\boldsymbol{d_0}\otimes\boldsymbol{d_0})\boldsymbol{F_e}^{\boldsymbol{T}}\boldsymbol{d})$.

From the fourth term in eqn (4.9), we obtain the evolution equation $\dot{\boldsymbol{F}}_v = \frac{1}{\eta_1}\boldsymbol{F}_e{}^{-T}\frac{\partial f_r}{\partial \boldsymbol{F}_e}\boldsymbol{F}_v$ for $\dot{\boldsymbol{F}}_e$ ($\dot{\boldsymbol{F}}_v$)

$$\dot{\boldsymbol{F}}_v = \frac{\mu^{neq}}{\eta_1}\left(\boldsymbol{F}_e^T\boldsymbol{l}^{-1}\boldsymbol{F}_e\boldsymbol{l}_0 + a\boldsymbol{F}_e^T\boldsymbol{d}\otimes(\boldsymbol{I}-\boldsymbol{d}_0\otimes\boldsymbol{d}_0)\boldsymbol{F}_e^T\mathbf{d}-\boldsymbol{I}\right)\boldsymbol{F}_v + \frac{B_e}{\eta_1}J^e(J^e-1)\boldsymbol{F}_v. \quad (4.14)$$

In the end, we get the evolution equation for the phase-field variable from the last term in eqn (4.9). Here, based on the findings that the intrinsic fracture energy could be only related to the equilibrium elastic energy [55,57], we write the evolution equation for φ as

$$\frac{\partial g(\varphi)}{\partial \varphi} f_r^{eq}(\boldsymbol{F},\boldsymbol{d}) + G_c\cdot\frac{3}{8}\left[\frac{1}{b_0} - 2b_0\nabla\cdot(\boldsymbol{A}\cdot\nabla\varphi)\right] = 0. \quad (4.15)$$

To prevent the crack from healing, a history variable [126] is introduced as

$$H = \max_{\tau\in[0,t]}\frac{f_r^{eq}(\tau)}{G_c(\tau)}, \quad (4.16)$$

where H is a monotonically non-decreasing function. In this way, the crack evolution equation is rewritten as:

$$-2(1-\varphi)H + \frac{3}{8}\left[\frac{1}{b_0} - 2b_0\nabla\cdot(\boldsymbol{A}\cdot\nabla\varphi)\right] = 0. \quad (4.17)$$

The model is implemented in COMSOL under plane stress condition. The four governing equations (4.10)(4.13)(4.14)(4.17) are implemented using the weak form. Linear Lagrange discretization is utilized for variables of displacement, director, and the phase-field variable. Discontinuous lear Lagrange discretization is used for $\boldsymbol{F}_e$ (or $\boldsymbol{F}_v$). The material parameters of phase-field model are estimated based on experimental observations in Table 4.1 and Table 4.2:

Table 4.1 Mateiral parameters of LCEs

η_0/μ^{eq}	η_1/μ^{eq}	μ^{neq}/μ^{eq}	B/μ^{eq}	B_e/μ^{eq}	a	r
0.5	10	9	100	100	0.08	5.5

Table 4.2 Fracture parameter setting for the phase-field model

b_0(mm)	α_{ani}	G_{co} (N/m)	β $(\sqrt{N/m})$	r_{d0} (s^{-1})
0.2	15	400	0.08	$\sqrt{1.5} \times 10^{-4}$

We build a rectangular model with a width of 30 mm and a height of 20 mm as shown in Figure 4.9. The crack width is 0.1 mm and the mesh size is refined along the crack path also set as 0.1 mm. The bottom boundary is fixed and the top boundary is velocity/displacement-controlled. We pre-stretch the sample at a rate of 0.01%/s and then hold. The pre-stretching stage is quasi-static based on the material parameters in Table 4.1. As we did not build a dogbone-shape model shown in Figure 4.1, we enforced a phase-field variable $\varphi = 0$ at four corners of a rectangular with 10 mm X_1 and 4.5 mm along X_2 to prevent boudanry failure. During pre-stretching, the initial phase-field variable is set $\varphi = 0$ for all regions, ensuring no damage occurs. At the beginning of the holding stage, we manually assign the phase-field variable $\varphi = 0.99$ to the pre-cut crack region, introducing highly damaged material to simulate the post-cut process described in Section 4.2.2. The displacement is maintained, allowing the crack to propagate over time.

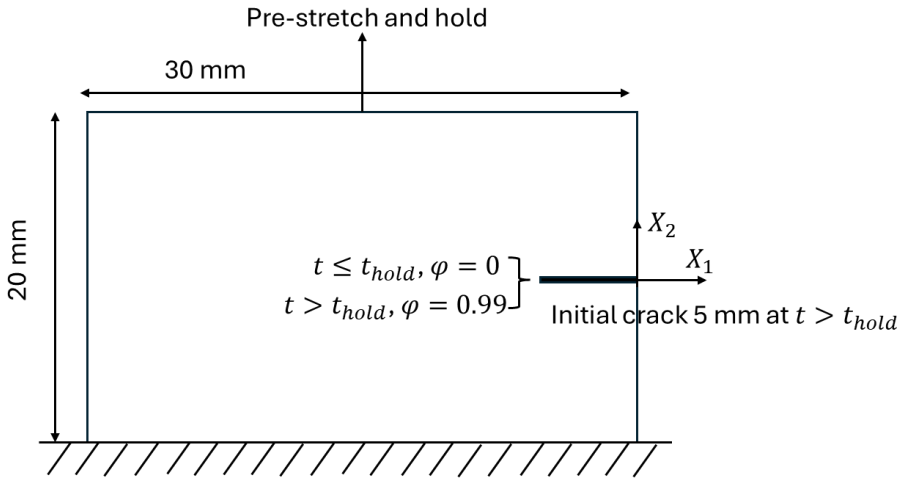

Figure 4.9 Schematic of the phase-field model in COMSOL

4.4.2 Numerical Simulation Results and Discussion

We utilize the phase-field model to further demonstrate the relationship among the crack growth, initial director, and pre-stretching levels.

Figure 4.10a shows the director distribution after cutting in a LCE with $\theta_0 = 90°$ at a pre-stretching level of 30%. The director reorientation is in agreement with the experimental observation shown in Figure 4.5a, exhibiting clockwise rotation above the crack tip and counter-clockwise rotation below it. A slight delay in the initiation of crack growth is observed, particularly at lower is lower pre-stretching levels. Following this initial phase, the crack transitions into a steady growth stage, consistent with the experimental findings (Figure 4.10b). The crack propagation rates during the steady growth phase are plotted in Figure 4.10c, with values of 0.027 mm/s, 0.0080 mm/s, and 0.0016 mm/s at pre-stretching levels of 30%, 25%, and 20%, respectively. The growth rate matches quite well with the experiments (Figure 4.2), especially at the low stretching levels (20%).

Figure 4.10d shows the director distribution following cutting in a LCE with $\theta_0 = 60°$ at a pre-stretching level of 30%. In Figure 4.10e, the initial slow crack growth becomes more obvious compared to the case of $\theta_0 = 90°$, showing a trend consistent with the discussion in Section 4.3.1. This behavior indicates a tilted initial director restricts crack opening compared to the parallel loading cases. The corresponding crack propagation rates during the steady growth phase are plotted in Figure 4.10f, with values of 0.0095 mm/s, 0.0028 mm/s, and 0.0008 mm/s at pre-stretching levels of 30%, 25%, and 20%, respectively. The simulation and experiment exhibit

a remarkable agreement in crack velocity at low pre-stretching levels, with only a slight deviation observed at high pre-stretching levels.

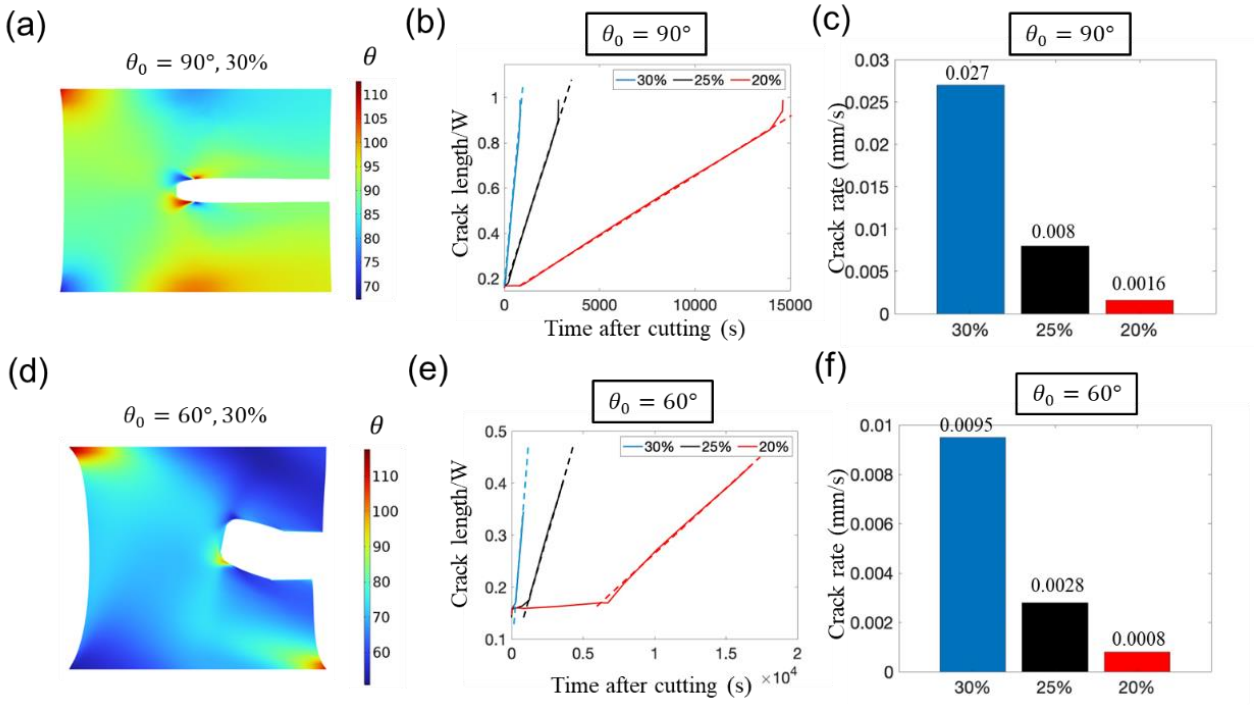

Figure 4.10 The crack prediction based on a phase-field model. The director distribution in a LCE with (a) $\theta_0 = 90°$ and (d) $\theta_0 = 60°$ at a pre-stretching level of 30%. The crack growth length in LCEs with (b) $\theta_0 = 90°$ and (e) $\theta_0 = 60°$ at pre-stretching level of 20%, 25%, and 30%. The corresponding constant crack growth rates in LCEs with (c) $\theta_0 = 90°$ and (f) $\theta_0 = 60°$.

Through a specialized surface density function in eqn (4.7), the crack is programmed to propagate perpendicular to the director ahead of the crack tip. Figure 4.11 presents a comparison of crack propagation paths in the undeformed configuration between phase-field simulations and experimental results for LCEs with initial directors $\theta_0 = 90°$ and $\theta_0 = 60°$. The contour illustrates the phase-field variable, where $\varphi = 0.99$ denotes a fully damaged material. The simulated crack paths closely match the experimental results, exhibiting a horizontal crack

propagation for $\theta_0 = 90°$ and an inclined crack path for $\theta_0 = 60°$. Note that we a portion of the crack path is simulated for $\theta_0 = 60°$, as damgae is not permitted at the boundary.

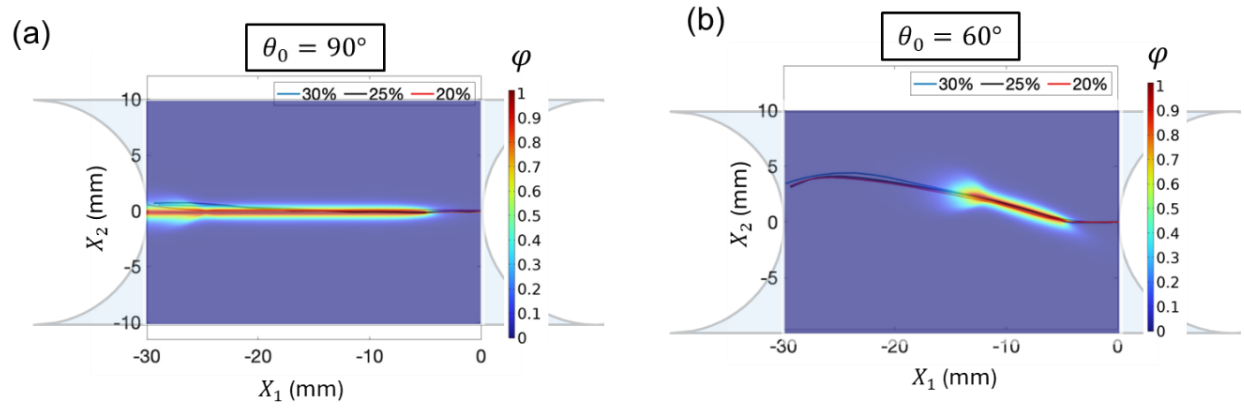

Figure 4.11 The crack propagation path comparison in the reference configuration between phase-field prediction and experiments for LCEs with an initial director (a) $\theta_0 = 90°$ and (b) $\theta_0 = 60°$

Although this phase-field model generally exhibits good agreement with experimental observations, it does present certain limitations. First, the predicted crack velocity at higher stretching levels, such as 30%, shows higher values than the experimental results. This discrepancy may be attributed to the model's failure to account for viscous director rotation. Given that the crack is constrained to propagate perpendicular to the director in the simulation, the strain rates along the crack propagation direction can be expressed as

$$\dot{\varepsilon_c} = \dot{\varepsilon_{11}} sin^2(\theta) + \dot{\varepsilon_{22}} cos^2(\theta) - 2\dot{\varepsilon_{12}} sin(\theta) cos(\theta), \quad (4.18)$$

where $\dot{\varepsilon_{11}}$, $\dot{\varepsilon_{13}}$, and $\dot{\varepsilon_{22}}$ are the components of strain rate tensor $\dot{\boldsymbol{\varepsilon}}$. Figure 4.12 presents the strain rates $\dot{\varepsilon_c}$ along the crack propagation direction in phase-field models. At low pre-stretching levels, where $\dot{\varepsilon_c}$ around the crack tip is smaller or approaching 0.1%/s (Figure 4.12a,d,e), the director rotation almost reaches equilibrium [62], resulting in close agreement between simulation and experimental results. However, at high pre-stretching levels, where $\dot{\varepsilon_c}$ near the crack tip

significantly exceeds 0.1%/s (Figure 4.12b,c,f), the deformation rates become sufficiently high for viscous director rotation to have a notable impact. Since this effect is not incorporated into the current model, discrepancies arise between the numerical predictions and experimental results. To improve model accuracy, incorporating viscous director rotation into both the constitutive material model and the viscous fracture is likely necessary. Besides, employing a more refined viscoelastic model, such as the multi-branch Maxwell model in Yu et al.[127] and Rezaei et al.[128], along with optimized material parameters, could enhance the model's precision.

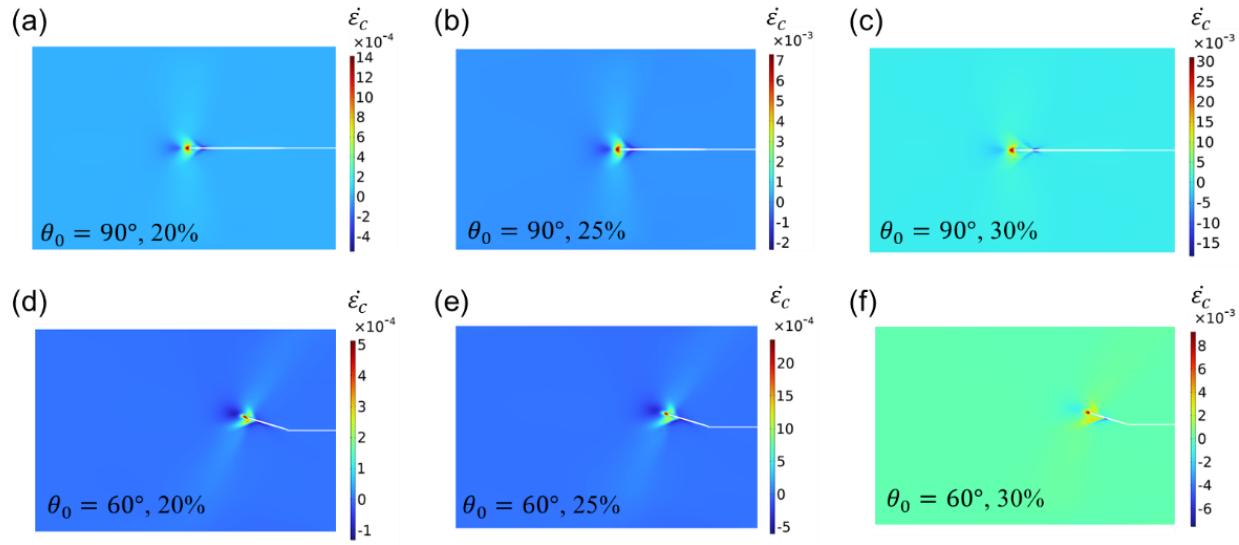

Figure 4.12 Strain rates along crack propagation direction in phase-field model with initial directors (a-c) $\theta_0 = 90°$ and (d-f) $\theta_0 = 60°$ under pre-prestretcing levels of (a,d) 20%, (b,e) 25%, and (c,f) 30%.

Secondly, the relationship between intrinsic fracture energy and director orientation remains uncertain, particularly considering the differing fracture energies of monodomain LCEs under perpendicular and parallel loading [54,61]. This complexity is most evident in the case of $\theta_0 = 30°$, where the intricate material composition at the crack tip poses a challenge. As a result,

the current phase-field model encounters convergence issues when simulating this case. Understanding and addressing these issues is crucial to refining the model and fully realizing its potential in accurately capturing the crack propagation behavior of LCEs.

Thirdly, the parameters used in the phase-field model are hard to measure experimentally. The value listed in Table 4.1 and 4 were mathematically fitted based on the experimental observations, i.e. crack velocity. However, these parameters possess physical significance, they should ideally be determined through direct experimental measurements rather than fitting procedures. Consequently, although the phase-field model's predictions align relatively well with post-cut test results, its applicability to other loading conditions may be limited or entirely inaccurate. To address this limitation, it is essential to design novel experimental methodologies to directly measure key material parameters, such as intrinsic fracture energy and phase-field length scale, thereby enhancing the model's robustness and generalizability.

4.5 Conclusion

In this chapter, we examine the crack propagation in LCEs under varying initial directors and pre-stretching levels. Given the crack propagation path is not always horizontal, conventional fracture evaluation using the 'pure shear' method is inadequate. Instead, we adopt a post-cut method by applying different pre-stretching levels to analyze the crack growth direction and rates while minimizing the effects of bulk dissipation. The director-dependent crack growth path is characterized through optical polarized measurement, and the steady-state crack growth rates are quantified. A phase-field model is implemented into COMSOL, yielding predictions that align well with experimental observations. This investigation highlights the significant

influence of initial directors and pre-stretching levels on crack propagation direction and rates, offering new insights into the mechanics of fracture in LCEs.

First, we find the crack typically propagates perpendicular to the director ahead of the crack. Under parallel loading ($\theta_0 = 90°$), the crack follows the $X_1 - axis$, with the director ahead of the crack tip aligns with $X_2 - axis$. Under tilted loading ($\theta_0 \neq 90°$), the crack path deviates from $X_1 - axis$, maintain a direction perpendicular to the tilted director ahead of the crack tip. In addition, at $\theta_0 = 30°$, the crack path becomes more horizontal as pre-stretching levels increase due to the director's rotation towards $X_2 - axis$, whereas other loading angles show minimal dependence on pre-stretching. Notably, an atypical crack growth is observed at a 30% pre-stretching level in a LCE with $\theta_0 = 30°$, where strip domains and monodomain coexist at the crack tip after cutting. The crack initiates in the strip domain and later reorients perpendicularly to the director. This anomalous behavior is believed attributed to the lower fracture energy in the strip domain compared to the monodomain.

Secondly, the crack propagation rates exhibit an initial delay in growth followed by a steady-state velocity. Even in LCEs with $\theta_0 = 90°$, an obvious crack growth delay is observed at the onset. This phenomenon is assumed to be attributed to the combined effects of the long-time relaxation of LCEs, viscous toughness, and crack nucleation as previously reported [119–121]. In LCEs with tilted initial directors, the delay in crack growth is more pronounced during the early stages, suggesting that inhomogeneous and significant director reorientation impedes crack opening. Overall, the crack growth rate increases with higher pre-stretching levels, potentially following a power-law relationship.

Finally, we use a phase-field model to demonstrate the mechanism. By prescribing the crack direction perpendicular to the director, the model successfully reproduces both the crack propagation direction and rates observed in experiments. However, at higher pre-stretching levels, the model predicts faster crack rates than those observed experimentally. This discrepancy is likely due to the failure to account for viscous director rotation. To address this limitation, it is recommended to consider a more decent viscoelastic constitutive model and viscous toughness.

This work is the first to systematically investigate the crack propagation direction and rates in relation to varying initial directors and stretching levels. The findings offer thoughtful insights into fracture behavior and provide valuable contributions to the development of fracture criteria. However, several questions remain unsolved. The fracture mechanical differences between strip domains and monodomains are not yet fully understood, complicating the prediction of crack direction when both domains exist. Besides, the current model is unable to simulate strip domains; an alternative free energy formulation proposed by Desimone et al.[129] may be considered for future work. Furthermore, the rate predictions from simulations show some divergence from experimental results, indicating a need for further refinement of the phase-field models. Lastly, it is essential to develop a more advanced methodology to experimentally measure material properties required for the phase-field model. We anticipate that with these improvements, a comprehensive fracture criteria for LCEs could be established.

Chapter 5 Conclusions and Outlook

5.1 Conclusions

This dissertation provides a comprehensive exploration of rate-dependent mechanical responses, stress-director coupling effects around the crack tip, and dynamic crack propagation in LCEs with varying initial directors and loading conditions. The experimental methodologies and theoretical constitutive models developed in this work not only enhance our understanding of LCEs mechanism but also provide a foundation for broader application, serving as a valuable resource for further research. These findings hold significant potential for guiding the design of optimized LCEs. The key contributions are summarized as follows:

In Chapter 2, we investigate the rate-dependent stress, strain, and director rotation under tension at different loading rates. We systematically characterize real-time stress, strain, and director orientation in experiments, highlighting both viscous networks and mesogens. Notable, we quantitively differentiate the two distinct relaxation time scales associated with network deformation and director rotation. To further explain the rate-dependent behavior, a viscoelastic constitutive model is developed, presenting analytical solutions that qualitatively match experimental results. This study provides a detailed analysis of the complex interaction between network extension and director rotation, advancing our understanding of the stress-director coupling effect and its influence on the viscoelastic response of LCEs.

In Chapter 3, we examine the stress-director coupling effect on a crack tip. A complex LCEs model is implemented into ABAQUS UEL. Through the experiments and simulations, we observe symmetrical stress, strain director distributions when the initial director is aligned parallel to the loading direction. In contrast, when the initial director is tilted relative to the

loading direction, the stress, strain, and director distributions around the crack tip become asymmetrical. Notably, a formation of the domain wall is observed in both experiments and simulations under tilted loading. The fracture behavior is evaluated through energy release rate and crack opening displacement, revealing that a tilted initial director inhibits the crack opening. This work provides a valuable understanding of the director, stress, and strain distributions in the vicinity of a crack tip of LCEs. The findings and methodology presented here provide a solid foundation for further investigation into the fracture behavior.

In Chapter 4, we present a detailed discussion on crack propagation influenced by varying initial directors and pre-stretching levels. Our systematic investigation reveals that the crack typically propagates perpendicular to the director ahead of the crack tip. However, an atypical crack growth path is observed when a strip domain exists at the crack tip. Additionally, the crack growth rates computed at steady stages increase with higher pre-stretching levels. A delay in the onset of crack growth is noted and becomes more pronounced at low pre-stretching levels and when there is a large deviation angle between the initial director and the loading direction. We implement a phase-field model in COMSOL, showing simulation results agree well with experimental observations. This study provides novel insights into crack propagation under varying initial directors, a topic previously unexplored, and offers new perspectives for the development of fracture criteria of LCEs.

5.2 Outlook

In this dissertation, we have studied the unique mechanical response of LCEs under various loading conditions, showing lots of interesting phenomena driven by stress-director

coupling effects. However, there are still many questions remaining unanswered. I outline several areas for further study.

First, the viscoelastic constitutive model requires further refinement. While we excluded the viscosity of the director due to its relatively negligible short relaxation time scale, this assumption may not hold near the crack tip, where the strain rates are extremely high due to the strain concentration. In such a case, the director's viscosity must be accounted. Moreover, most existing viscoelastic models are based on monodomain LCEs. Our study on fracture highlights the demand for an advanced model capable of capturing the transition between the monodomain and strip domains.

Secondly, optimizing the design of LCEs through the tuning of initial directors is a promising area of research. Strategically orienting the directors to mitigate stress and strain concentration at critical locations, such as crack tips, could prevent failure. However, identifying optimal designs remains a challenge. With advancements in artificial intelligence, there is potential to leverage AI to explore various combinations of initial director arrangements and identify the most effective configurations. Such design guidance could significantly expand the application potential of LCEs.

Thirdly, defining the failure criteria or fracture energy in LCEs presents significant challenges due to the dependency of fracture energy on director orientation. It is crucial to understand how fracture energy is influenced by director orientation and the mechanism underlying chain breakage within strip domains. For LCEs with tilted initial directors, accurately measuring fracture energy is particularly challenging because the oblique crack propagation path subjects the material to mixed-mode tension. Furthermore, the inherent high viscosity of LCEs

complicates the assessment of rate-dependent fracture energy. Last, it is hard to introduce a uniform crack across experiments and crack sharpness will also influence the crack propagation, especially at the onset of crack growth. There is currently no established failure criterion for standard viscoelastic soft material. Addressing these complexities remains a critical avenue for further research.

Appendix

A.1 Viscoelastic Constitutive Model

To simulate the crack-tip fields of LCEs, we implement the constitutive model into a FEM code. Though we assume the LCE samples are loaded slowly enough to reach quasi-equilibrium so that we do not need to consider their viscoelasticity, a small dissipation is added to the model to avoid convergence issues during analyses. Following Zhang et al. [72], we use a simple Rayleigh dissipation density function to represent the viscosity of the network and the director

$$R = R\left(\dot{\boldsymbol{\varepsilon}}, \widetilde{\dot{\boldsymbol{d}}}\right) = \frac{1}{2}\eta_d \widetilde{\dot{\boldsymbol{d}}}^2 + \frac{1}{2}\eta_0 tr(\dot{\boldsymbol{\varepsilon}}^2), \tag{A1}$$

where $\dot{\boldsymbol{\varepsilon}}$ is the strain rate tensor $\dot{\boldsymbol{\varepsilon}} = \dot{\boldsymbol{F}}\boldsymbol{F}^{-1}$, $\widetilde{\dot{\boldsymbol{d}}}$ is the corotational time derivative $\widetilde{\dot{\boldsymbol{d}}} = \dot{\boldsymbol{d}} - \boldsymbol{W}\boldsymbol{d}$ with $\boldsymbol{W}$ the spin tensor $\boldsymbol{W} = (\nabla\dot{\boldsymbol{u}} - \nabla\dot{\boldsymbol{u}}^T)/2$, and η_0 and η_d are the viscosity of the network extension and director rotation, respectively, which are assumed very small, $\eta_0/\mu = \eta_d/\mu = 10^{-4}s$. In our simulations, we applied a low loading rate to ensure the quasistatic condition. The energy balance can be expressed as

$$\dot{W} - \int_{\Omega_0} \dot{f}_r dV = \int_{\Omega_0} \left(\frac{\partial R}{\partial \widetilde{\dot{\boldsymbol{d}}}} : \widetilde{\dot{\boldsymbol{d}}} + \frac{\partial R}{\partial \dot{\boldsymbol{\varepsilon}}} : \dot{\boldsymbol{\varepsilon}}\right) dV, \tag{A2}$$

where $\dot{W}$ is the external power and f_r is the free energy density, as elaborated in the main text.

Due to the addition of the Rayleigh dissipation, we could re-derive the governing equations associated with $\ddot{\boldsymbol{u}}$ and $\dot{\boldsymbol{d}}$ as the following, which are slightly different from Eqs. (3.6)-(3.8)

$$div(\boldsymbol{\sigma}) + \boldsymbol{b} = \boldsymbol{0}, \tag{A3}$$

$$\eta_d \dot{\boldsymbol{d}} \times \boldsymbol{d} = \eta_d \boldsymbol{W}\boldsymbol{d} \times \boldsymbol{d} - \mu\left(\left(l_{\parallel}^{-1} - l_{\perp}^{-1}\right)\boldsymbol{F}\boldsymbol{l_0}\boldsymbol{F}^T\boldsymbol{d} + \alpha\boldsymbol{F}(\boldsymbol{I} - \boldsymbol{d_0} \otimes \boldsymbol{d_0})\boldsymbol{F}^T\boldsymbol{d}\right) \times \boldsymbol{d} + K\nabla^{\boldsymbol{2}}\boldsymbol{d} \times \boldsymbol{d}, \tag{A4}$$

where the Cauchy stress $\boldsymbol{\sigma}$ is

$$\boldsymbol{\sigma} = J^{-1}\mu\left(\boldsymbol{l}^{-1}\boldsymbol{F}\boldsymbol{l_0}\boldsymbol{F}^{\boldsymbol{T}} + \alpha\boldsymbol{d} \otimes (\boldsymbol{I} - \boldsymbol{d_0} \otimes \boldsymbol{d_0})\boldsymbol{F}^{\boldsymbol{T}}\boldsymbol{d} \cdot \boldsymbol{F}^{\boldsymbol{T}} - \boldsymbol{I}\right) + 2B(J-1)\boldsymbol{I} - J^{-1}K(\nabla\boldsymbol{d})^T\nabla\boldsymbol{d} + J^{-1}\eta_0\dot{\boldsymbol{\varepsilon}} + \frac{J^{-1}}{2}\eta_d(\boldsymbol{d} \otimes \left(\dot{\boldsymbol{d}} - \boldsymbol{W}\boldsymbol{d}\right) - (\dot{\boldsymbol{d}} - \boldsymbol{W}\boldsymbol{d}) \otimes \boldsymbol{d}). \tag{A5}$$

If the viscosity is not considered, Eqs. (A4)(A5) recover Eqs. (3.7)(3.8) by eliminating the terms involving η_0 and η_d. The first two terms in Eq. (A5) can be rewritten as the following so that the first term is independent of the director, which is more convenient for the implementation of the UEL later

$$\boldsymbol{\sigma} = J^{-1}\mu\left(l_{\perp}^{-1}\boldsymbol{F}\boldsymbol{l_0}\boldsymbol{F}^T + \left(l_{\parallel}^{-1} - l_{\perp}^{-1}\right)\boldsymbol{d} \otimes \boldsymbol{F}\widehat{\boldsymbol{l_0}}\boldsymbol{F}^T\boldsymbol{d} - \boldsymbol{I}\right) + 2B(J-1)\boldsymbol{I} - J^{-1}K(\nabla\boldsymbol{d})^T\nabla\boldsymbol{d} + J^{-1}\eta_0\dot{\boldsymbol{\varepsilon}} + \frac{J^{-1}}{2}\eta_d(\boldsymbol{d} \otimes \left(\dot{\boldsymbol{d}} - \boldsymbol{W}\boldsymbol{d}\right) - (\dot{\boldsymbol{d}} - \boldsymbol{W}\boldsymbol{d}) \otimes \boldsymbol{d}), \tag{A6}$$

with $\widehat{\boldsymbol{l_0}} = \boldsymbol{l_0} + \alpha(\boldsymbol{I} - \boldsymbol{d_0} \otimes \boldsymbol{d_0})/\left(l_{\parallel}^{-1} - l_{\perp}^{-1}\right)$. Under the plane strain condition, the director degenerates to $\boldsymbol{d} = (\cos(\theta), \sin(\theta), 0)$, where θ is utilized as the variable to represent the angle between the director and the $X_1 -$ axis. Thereby, the governing equation Eq. (A4) can be further simplified as

$$\eta_d\dot{\theta} + \eta_d W_{12} - \sigma^d{}_{21} + \sigma^d{}_{12} - K\nabla^2\theta = 0, \tag{A7}$$

with $\boldsymbol{\sigma^d} = \mu(l_{\parallel}^{-1} - l_{\perp}^{-1})\boldsymbol{d} \otimes \boldsymbol{F}\widehat{\boldsymbol{l_0}}\boldsymbol{F}^T\boldsymbol{d}$. The boundary conditions associated with the displacement and the director field are

$$\boldsymbol{\sigma} \cdot \boldsymbol{n} = \boldsymbol{t}, \tag{A8}$$

$$J^{-1}K\boldsymbol{\nabla}\boldsymbol{d} \cdot \boldsymbol{n} = \boldsymbol{0}, \tag{A9}$$

where $\boldsymbol{t}$ is the traction in the current configuration on the surface, and $\boldsymbol{n}$ represents the unit outer vector normal to the deformed surface boundary. In this study, we assume no body force and surface traction.

A.2 Numerical Solution Procedure

Based on the FEM, the two coupled Eqs. (A3) (A4) are solved via a Newton procedure by gradually vanishing the corresponding residuals on the element level. We use a method similar to Chester et al.[95] to implement the coupled equations into a user element subroutine, UEL, in the commercial finite element software, ABAQUS. The trial solutions for the displacement and the director angle are interpolated inside each element by:

$$\boldsymbol{u} = \sum \boldsymbol{u^A} N^A, \tag{A10}$$

$$\theta = \sum \theta^A N^A, \tag{A11}$$

where A={1,2,3 …} denotes the nodes of a given element, $\boldsymbol{u^A}$ and θ^A represent the values of the displacement and the director angle at node A, and N^A represents the corresponding shape function. In the absence of body forces, we employ a standard Galerkin approach with two weight functions $\boldsymbol{w_1} = \sum \boldsymbol{w_1}^A N^A$ and $w_2 = \sum {w_2}^A N^A$, where $\boldsymbol{w_1}$ and w_2 have the same shape function as the trial solutions and vanish under the Dirichlet boundary condition. In the absence of body forces, we can get two weak forms for Eqs. (A3) (A4)

$$\int_{\Omega_c} \boldsymbol{w_1} \cdot div(\boldsymbol{\sigma}) dv = 0, \tag{A12}$$

$$\int_{\Omega_c} w_2 \left(\eta_d \dot{\theta} + \eta_d W_{12} - {\sigma^d}_{21} + {\sigma^d}_{12} - K\nabla^2\theta\right) dv = 0\,. \tag{A13}$$

Through the divergence theorem and boundary conditions in Eqs. (A8) (A9), we can get the following element-level equations

$$\int_{\Omega_c} \frac{\partial N^A}{\partial x} \boldsymbol{\sigma} dv = \int_{\Gamma_c} N^A \boldsymbol{t} da, \tag{A14}$$

$$\int_{\Omega_c} N^A \left(\eta_d \dot{\theta} + \eta_d W_{12} - {\sigma^d}_{21} + {\sigma^d}_{12}\right) dv = -\int_{\Omega_c} K \frac{\partial N^A}{\partial x} \nabla\theta dv. \tag{A15}$$

We solve the coupled equations through the Newton's method by defining two residuals $\boldsymbol{R_u^A}$ and R_θ^A for the displacement and the director

$$\boldsymbol{R_u^A} = -\int_{\Omega_c} \frac{\partial N^A}{\partial x} \boldsymbol{\sigma} dv + \int_{\Gamma_c} N^A \boldsymbol{t} da, \tag{A16}$$

$$R_\theta^A = -\int_{\Omega_c} (N^A \left(\eta_d \dot{\theta} + \eta_d W_{12} - {\sigma^d}_{21} + {\sigma^d}_{12}\right) + K \frac{\partial N^A}{\partial x} \nabla\theta) dv. \tag{A17}$$

In addition to the residuals, ABAQUS/Standard requires the matrix AMATRX to be evaluated and updated for the iterative Newton solver. AMATRX is defined as an array containing the contribution of this element to the Jacobian (stiffness) or other matrix of the overall system of equations, which is given by:

$$K = \begin{bmatrix} K_{u_1u_1}^{11} & K_{u_1u_2}^{11} & K_{u_1\theta}^{11} & & K_{u_1u_1}^{14} & K_{u_1u_2}^{14} & K_{u_1\theta}^{14} \\ K_{u_2u_1}^{11} & K_{u_2u_2}^{11} & K_{u_2\theta}^{11} & \cdots & K_{u_2u_1}^{14} & K_{u_2u_2}^{14} & K_{u_2\theta}^{14} \\ K_{\theta u_1}^{11} & K_{\theta u_2}^{11} & K_{\theta\theta}^{11} & & K_{\theta u_1}^{14} & K_{\theta u_2}^{14} & K_{\theta\theta}^{14} \\ & \vdots & & \ddots & & \vdots & \\ K_{u_1u_1}^{41} & K_{u_1u_2}^{41} & K_{u_1\theta}^{41} & & K_{u_1u_1}^{44} & K_{u_1u_2}^{44} & K_{u_1\theta}^{44} \\ K_{u_2u_1}^{41} & K_{u_2u_2}^{41} & K_{u_2\theta}^{41} & \cdots & K_{u_2u_1}^{44} & K_{u_2u_2}^{44} & K_{u_2\theta}^{44} \\ K_{\theta u_1}^{41} & K_{\theta u_2}^{41} & K_{\theta\theta}^{41} & & K_{\theta u_1}^{44} & K_{\theta u_2}^{44} & K_{\theta\theta}^{44} \end{bmatrix}, \tag{A18}$$

where the Jacobian stiffness $K_{u_iu_k}^{AB} = -\partial R_{u_i}^A / \partial u_k^B$, $K_{u_i\theta}^{AB} = -\partial R_{u_i}^A / \partial \theta^B$, $K_{\theta\theta}^{AB} = -\partial R_\theta^A / \partial \theta^B$, and $K_{\theta u_i}^{AB} = -\partial R_\theta^A / \partial u_i^B$ with B={1,2,3 …} denoting the nodes of the element, and u_1 and u_2 denote the displacements in the X_1 and X_2 directions, respectively. In this study, we utilize a 2D plane-strain 4-node linear quadrilateral elements, and hence AMATRX is a 12 by 12 matrix. Here we rewrite each Jacobian stiffness in the index notation

$$K_{u_i u_k}^{AB} = \frac{-\partial R_{u_i}^A}{\partial u_k^B} = \frac{\partial\left(\int_{\Omega_c} \frac{\partial N^A}{\partial x_j}\sigma_{ij} dv - \int_{\Gamma_c} N^A \boldsymbol{t} da\right)}{\partial u_k^B} = \int_{\Omega_c} \frac{\partial N^A}{\partial x_j}\left(J^{-1} F_{lN} F_{jM} \frac{\partial J[\boldsymbol{\sigma F}^{-T}]_{iM}}{\partial F_{kN}}\right)\frac{\partial N^B}{\partial x_l} dv - \int_{\Gamma_c} N^A N^B \frac{\partial \boldsymbol{t}}{\partial u_k} da, \tag{A19}$$

with $[\quad]_{ij}$ represents the matrix component. We assume there is no surface traction, and thereby the last term in Eq. (A19) can be eliminated. Substitute Eq. (A6), and $\partial J[\boldsymbol{\sigma F}^{-T}]_{iM}/\partial F_{kN}$ can be expressed as

$$\frac{\partial J(\boldsymbol{\sigma F}^{-T})_{iM}}{\partial F_{kN}} = K_{iM,kN}^1 + K_{iM,kN}^2 + K_{iM,kN}^3 - K_{iM,kN}^4 + K_{iM,kN}^5 + K_{iM,kN}^6, \tag{A20}$$

where

$$K_{iM,kN}^1 = \partial \eta_0 [\dot{\boldsymbol{\varepsilon}} \boldsymbol{F}^{-T}]_{iM}/\partial F_{kN}, \tag{A21}$$

$$K_{iM,kN}^2 = \partial \mu (l_\perp^{-1}[\boldsymbol{F l_0}]_{iM} - {F^{-1}}_{Mi})/\partial F_{kN}, \tag{A22}$$

$$K_{iM,kN}^3 = \partial \mu \left(l_\parallel^{-1} - l_\perp^{-1}\right)[\boldsymbol{Q F}^{-T}]_{iM}/\partial F_{kN}, \tag{A23}$$

$$K_{iM,kN}^4 = \partial K[(\nabla \boldsymbol{d})^T \nabla \boldsymbol{d} \cdot \boldsymbol{F}^{-T}]_{iM}/\partial F_{kN}, \tag{A24}$$

$$K_{iM,kN}^5 = \partial \eta_d [\boldsymbol{H F}^{-T}]_{iM}/2\partial F_{kN}, \tag{A25}$$

$$K_{iM,kN}^6 = \partial 2BJ(J-1){F^{-T}}_{Mi}/\partial F_{kN}, \tag{A26}$$

with tensor $\dot{\boldsymbol{\varepsilon}} = (\dot{\boldsymbol{F}}\boldsymbol{F}^{-1} + \boldsymbol{F}^{-T}\dot{\boldsymbol{F}}^T)/2$, $\boldsymbol{Q} = \boldsymbol{d} \otimes \boldsymbol{F}\widehat{\boldsymbol{l_0}}\boldsymbol{F^T}\boldsymbol{d}$, and $\boldsymbol{H} = \boldsymbol{d} \otimes \left(\dot{\boldsymbol{d}} - \boldsymbol{W d}\right) - (\dot{\boldsymbol{d}} - \boldsymbol{W d}) \otimes \boldsymbol{d}$. Therefore, $K_{iM,kN}^1$ to $K_{iM,kN}^6$ can be calculated as

$$K_{iM,kN}^1 = \frac{\eta_0}{2}\left(\frac{1}{\Delta t}[\boldsymbol{F}^{-1}\boldsymbol{F}^{-T}]_{NM}\delta_{ki} - [\dot{\boldsymbol{F}}\boldsymbol{F}^{-1}]_{ik}[\boldsymbol{F}^{-1}\boldsymbol{F}^{-T}]_{NM} + \frac{1}{\Delta t}F_{Mk}^{-1}F_{Ni}^{-1} - [\boldsymbol{F}^{-1}\dot{\boldsymbol{F}}\boldsymbol{F}^{-1}]_{Mk}F_{Ni}^{-1}\right) - \eta_0[\dot{\boldsymbol{\varepsilon}}\boldsymbol{F}^{-T}]_{iN}F_{Mk}^{-1}, \tag{A27}$$

$$K_{iM,kN}^2 = \mu l_\perp^{-1}\delta_{ki}{l_0}_{NM} + F_{Ni}^{-1}F_{Mk}^{-1}, \tag{A28}$$

$$K^3_{iM,kN} = \mu\left(l_{\parallel}^{-1} - l_{\perp}^{-1}\right)(D_{iN}F^{-1}_{Mk} + n_i[\boldsymbol{F^{-1}F}\widehat{\boldsymbol{l_0}}]_{MN}n_k - [\boldsymbol{QF^{-T}}]_{iN}F^{-1}_{Mk}), \tag{A29}$$

$$K^4_{iM,kN} = -K([(\nabla \boldsymbol{d})^T\nabla \boldsymbol{d}\cdot \boldsymbol{F}^{-T}]_{kM}F^{-1}_{Ni} - [(\nabla \boldsymbol{d})^T\nabla \boldsymbol{d}]_{ki}\left[\boldsymbol{F^{-1}F^{-T}}\right]_{MN} - [(\nabla \boldsymbol{d})^T\nabla \boldsymbol{d}\cdot \boldsymbol{F}^{-T}]_{iN}F^{-1}_{Mk}), \tag{A30}$$

$$K^5_{iM,kN} = \frac{\eta_d}{2}(-d_i\frac{\partial W_{ab}}{\partial F_{kN}}d_b + \frac{\partial W_{ib}}{\partial F_{kN}}d_bd_a)F^{-1}_{Ma} - \frac{\eta_d}{2}[\boldsymbol{HF^{-T}}]_{iN}F^{-1}_{Mk}, \tag{A31}$$

$$K^6_{iM,kN} = 2BJ((2J-1)F^{-1}_{Nk}F^{-1}_{Mi} - (J-1)F^{-1}_{Ni}F^{-1}_{Mk}), \tag{A32}$$

where tensor $\boldsymbol{D} = \boldsymbol{d}\otimes\widehat{\boldsymbol{l_0}}\boldsymbol{F^T}\boldsymbol{d}$, Δt represents the time increment at each step, $\dot{\boldsymbol{d}} = (\boldsymbol{d}_{n+1} - \boldsymbol{d}_n)/\Delta t$ with variable $\boldsymbol{d}_{n+1}$ and $\boldsymbol{d}_n$ the directors at increment steps $n+1$ and n, respectively, and δ_{ki} represents Kronecker delta. $\partial W_{ab}/\partial F_{kn}$ in Eq. (A31) is

$$\frac{\partial W_{ab}}{\partial F_{kN}} = \frac{1}{2}(-[\dot{\boldsymbol{F}}\boldsymbol{F}^{-1}]_{ak}F^{-1}_{Nb} + [\dot{\boldsymbol{F}}\boldsymbol{F}^{-1}]_{bk}F^{-1}_{Na}) + \frac{1}{2\Delta t}(\delta_{ak}F^{-1}_{Nb} - \delta_{bk}F^{-1}_{Na}). \tag{A33}$$

To alleviate the convergent issue, following Chester et al. [95], we assume $\partial(\nabla \boldsymbol{d})/\partial \boldsymbol{F} = 0$ in deriving Eq. (A24), and approximate Eq. (A30) as

$$K^4_{iM,kN} = -K[(\nabla \boldsymbol{d})^T\nabla \boldsymbol{d}\cdot \boldsymbol{F}^{-T}]_{iN}F^{-1}_{Mk}). \tag{A34}$$

Similarly, the Jacobian stiffness $K^{AB}_{u_i\theta}$ is

$$K^{AB}_{u_i\theta} = \int_{\Omega_c}\frac{\partial N^A}{\partial x_j}\left(K^1_{ij,\theta} - K^2_{ij,\theta} + K^3_{ij,\theta}\right)N^B dv \tag{A35}$$

where

$$K^1_{ij,\theta} = \partial\mu\left(l_{\parallel}^{-1} - l_{\perp}^{-1}\right)Q_{ij}/\partial\theta \tag{A36}$$

$$K^2_{ij,\theta} = \partial[K(\nabla \boldsymbol{d})^T\nabla \boldsymbol{d}]_{ij}/\partial\theta, \tag{A37}$$

$$K^3_{ij,\theta} = \partial\eta_d H_{ij}/2\partial\theta, \tag{A38}$$

They can be calculated as:

$$K_{ij,\theta}^{1} = \mu\left(l_{\parallel}^{-1} - l_{\perp}^{-1}\right)\left[\frac{\partial d_i}{\partial \theta}\left[\boldsymbol{F}\widehat{\boldsymbol{l}_0}\boldsymbol{F}^{\boldsymbol{T}}\boldsymbol{d}\right]_j + d_i\left[\boldsymbol{F}\widehat{\boldsymbol{l}_0}\boldsymbol{F}^{\boldsymbol{T}}\frac{\partial \boldsymbol{d}}{\partial \theta}\right]_{\boldsymbol{j}}\right], \tag{A39}$$

$$K_{ij,\theta}^{2} = K\left[\frac{\partial(\nabla \boldsymbol{d})^T}{\partial \theta}\nabla \mathbf{d} + (\nabla \boldsymbol{d})^T\frac{\partial \nabla \mathbf{d}}{\partial \theta}\right]_{ij}, \tag{A40}$$

$$K_{ij,\theta}^{3} = \frac{\eta_d}{2}(Z_{ij} - Z_{ji}), \tag{A41}$$

where tensor $\boldsymbol{Z} = \frac{\partial \boldsymbol{d}}{\partial \theta} \otimes \left(\dot{\boldsymbol{d}} - \boldsymbol{W}\boldsymbol{d}\right) + \boldsymbol{d} \otimes \left(\frac{\partial \dot{\boldsymbol{d}}}{\partial \theta} - \boldsymbol{W}\frac{\partial \boldsymbol{d}}{\partial \theta}\right)$, and $\partial \boldsymbol{d}/\partial\theta = (-\sin(\theta), \cos(\theta), 0)$.

The Jacobian stiffness $K_{\theta\theta}^{AB}$ is

$$K_{\theta\theta}^{AB} = \int_{\Omega_c}\left(N^A N^B\left(K_{\theta,\theta}^{1} + K_{\theta,\theta}^{3} - K_{\theta,\theta}^{4}\right) + \frac{\partial N^A}{\partial x}K_{\theta,\theta}^{2}\frac{\partial N^B}{\partial x}\right)dv \tag{A42}$$

where $K_{\theta,\theta}^{1}$, $K_{\theta,\theta}^{2}$, $K_{\theta,\theta}^{3}$ and $K_{\theta,\theta}^{4}$ are:

$$K_{\theta,\theta}^{1} = \frac{\eta_d \partial \dot{\theta}}{\partial \theta} = \frac{\eta_d}{\Delta t}, \tag{A43}$$

$$K_{\theta,\theta}^{2} = K, \tag{A44}$$

$$K_{\theta,\theta}^{3} = \mu(l_{\parallel}^{-1} - l_{\perp}^{-1})S_{21}, \tag{A45}$$

$$K_{\theta,\theta}^{4} = \mu(l_{\parallel}^{-1} - l_{\perp}^{-1})S_{12}, \tag{A46}$$

with tensor $\boldsymbol{S} = \frac{\partial \boldsymbol{d}}{\partial \theta} \otimes \boldsymbol{F}\widehat{\boldsymbol{l}_0}\boldsymbol{F}^{\boldsymbol{T}}\boldsymbol{d} + \boldsymbol{d} \otimes \boldsymbol{F}\widehat{\boldsymbol{l}_0}\boldsymbol{F}^{\boldsymbol{T}}\frac{\partial \boldsymbol{d}}{\partial \theta}$.

The Jacobian stiffness $K_{\theta u_k}^{AB}$ is

$$K_{\theta u_k}^{AB} = \int_{\Omega_c} N^A\left(-K_{\theta,kN}^{1} + K_{\theta,kN}^{2} + K_{\theta,kN}^{3}\right)\frac{\partial N^B}{\partial x_a}F_{aN}dv, \tag{A47}$$

where the components $K_{\theta,kN}^{1}$, $K_{\theta,kN}^{2}$ and $K_{\theta,kN}^{3}$ are

$$K_{\theta,kN}^{1} = \mu\left(l_{\parallel}^{-1} - l_{\perp}^{-1}\right)\left[d_2\delta_{1k}\left[\widehat{\boldsymbol{l}_0}\boldsymbol{F}^{\boldsymbol{T}}\boldsymbol{d}\right]_N + d_2\left[\boldsymbol{F}\widehat{\boldsymbol{l}_0}\right]_{1N}d_k\right], \tag{A48}$$

$$K_{\theta,kN}^{2} = \mu\left(l_{\parallel}^{-1} - l_{\perp}^{-1}\right)\left[d_1\delta_{2k}\left[\widehat{\boldsymbol{l}_0}\boldsymbol{F}^{\boldsymbol{T}}\boldsymbol{d}\right]_N + d_1\left[\boldsymbol{F}\widehat{\boldsymbol{l}_0}\right]_{2N}d_k\right], \tag{A49}$$

$$K^3_{\theta,kN} = \frac{\eta_d}{2}([\dot{\boldsymbol{F}}\boldsymbol{F}^{-1}]_{2k}F^{-1}_{N1} - [\dot{\boldsymbol{F}}\boldsymbol{F}^{-1}]_{1k}F^{-1}_{N2} + \frac{1}{\Delta t}(\delta_{1k}F^{-1}_{N2} - \delta_{2k}F^{-1}_{N1})), \tag{A50}$$

To accommodate nearly incompressible solids and mitigate volumetric locking behavior, we implemented the F-bar method [94,95,130]. Based on the concept of splitting the deformation gradient into a volumetric part and a distortional part, we have

$$\boldsymbol{F} = \boldsymbol{F}_{dis}\boldsymbol{F}_{vol}, \tag{A51}$$

where $\boldsymbol{F}_{dis} = J^{-1/3}\boldsymbol{F}$ and $\boldsymbol{F}_{vol} = J^{1/3}\boldsymbol{I}$. The modified deformation gradient F-bar, $\overline{\boldsymbol{F}}$, is defined as the multiplication of the distortional part of $\boldsymbol{F}$ and the cubic root of the determinant of the deformation gradient $\boldsymbol{F_c}$ at the centroid of each element

$$\overline{\boldsymbol{F}} = (\frac{\det(\boldsymbol{F_c})}{J})^{1/3}\boldsymbol{F}. \tag{A52}$$

It is clear that the distortional/volumetric split of $\overline{\boldsymbol{F}}$ is

$$\overline{\boldsymbol{F}} = \overline{\boldsymbol{F}}_{dis}\overline{\boldsymbol{F}}_{vol}, \tag{A53}$$

with $\overline{\boldsymbol{F}}_{dis} = \boldsymbol{F}_{dis}$ and $\overline{\boldsymbol{F}}_{vol} = (\boldsymbol{F_c})_{vol}$. Thereby, the volumetric part changes to that at the centroid of the element, meaning that all the integration points in one element share the same volumetric deformation. We replace $\boldsymbol{F}$ by $\overline{\boldsymbol{F}}$ in the Cauchy stress Eq. (A6) so that the Cauchy stress at each Gauss point is computed as $\boldsymbol{\sigma}(\overline{\boldsymbol{F}})$. To simplify the implementation and calculation of the UEL, we still use $\boldsymbol{F}$ in Eq. (A7), but only applied $\overline{\boldsymbol{F}}$ to the residual equation related to the displacement, Eq. (A16). As a consequence, only the stiffness component $K^{AB}_{u_iu_k}$ needs to be modified to [94,95]

$$\overline{K^{AB}_{u_iu_k}} = K^{AB}_{u_iu_k} + \int \frac{\partial N^A}{\partial x_j}\boldsymbol{q}(\left(\frac{\partial N^B}{\partial x_l}\right)_c - \frac{\partial N^B}{\partial x_l})\,dv, \tag{A54}$$

where $(\partial N^B/\partial x_l)_c$ is the gradient operator at the centroid of an element, and $\boldsymbol{q}$ is a fourth-order tensor defined by

$$\boldsymbol{q} = \frac{1}{2}\boldsymbol{A}\colon(\boldsymbol{I}\otimes\boldsymbol{I}) - \frac{1}{2}(\boldsymbol{\sigma}\otimes\boldsymbol{I}), \tag{A55}$$

with $A_{ijkl} = J^{-1}F_{lN}F_{jM}\frac{\partial J[\boldsymbol{\sigma F}^{-T}]_{iM}}{\partial F_{kN}}$ the spatial elasticity tensor.

A.3 Supplementary Figures

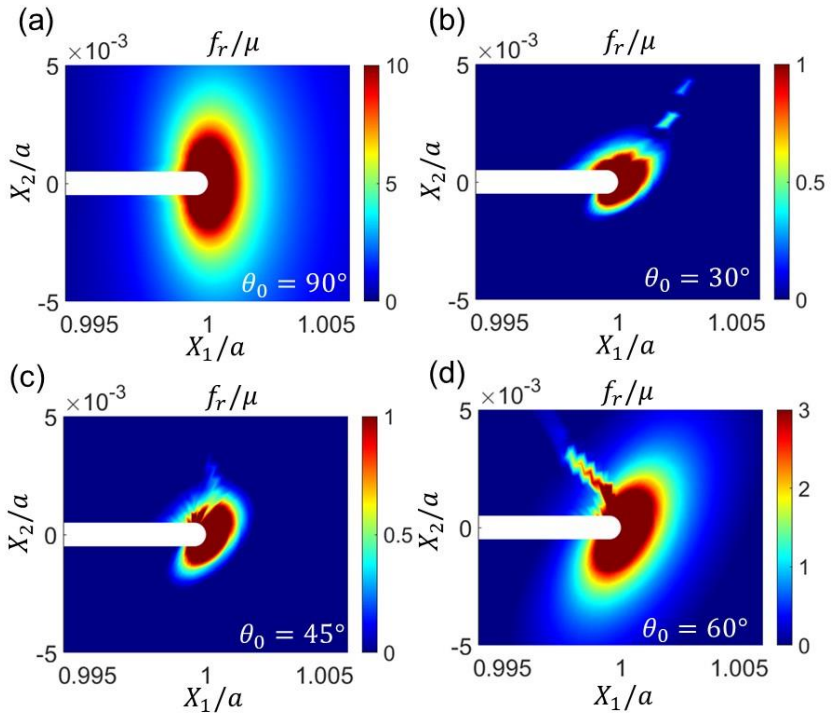

Fig. S1 FEM results of normalized elastic energy density distributions around the crack tip. Distributions of elastic free energy density around the crack tip at remote strain $\varepsilon^{\infty} = 10\%$ for LCEs with the initial director (a) $\theta_0 = 90°$, (b) $\theta_0 = 30°$, (c) $\theta_0 = 45°$, and (d) $\theta_0 = 60°$.

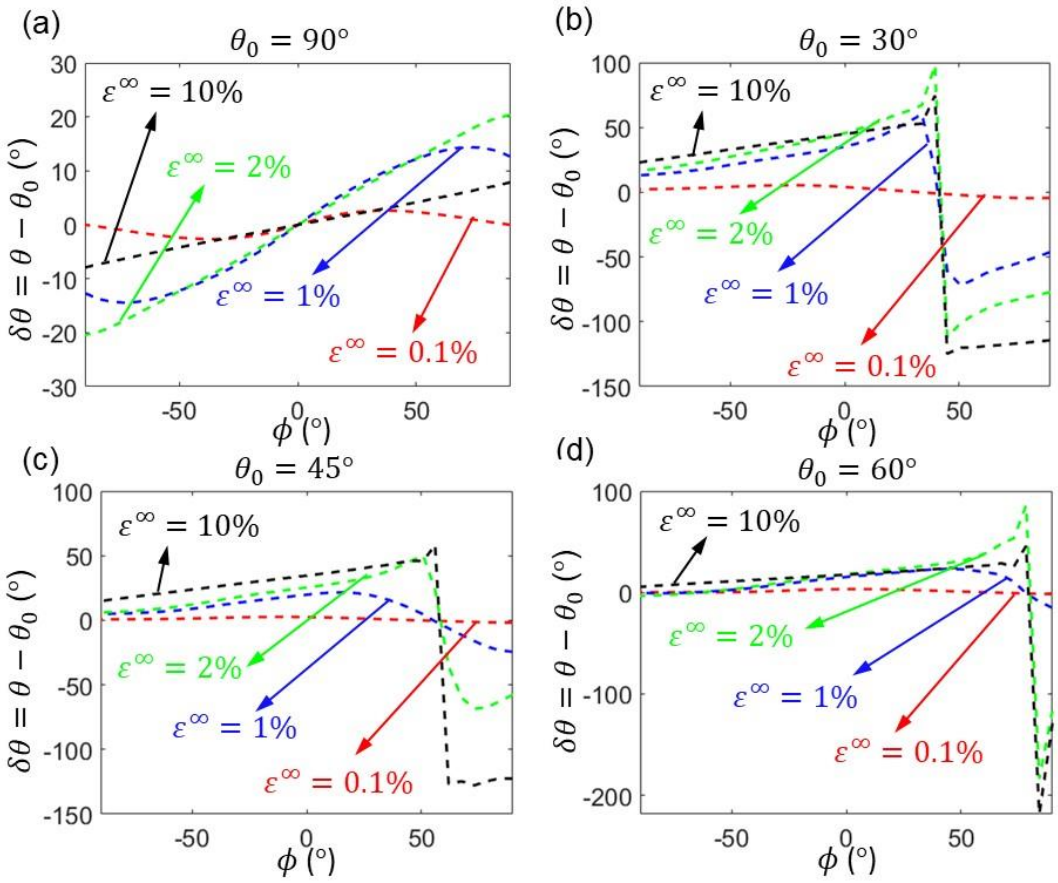

Fig. S2 FEM results of the director distributions at different ε^∞ around the crack tip. FEM simulation results of the director distributions at the crack tip at different remote strains from $\varepsilon^\infty = 0.1\%$ to 10% for LCEs with (a) $\theta_0 = 90°$, (b) 30°, (c) 45°, (d) 60°.

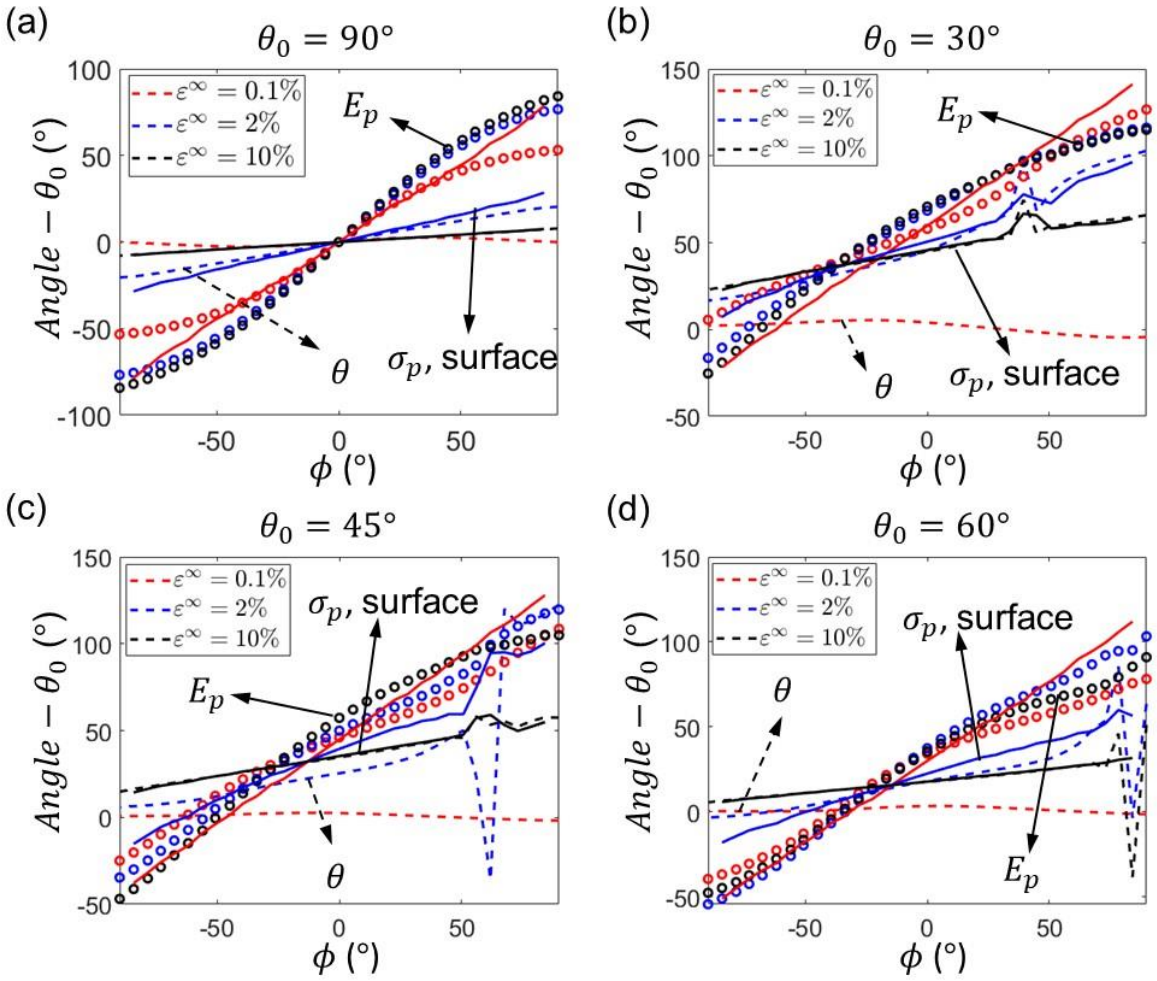

Fig. S3 FEM results of the relative angles at the crack tip at different ε^∞ around the crack tip for LCEs with (a) $\theta_0 = 90°$, (b) 30°, (c) 45°, and (d) 60°. The dots represent the direction of the maximum principal strain relative to the initial director; the solid curves represent the direction of the maximum principal stress and tangent direction of the crack surface relative to the initial director; the dashed curves represent the current director relative to the initial director. Note that for (b) $\theta_0 = 30°$, (c) 45° and (d) 60°, at $\varepsilon^\infty = 10\%$ and 2%, the clockwise director rotation at one side of the domain wall is added by 180° due to the symmetry of the director.

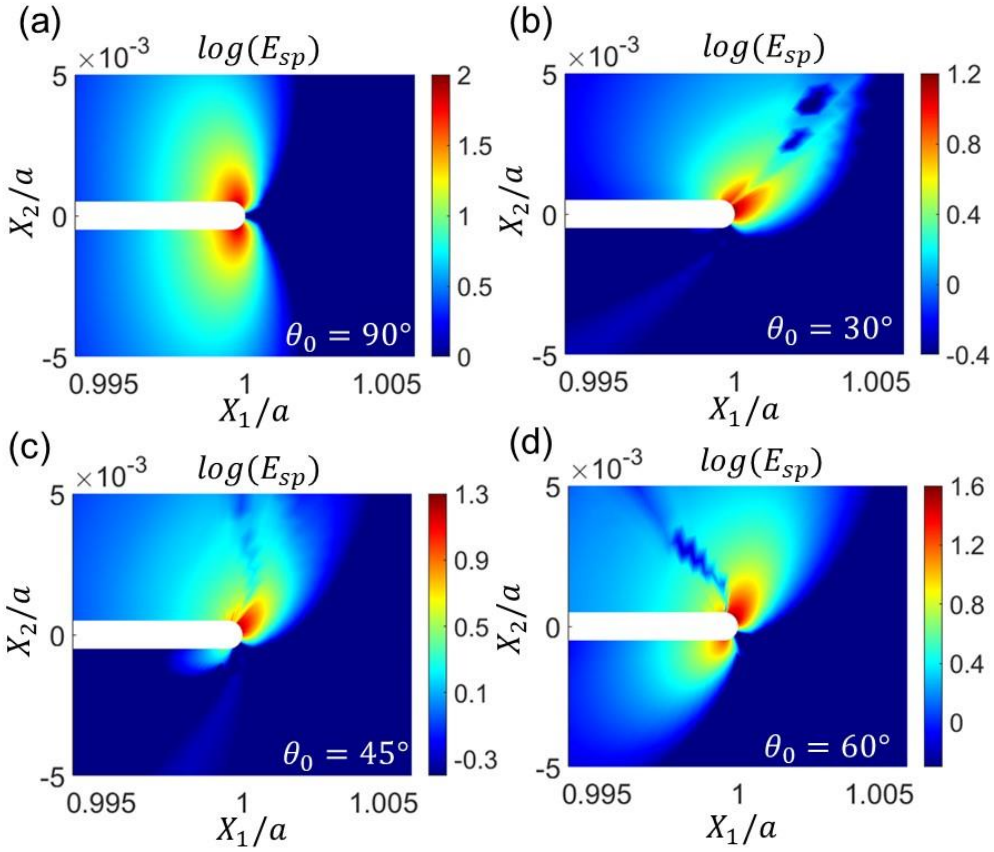

Fig. S4 FEM results of the spontaneous strain distributions around the crack tip. Distributions of the maximum principal spontaneous strain around the crack tip at remote strain $\varepsilon^{\infty} = 10\%$ for LCEs with the initial director (a) $\theta_0 = 90°$, (b) 30°, (c) 45°, and (d) 60°.

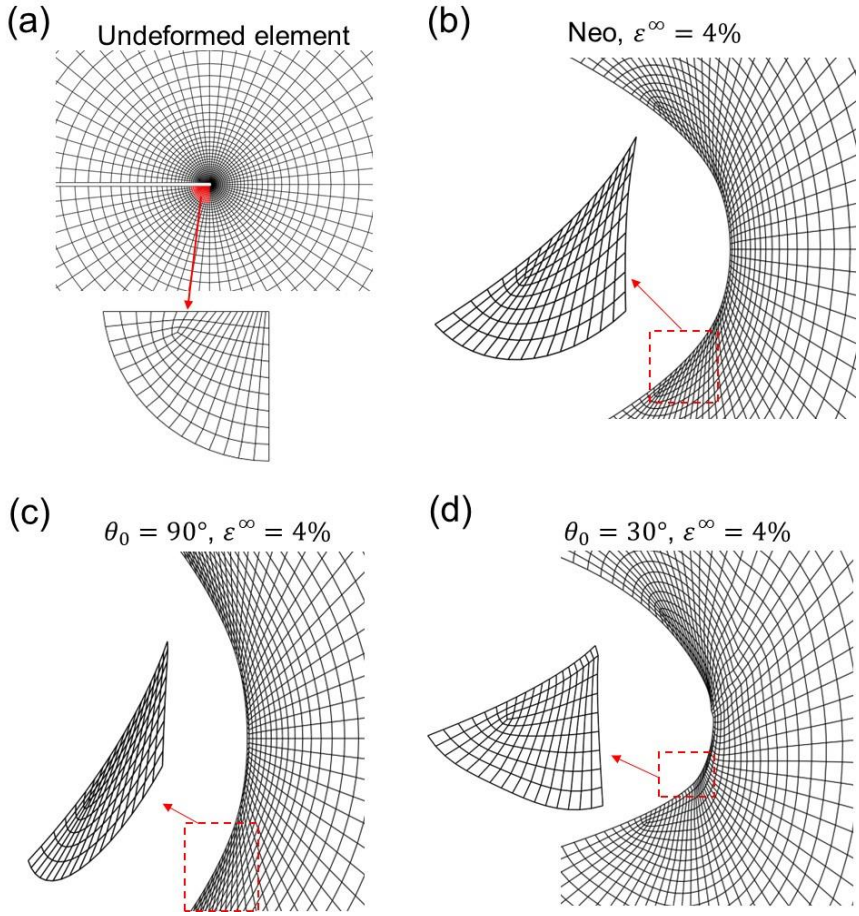

Fig. S5 Comparing the deformation of the FEM elements around the crack tip for LCEs and neo-Hookean materials at $\varepsilon^{\infty} = 4\%$. (a) Undeformed element. Crack opening and element deformation at $\varepsilon^{\infty} = 4\%$ for (b) a neo-Hookean material and a LCE with (c) $\theta_0 = 90°$ and (d) $\theta_0 = 30°$.

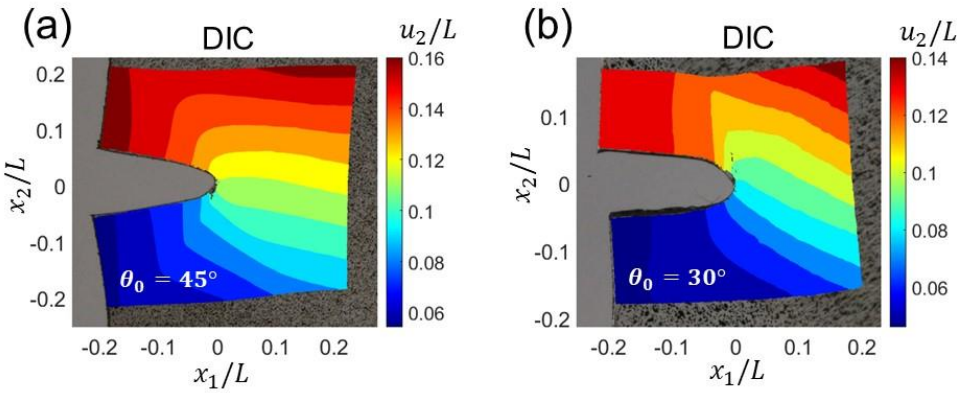

Fig. S6 DIC measurement of the displacement at $\varepsilon^{\infty} = 20\%$. Distributions of the normalized displacement u_2/L around the crack for the LCEs with (a) $\theta_0 = 45°$ and (b) $\theta_0 = 30°$.

Reference

[1] Yu, Y., and Ikeda, T., 2006, "Soft Actuators Based on Liquid-Crystalline Elastomers," Angew. Chem. Int. Ed., **45**(33), pp. 5416–5418. https://doi.org/10.1002/anie.200601760.

[2] Lee, K. M., Smith, M. L., Koerner, H., Tabiryan, N., Vaia, R. A., Bunning, T. J., and White, T. J., 2011, "Photodriven, Flexural–Torsional Oscillation of Glassy Azobenzene Liquid Crystal Polymer Networks," Advanced Functional Materials, **21**(15), pp. 2913–2918. https://doi.org/10.1002/adfm.201100333.

[3] White, T. J., Tabiryan, N. V., Serak, S. V., Hrozhyk, U. A., Tondiglia, V. P., Koerner, H., Vaia, R. A., and Bunning, T. J., 2008, "A High Frequency Photodriven Polymer Oscillator," Soft Matter, **4**(9), pp. 1796–1798. https://doi.org/10.1039/B805434G.

[4] Shaha, R. K., Merkel, D. R., Anderson, M. P., Devereaux, E. J., Patel, R. R., Torbati, A. H., Willett, N., Yakacki, C. M., and Frick, C. P., 2020, "Biocompatible Liquid-Crystal Elastomers Mimic the Intervertebral Disc," Journal of the Mechanical Behavior of Biomedical Materials, **107**, p. 103757. https://doi.org/10.1016/j.jmbbm.2020.103757.

[5] Gao, Y., Mori, T., Manning, S., Zhao, Y., Nielsen, A. D., Neshat, A., Sharma, A., Mahnen, C. J., Everson, H. R., Crotty, S., Clements, R. J., Malcuit, C., and Hegmann, E., 2016, "Biocompatible 3D Liquid Crystal Elastomer Cell Scaffolds and Foams with Primary and Secondary Porous Architecture," ACS Macro Lett., **5**(1), pp. 4–9. https://doi.org/10.1021/acsmacrolett.5b00729.

[6] Tian, H., Wang, Z., Chen, Y., Shao, J., Gao, T., and Cai, S., 2018, "Polydopamine-Coated Main-Chain Liquid Crystal Elastomer as Optically Driven Artificial Muscle," ACS Appl. Mater. Interfaces, **10**(9), pp. 8307–8316. https://doi.org/10.1021/acsami.8b00639.

[7] Wermter, H., and Finkelmann, H., 2001, "Liquid Crystalline Elastomers as Artificial Muscles," e-Polymers, **1**(1). https://doi.org/10.1515/epoly.2001.1.1.111.

[8] Ahn, C., Liang, X., and Cai, S., 2019, "Bioinspired Design of Light-Powered Crawling, Squeezing, and Jumping Untethered Soft Robot," Advanced Materials Technologies, **4**(7), p. 1900185. https://doi.org/10.1002/admt.201900185.

[9] White, T. J., and Broer, D. J., 2015, "Programmable and Adaptive Mechanics with Liquid Crystal Polymer Networks and Elastomers," Nature Mater, **14**(11), pp. 1087–1098. https://doi.org/10.1038/nmat4433.

[10] Rogóż, M., Zeng, H., Xuan, C., Wiersma, D. S., and Wasylczyk, P., 2016, "Light-Driven Soft Robot Mimics Caterpillar Locomotion in Natural Scale," Advanced Optical Materials, **4**(11), pp. 1689–1694. https://doi.org/10.1002/adom.201600503.

[11] Wu, S., Hong, Y., Zhao, Y., Yin, J., and Zhu, Y., 2023, "Caterpillar-Inspired Soft Crawling Robot with Distributed Programmable Thermal Actuation," Science Advances, **9**(12), p. eadf8014. https://doi.org/10.1126/sciadv.adf8014.

[12] Wang, C., Sim, K., Chen, J., Kim, H., Rao, Z., Li, Y., Chen, W., Song, J., Verduzco, R., and Yu, C., 2018, "Soft Ultrathin Electronics Innervated Adaptive Fully Soft Robots," Advanced Materials, **30**(13), p. 1706695. https://doi.org/10.1002/adma.201706695.

[13] Schätzle, J., Kaufhold, W., and Finkelmann, H., 1989, “Nematic Elastomers: The Influence of External Mechanical Stress on the Liquid-Crystalline Phase Behavior,” Die Makromolekulare Chemie, **190**(12), pp. 3269–3284. https://doi.org/10.1002/macp.1989.021901224.

[14] Naciri, J., Srinivasan, A., Jeon, H., Nikolov, N., Keller, P., and Ratna, B. R., 2003, “Nematic Elastomer Fiber Actuator,” Macromolecules, **36**(22), pp. 8499–8505. https://doi.org/10.1021/ma034921g.

[15] Sawa, Y., Urayama, K., Takigawa, T., DeSimone, A., and Teresi, L., 2010, “Thermally Driven Giant Bending of Liquid Crystal Elastomer Films with Hybrid Alignment,” Macromolecules, **43**(9), pp. 4362–4369. https://doi.org/10.1021/ma1003979.

[16] Finkelmann, H., Nishikawa, E., Pereira, G. G., and Warner, M., 2001, “A New Opto-Mechanical Effect in Solids,” Phys. Rev. Lett., **87**(1), p. 015501. https://doi.org/10.1103/PhysRevLett.87.015501.

[17] Yu, Y., Nakano, M., and Ikeda, T., 2003, “Directed Bending of a Polymer Film by Light,” Nature, **425**(6954), pp. 145–145. https://doi.org/10.1038/425145a.

[18] Winkler, M., Kaiser, A., Krause, S., Finkelmann, H., and Schmidt, A. M., 2010, “Liquid Crystal Elastomers with Magnetic Actuation,” Macromolecular Symposia, **291–292**(1), pp. 186–192. https://doi.org/10.1002/masy.201050522.

[19] Schuhladen, S., Preller, F., Rix, R., Petsch, S., Zentel, R., and Zappe, H., 2014, “Iris-Like Tunable Aperture Employing Liquid-Crystal Elastomers,” Advanced Materials, **26**(42), pp. 7247–7251. https://doi.org/10.1002/adma.201402878.

[20] Kaiser, A., Winkler, M., Krause, S., Finkelmann, H., and M. Schmidt, A., 2009, “Magnetoactive Liquid Crystal Elastomer Nanocomposites,” Journal of Materials Chemistry, **19**(4), pp. 538–543. https://doi.org/10.1039/B813120C.

[21] Courty, S., Miné, J., Tajbakhsh, A., and Terentjev, E., 2003, “Nematic Elastomers with Aligned Carbon Nanotubes: New Electromechanical Actuators,” EPL (Europhysics Letters), **64**. https://doi.org/10.1209/epl/i2003-00277-9.

[22] Fukunaga, A., Urayama, K., Takigawa, T., DeSimone, A., and Teresi, L., 2008, “Dynamics of Electro-Opto-Mechanical Effects in Swollen Nematic Elastomers,” Macromolecules, **41**(23), pp. 9389–9396. https://doi.org/10.1021/ma801639j.

[23] Lehmann, W., Skupin, H., Tolksdorf, C., Gebhard, E., Zentel, R., Krüger, P., Lösche, M., and Kremer, F., 2001, “Giant Lateral Electrostriction in Ferroelectric Liquid-Crystalline Elastomers,” Nature, **410**(6827), pp. 447–450. https://doi.org/10.1038/35068522.

[24] Warner, M., and Terentjev, E. M., 2007, *Liquid Crystal Elastomers*, OUP Oxford.

[25] Ericksen, J. L., 1991, “Liquid Crystals with Variable Degree of Orientation,” Arch. Rational Mech. Anal., **113**(2), pp. 97–120. https://doi.org/10.1007/BF00380413.

[26] Leslie, F. M., 1992, “Continuum Theory for Nematic Liquid Crystals,” Continuum Mech. Thermodyn, **4**(3), pp. 167–175. https://doi.org/10.1007/BF01130288.

[27] Stephen, M. J., and Straley, J. P., 1974, “Physics of Liquid Crystals,” Rev. Mod. Phys., **46**(4), pp. 617–704. https://doi.org/10.1103/RevModPhys.46.617.

[28] Urayama, K., Mashita, R., Kobayashi, I., and Takigawa, T., 2007, "Stretching-Induced Director Rotation in Thin Films of Liquid Crystal Elastomers with Homeotropic Alignment," Macromolecules, **40**(21), pp. 7665–7670. https://doi.org/10.1021/ma071104y.

[29] Okamoto, S., Sakurai, S., and Urayama, K., 2021, "Effect of Stretching Angle on the Stress Plateau Behavior of Main-Chain Liquid Crystal Elastomers," Soft Matter, **17**(11), pp. 3128–3136. https://doi.org/10.1039/D0SM02244F.

[30] He, X., Zheng, Y., He, Q., and Cai, S., 2020, "Uniaxial Tension of a Nematic Elastomer with Inclined Mesogens," Extreme Mechanics Letters, **40**, p. 100936. https://doi.org/10.1016/j.eml.2020.100936.

[31] Mistry, D., B. Morgan, P., H. Clamp, J., and F. Gleeson, H., 2018, "New Insights into the Nature of Semi-Soft Elasticity and 'Mechanical-Fréedericksz Transitions' in Liquid Crystal Elastomers," Soft Matter, **14**(8), pp. 1301–1310. https://doi.org/10.1039/C7SM02107K.

[32] Luo, C., Chung, C., Yakacki, C. M., Long, K., and Yu, K., 2022, "Real-Time Alignment and Reorientation of Polymer Chains in Liquid Crystal Elastomers," ACS Appl. Mater. Interfaces, **14**(1), pp. 1961–1972. https://doi.org/10.1021/acsami.1c20082.

[33] Küupfer, J., and Finkelmann, H., 1994, "Liquid Crystal Elastomers: Influence of the Orientational Distribution of the Crosslinks on the Phase Behaviour and Reorientation Processes," Macromolecular Chemistry and Physics, **195**(4), pp. 1353–1367. https://doi.org/10.1002/macp.1994.021950419.

[34] Higaki, H., Takigawa, T., and Urayama, K., 2013, "Nonuniform and Uniform Deformations of Stretched Nematic Elastomers," Macromolecules, **46**(13), pp. 5223–5231. https://doi.org/10.1021/ma400771z.

[35] Mistry, D., Traugutt, N. A., Sanborn, B., Volpe, R. H., Chatham, L. S., Zhou, R., Song, B., Yu, K., Long, K. N., and Yakacki, C. M., 2021, "Soft Elasticity Optimises Dissipation in 3D-Printed Liquid Crystal Elastomers," Nat Commun, **12**(1), p. 6677. https://doi.org/10.1038/s41467-021-27013-0.

[36] Azoug, A., Vasconcellos, V., Dooling, J., Saed, M., Yakacki, C. M., and Nguyen, T. D., 2016, "Viscoelasticity of the Polydomain-Monodomain Transition in Main-Chain Liquid Crystal Elastomers," Polymer, **98**, pp. 165–171. https://doi.org/10.1016/j.polymer.2016.06.022.

[37] Clarke, S. M., and Terentjev, E. M., 1998, "Slow Stress Relaxation in Randomly Disordered Nematic Elastomers and Gels," Phys. Rev. Lett., **81**(20), pp. 4436–4439. https://doi.org/10.1103/PhysRevLett.81.4436.

[38] Giamberini, M., Ambrogi, V., Cerruti, P., and Carfagna, C., 2006, "Viscoelasticity of Main Chain Liquid Crystalline Elastomers," Polymer, **47**(13), pp. 4490–4496. https://doi.org/10.1016/j.polymer.2006.04.021.

[39] Hotta, A., and Terentjev, E., 2001, "Long-Time Stress Relaxation in Polyacrylate Nematic Liquid Crystalline Elastomers," Journal of Physics-Condensed Matter, **13**, pp. 11453–11464. https://doi.org/10.1088/0953-8984/13/50/305.

[40] Martin Linares, C. P., Traugutt, N. A., Saed, M. O., Martin Linares, A., Yakacki, C. M., and Nguyen, T. D., 2020, "The Effect of Alignment on the Rate-Dependent Behavior of a

Main-Chain Liquid Crystal Elastomer," Soft Matter, **16**(38), pp. 8782–8798. https://doi.org/10.1039/D0SM00125B.

[41] Ortiz, C., K. Ober, C., and Kramer, E. J., 1998, "Stress Relaxation of a Main-Chain, Smectic, Polydomain Liquid Crystalline Elastomer," Polymer, **39**(16), pp. 3713–3718. https://doi.org/10.1016/S0032-3861(97)10321-4.

[42] Urayama, K., Honda, S., and Takigawa, T., 2006, "Slow Dynamics of Shape Recovery of Disordered Nematic Elastomers," Phys. Rev. E, **74**(4), p. 041709. https://doi.org/10.1103/PhysRevE.74.041709.

[43] Urayama, K., Kondo, H., Arai, Y. O., and Takigawa, T., 2005, "Electrically Driven Deformations of Nematic Gels," Phys. Rev. E, **71**(5), p. 051713. https://doi.org/10.1103/PhysRevE.71.051713.

[44] Urayama, K., Honda, S., and Takigawa, T., 2006, "Deformation Coupled to Director Rotation in Swollen Nematic Elastomers under Electric Fields," Macromolecules, **39**(5), pp. 1943–1949. https://doi.org/10.1021/ma052762q.

[45] Clarke, S. M., Hotta, A., Tajbakhsh, A. R., and Terentjev, E. M., 2002, "Effect of Cross-Linker Geometry on Dynamic Mechanical Properties of Nematic Elastomers," Phys. Rev. E, **65**(2), p. 021804. https://doi.org/10.1103/PhysRevE.65.021804.

[46] Clarke, S., Tajbakhsh, A., Terentjev, E., Remillat, C., Tomlinson, G., and House, J., 2001, "Soft Elasticity and Mechanical Damping in Liquid Crystalline Elastomers," Journal of Applied Physics, **89**, pp. 6530–6535. https://doi.org/10.1063/1.1368177.

[47] Clarke, S. M., and Terentjev, E. M., 1999, "Slow Stress Relaxation in Liquid Crystal Elastomers and Gels," Faraday Disc., **112**, pp. 325–333. https://doi.org/10.1039/a808847k.

[48] Qi, Y., Zou, Z., Xiao, J., and Long, R., 2019, "Mapping the Nonlinear Crack Tip Deformation Field in Soft Elastomer with a Particle Tracking Method," Journal of the Mechanics and Physics of Solids, **125**, pp. 326–346. https://doi.org/10.1016/j.jmps.2018.12.018.

[49] Long, R., Hui, C.-Y., Gong, J. P., and Bouchbinder, E., 2021, "The Fracture of Highly Deformable Soft Materials: A Tale of Two Length Scales," Annual Review of Condensed Matter Physics, **12**(1), pp. 71–94. https://doi.org/10.1146/annurev-conmatphys-042020-023937.

[50] Lu, Y., Qi, Y., Tenardi, M., and Long, R., 2021, "Mixed-Mode Fracture in a Soft Elastomer," Extreme Mechanics Letters, **48**, p. 101380. https://doi.org/10.1016/j.eml.2021.101380.

[51] Jiang, Y., Jin, L., and Huo, Y., 2021, "Unusual Stress and Strain Concentration Behaviors at the Circular Hole of a Large Monodomain Liquid Crystal Elastomer Sheet," Journal of the Mechanics and Physics of Solids, **156**, p. 104615. https://doi.org/10.1016/j.jmps.2021.104615.

[52] Jiang, Y., Li, D., Chen, Y., and Huo, Y., 2023, "Analysis of Stress and Strain Concentration around a Centralized Elliptical Hole in a Monodomain Liquid Crystal Elastomer Sheet," International Journal of Solids and Structures, **264**, p. 112079. https://doi.org/10.1016/j.ijsolstr.2022.112079.

[53] Peng, Z., Jiang, Y., Chen, Y., and Huo, Y., 2023, “Attenuating Liquid Crystal Elastomers’ Stress Concentration by Programming Initial Orientation,” International Journal of Mechanical Sciences, **249**, p. 108274. https://doi.org/10.1016/j.ijmecsci.2023.108274.

[54] Hu, M., Wang, L., Wei, Z., Xiao, R., and Qian, J., 2024, “Fracture and Fatigue Characteristics of Monodomain and Polydomain Liquid Crystal Elastomers,” Soft Matter. https://doi.org/10.1039/D4SM01042F.

[55] Zhou, Y., Wei, C., and Jin, L., 2024, “Fracture of Liquid Crystal Elastomers,” In preparation.

[56] Yeoh, O. H., 2001, “Analysis of Deformation and Fracture of ‘Pure Shear’ Rubber Testpiece,” Plastics, Rubber and Composites, **30**(8), pp. 389–397. https://doi.org/10.1179/146580101101541787.

[57] Shrimali, B., and Lopez-Pamies, O., 2023, “The ‘Pure-Shear’ Fracture Test for Viscoelastic Elastomers and Its Revelation on Griffith Fracture,” Extreme Mechanics Letters, **58**, p. 101944. https://doi.org/10.1016/j.eml.2022.101944.

[58] Ciavarella, M., Cricri, G., and McMeeking, R., 2021, “A Comparison of Crack Propagation Theories in Viscoelastic Materials,” Theoretical and Applied Fracture Mechanics, **116**, p. 103113. https://doi.org/10.1016/j.tafmec.2021.103113.

[59] Hui, C.-Y., Zhu, B., and Long, R., 2022, “Steady State Crack Growth in Viscoelastic Solids: A Comparative Study,” Journal of the Mechanics and Physics of Solids, **159**, p. 104748. https://doi.org/10.1016/j.jmps.2021.104748.

[60] Annapooranan, R., and Cai, S., 2022, “Thermally Induced Self-Rupture of a Constrained Liquid Crystal Elastomer,” Engineering Fracture Mechanics, **269**, p. 108584. https://doi.org/10.1016/j.engfracmech.2022.108584.

[61] Fan, W., Wang, Z., and Cai, S., 2016, “Rupture of Polydomain and Monodomain Liquid Crystal Elastomer,” Int. J. Appl. Mechanics, **08**(07), p. 1640001. https://doi.org/10.1142/S1758825116400019.

[62] Wei, C., Cao, S., Zhou, Y., Lin, D., and Jin, L., 2023, “Rate-Dependent Stress-Order Coupling in Main-Chain Liquid Crystal Elastomers,” Soft Matter, **19**(41), pp. 7923–7936.

[63] Wei, C., Zhou, Y., Hsu, B., and Jin, L., 2024, “Exceptional Stress-Director Coupling at the Crack Tip of a Liquid Crystal Elastomer,” Journal of the Mechanics and Physics of Solids, **183**, p. 105522.

[64] Wei, C., Zhou, Y., and Jin, L., 2025, “Intriguing Crack Propagation of Liquid Crystal Elastomers,” preparation.

[65] Schönstein, M., Stille, W., and Strobl, G., 2001, “Effect of the Network on the Director Fluctuations in a Nematic Side-Group Elastomer Analysed by Static and Dynamic Light Scattering,” The European Physical Journal E, **5**(5), pp. 511–517. https://doi.org/10.1007/s101890170034.

[66] Traugutt, N. A., Volpe, R. H., Bollinger, M. S., Saed, M. O., Torbati, A. H., Yu, K., Dadivanyan, N., and Yakacki, C. M., 2017, “Liquid-Crystal Order during Synthesis Affects Main-Chain Liquid-Crystal Elastomer Behavior,” Soft Matter, **13**(39), pp. 7013–7025. https://doi.org/10.1039/C7SM01405H.

[67] Murthy, N. S., and Minor, H., 1990, “General Procedure for Evaluating Amorphous Scattering and Crystallinity from X-Ray Diffraction Scans of Semicrystalline Polymers,” Polymer, **31**(6), pp. 996–1002. https://doi.org/10.1016/0032-3861(90)90243-R.

[68] Ortiz, C., Wagner, M., Bhargava, N., Ober, C. K., and Kramer, E. J., 1998, “Deformation of a Polydomain, Smectic Liquid Crystalline Elastomer,” Macromolecules, **31**(24), pp. 8531–8539. https://doi.org/10.1021/ma971423x.

[69] Li, J., Tammer, M., Kremer, F., Komp, A., and Finkelmann, H., 2005, “Strain-Induced Reorientation and Mobility in Nematic Liquid-Crystalline Elastomers as Studied by Time-Resolved FTIR Spectroscopy,” Eur. Phys. J. E, **17**(4), pp. 423–428. https://doi.org/10.1140/epje/i2005-10018-6.

[70] Tammer, M., Li, J., Komp, A., Finkelmann, H., and Kremer, F., 2005, “FTIR-Spectroscopy on Segmental Reorientation of a Nematic Elastomer under External Mechanical Fields,” Macromolecular Chemistry and Physics, **206**(7), pp. 709–714. https://doi.org/10.1002/macp.200500050.

[71] Ortiz, C., Kim, R., Rodighiero, E., Ober, C. K., and Kramer, E. J., 1998, “Deformation of a Polydomain, Liquid Crystalline Epoxy-Based Thermoset,” Macromolecules, **31**(13), pp. 4074–4088. https://doi.org/10.1021/ma971439n.

[72] Zhang, Y., Xuan, C., Jiang, Y., and Huo, Y., 2019, “Continuum Mechanical Modeling of Liquid Crystal Elastomers as Dissipative Ordered Solids,” Journal of the Mechanics and Physics of Solids, **126**, pp. 285–303. https://doi.org/10.1016/j.jmps.2019.02.018.

[73] Zhou, H., and Bhattacharya, K., 2021, “Accelerated Computational Micromechanics and Its Application to Polydomain Liquid Crystal Elastomers,” Journal of the Mechanics and Physics of Solids, **153**, p. 104470. https://doi.org/10.1016/j.jmps.2021.104470.

[74] Wang, Z., El Hajj Chehade, A., Govindjee, S., and Nguyen, T. D., 2022, “A Nonlinear Viscoelasticity Theory for Nematic Liquid Crystal Elastomers,” Journal of the Mechanics and Physics of Solids, **163**, p. 104829. https://doi.org/10.1016/j.jmps.2022.104829.

[75] Saed, M. O., Torbati, A. H., Nair, D. P., and Yakacki, C. M., 2016, “Synthesis of Programmable Main-Chain Liquid-Crystalline Elastomers Using a Two-Stage Thiol-Acrylate Reaction,” JoVE (Journal of Visualized Experiments), (107), p. e53546. https://doi.org/10.3791/53546.

[76] Blaber, J., Adair, B., and Antoniou, A., 2015, “Ncorr: Open-Source 2D Digital Image Correlation Matlab Software,” Exp Mech, **55**(6), pp. 1105–1122. https://doi.org/10.1007/s11340-015-0009-1.

[77] Jin, L., Zeng, Z., and Huo, Y., 2010, “Thermomechanical Modeling of the Thermo-Order–Mechanical Coupling Behaviors in Liquid Crystal Elastomers,” Journal of the Mechanics and Physics of Solids, **58**(11), pp. 1907–1927. https://doi.org/10.1016/j.jmps.2010.07.019.

[78] Reese, S., and Govindjee, S., 1998, “A Theory of Finite Viscoelasticity and Numerical Aspects,” International Journal of Solids and Structures, **35**(26–27), pp. 3455–3482. https://doi.org/10.1016/S0020-7683(97)00217-5.

[79] Verwey, G. C., and Warner, M., 1995, “Soft Rubber Elasticity,” Macromolecules, **28**(12), pp. 4303–4306. https://doi.org/10.1021/ma00116a036.

[80] Warner, M., Bladon, P., and Terentjev, E. M., 1994, "'Soft Elasticity' — Deformation without Resistance in Liquid Crystal Elastomers," J. Phys. II France, **4**(1), pp. 93–102. https://doi.org/10.1051/jp2:1994116.

[81] Bladon, P., Terentjev, E. M., and Warner, M., 1993, "Transitions and Instabilities in Liquid Crystal Elastomers," Phys. Rev. E, **47**(6), pp. R3838–R3840. https://doi.org/10.1103/PhysRevE.47.R3838.

[82] Sonnet, A. M., and Virga, E. G., 2012, *Dissipative Ordered Fluids: Theories for Liquid Crystals*, Springer Science & Business Media.

[83] Biggins, J. S., Terentjev, E. M., and Warner, M., 2008, "Semisoft Elastic Response of Nematic Elastomers to Complex Deformations," Phys. Rev. E, **78**(4), p. 041704. https://doi.org/10.1103/PhysRevE.78.041704.

[84] Verwey, G. C., Warner, M., and Terentjev, E. M., 1996, "Elastic Instability and Stripe Domains in Liquid Crystalline Elastomers," J. Phys. II France, **6**(9), pp. 1273–1290. https://doi.org/10.1051/jp2:1996130.

[85] Finkelmann, H., Kundler, I., Terentjev, E. M., and Warner, M., 1997, "Critical Stripe-Domain Instability of Nematic Elastomers," J. Phys. II France, **7**(8), pp. 1059–1069. https://doi.org/10.1051/jp2:1997171.

[86] Zhang, T., Lin, S., Yuk, H., and Zhao, X., 2015, "Predicting Fracture Energies and Crack-Tip Fields of Soft Tough Materials," Extreme Mechanics Letters, **4**, pp. 1–8. https://doi.org/10.1016/j.eml.2015.07.007.

[87] Lin, S., Zhou, Y., and Zhao, X., 2014, "Designing Extremely Resilient and Tough Hydrogels via Delayed Dissipation," Extreme Mechanics Letters, **1**, pp. 70–75. https://doi.org/10.1016/j.eml.2014.11.002.

[88] Liu, M., Guo, J., Hui, C.-Y., and Zehnder, A. T., 2019, "Application of Digital Image Correlation (DIC) to the Measurement of Strain Concentration of a PVA Dual-Crosslink Hydrogel Under Large Deformation," Exp Mech, **59**(7), pp. 1021–1032. https://doi.org/10.1007/s11340-019-00520-4.

[89] Long, R., and Hui, C.-Y., 2015, "Crack Tip Fields in Soft Elastic Solids Subjected to Large Quasi-Static Deformation — A Review," Extreme Mechanics Letters, **4**, pp. 131–155. https://doi.org/10.1016/j.eml.2015.06.002.

[90] Rivlin, R. S., and Thomas, A. G., 1953, "Rupture of Rubber. I. Characteristic Energy for Tearing," Journal of Polymer Science, **10**(3), pp. 291–318. https://doi.org/10.1002/pol.1953.120100303.

[91] Knowles, J. K., and Sternberg, E., 1973, "An Asymptotic Finite-Deformation Analysis of the Elastostatic Field near the Tip of a Crack," J Elasticity, **3**(2), pp. 67–107. https://doi.org/10.1007/BF00045816.

[92] Verwey, G. C., and Warner, M., 1997, "Compositional Fluctuations and Semisoftness in Nematic Elastomers," Macromolecules, **30**(14), pp. 4189–4195. https://doi.org/10.1021/ma961801i.

[93] Frank, F. C., 1958, "I. Liquid Crystals. On the Theory of Liquid Crystals," Discuss. Faraday Soc., **25**(0), pp. 19–28. https://doi.org/10.1039/DF9582500019.

[94] de Souza Neto, E. A., Perić, D., Dutko, M., and Owen, D. R. J., 1996, "Design of Simple Low Order Finite Elements for Large Strain Analysis of Nearly Incompressible Solids," International Journal of Solids and Structures, **33**(20–22), pp. 3277–3296. https://doi.org/10.1016/0020-7683(95)00259-6.

[95] Chester, S. A., Di Leo, C. V., and Anand, L., 2015, "A Finite Element Implementation of a Coupled Diffusion-Deformation Theory for Elastomeric Gels," International Journal of Solids and Structures, **52**, pp. 1–18. https://doi.org/10.1016/j.ijsolstr.2014.08.015.

[96] Rice, J. R., 1968, "A Path Independent Integral and the Approximate Analysis of Strain Concentration by Notches and Cracks," Journal of Applied Mechanics, **35**(2), pp. 379–386. https://doi.org/10.1115/1.3601206.

[97] Knowles, J. K., and Sternberg, E., 1974, "Finite-Deformation Analysis of the Elastostatic Field near the Tip of a Crack: Reconsideration and Higher-Order Results," J Elasticity, **4**(3), pp. 201–233. https://doi.org/10.1007/BF00049265.

[98] Gasser, T. C., Ogden, R. W., and Holzapfel, G. A., 2005, "Hyperelastic Modelling of Arterial Layers with Distributed Collagen Fibre Orientations," Journal of The Royal Society Interface, **3**(6), pp. 15–35. https://doi.org/10.1098/rsif.2005.0073.

[99] Broberg, K. B., 1999, *Cracks and Fracture*, Elsevier.

[100] Kanninen, M. F., McEvily, A. J., and Popelar, C. H., 1986, "Advanced Fracture Mechanics." https://doi.org/10.1115/1.3225862.

[101] Li, F. Z., Shih, C. F., and Needleman, A., 1985, "A Comparison of Methods for Calculating Energy Release Rates," Engineering Fracture Mechanics, **21**(2), pp. 405–421. https://doi.org/10.1016/0013-7944(85)90029-3.

[102] Wang, Z., Boechler, N., and Cai, S., 2022, "Anisotropic Mechanical Behavior of 3D Printed Liquid Crystal Elastomer," Additive Manufacturing, **52**, p. 102678. https://doi.org/10.1016/j.addma.2022.102678.

[103] Sutton, M. A., Deng, X., Ma, F., Newman Jr, J. C., and James, M., 2000, "Development and Application of a Crack Tip Opening Displacement-Based Mixed Mode Fracture Criterion," International Journal of Solids and Structures, **37**(26), pp. 3591–3618. https://doi.org/10.1016/S0020-7683(99)00055-4.

[104] Corre, T., Coret, M., Verron, E., Leblé, B., and Le Lay, F., 2020, "Experimental Full Field Analysis for Dynamic Fracture of Elastomer Membranes," Int J Fract, **224**(1), pp. 83–100. https://doi.org/10.1007/s10704-020-00447-1.

[105] Zhang, Y., Fukao, K., Matsuda, T., Nakajima, T., Tsunoda, K., Kurokawa, T., and Gong, J. P., 2022, "Unique Crack Propagation of Double Network Hydrogels under High Stretch," Extreme Mechanics Letters, **51**, p. 101588. https://doi.org/10.1016/j.eml.2021.101588.

[106] Morishita, Y., Tsunoda, K., and Urayama, K., 2017, "Crack-Tip Shape in the Crack-Growth Rate Transition of Filled Elastomers," Polymer, **108**, pp. 230–241. https://doi.org/10.1016/j.polymer.2016.11.041.

[107] Zheng, Y., and Gong, J. P., 2025, "Viscous Solvent Effect on Fracture of Predamaged Double-Network Gels Examined by Pre-Notch and Post-Notch Crack Tests," Journal of the Mechanics and Physics of Solids, **194**, p. 105926. https://doi.org/10.1016/j.jmps.2024.105926.

[108] Morishita, Y., Tsunoda, K., and Urayama, K., 2016, "Velocity Transition in the Crack Growth Dynamics of Filled Elastomers: Contributions of Nonlinear Viscoelasticity," Phys. Rev. E, **93**(4), p. 043001. https://doi.org/10.1103/PhysRevE.93.043001.

[109] Morishita, Y., Tsunoda, K., and Urayama, K., 2019, "Universal Relation between Crack-Growth Dynamics and Viscoelasticity in Glass-Rubber Transition for Filled Elastomers," Polymer, **179**, p. 121651. https://doi.org/10.1016/j.polymer.2019.121651.

[110] Mandal, T. K., Nguyen, V. P., and Wu, J.-Y., 2020, "A Length Scale Insensitive Anisotropic Phase Field Fracture Model for Hyperelastic Composites," International Journal of Mechanical Sciences, **188**, p. 105941. https://doi.org/10.1016/j.ijmecsci.2020.105941.

[111] Wu, J.-Y., Nguyen, V. P., Nguyen, C. T., Sutula, D., Sinaie, S., and Bordas, S. P. A., 2020, "Phase-Field Modeling of Fracture," *Advances in Applied Mechanics*, Elsevier, pp. 1–183. https://doi.org/10.1016/bs.aams.2019.08.001.

[112] Mattey, R., Jewell, B., Ghosh, S., and Sain, T., 2023, "Phase-Field Fracture Coupled Elasto-Plastic Constitutive Model for 3D Printed Thermoplastics and Composites," Engineering Fracture Mechanics, **291**, p. 109535. https://doi.org/10.1016/j.engfracmech.2023.109535.

[113] Li, P., Li, W., Li, B., Yang, S., Shen, Y., Wang, Q., and Zhou, K., 2023, "A Review on Phase Field Models for Fracture and Fatigue," Engineering Fracture Mechanics, **289**, p. 109419. https://doi.org/10.1016/j.engfracmech.2023.109419.

[114] Yu, Y., Hou, C., Zheng, X., Rabczuk, T., and Zhao, M., 2023, "A Generally Variational Phase Field Model of Fracture," Theoretical and Applied Fracture Mechanics, **128**, p. 104111. https://doi.org/10.1016/j.tafmec.2023.104111.

[115] Loew, P. J., Peters, B., and Beex, L. A. A., 2019, "Rate-Dependent Phase-Field Damage Modeling of Rubber and Its Experimental Parameter Identification," Journal of the Mechanics and Physics of Solids, **127**, pp. 266–294. https://doi.org/10.1016/j.jmps.2019.03.022.

[116] Pham, K., Amor, H., Marigo, J.-J., and Maurini, C., 2011, "Gradient Damage Models and Their Use to Approximate Brittle Fracture," International Journal of Damage Mechanics, **20**(4), pp. 618–652. https://doi.org/10.1177/1056789510386852.

[117] Dammaß, F., Kalina, K. A., Ambati, M., and Kästner, M., 2023, "Phase-Field Modelling and Analysis of Rate-Dependent Fracture Phenomena at Finite Deformation," Comput Mech, **72**(5), pp. 859–883. https://doi.org/10.1007/s00466-023-02310-1.

[118] Stortini, N., 2024, "Phase-Field Fracture Models for Elastomers." [Online]. Available: https://iris.uniroma1.it/handle/11573/1710487. [Accessed: 18-Jan-2025].

[119] Yang, Z., Zhu, Z., Xia, Y., Yang, F., Sun, Y., and Jiang, H., 2021, "Modified Cohesive Zone Model for Soft Adhesive Layer Considering Rate Dependence of Intrinsic Fracture Energy," Engineering Fracture Mechanics, **258**, p. 108089. https://doi.org/10.1016/j.engfracmech.2021.108089.

[120] Persson, B. N. J., and Brener, E. A., 2005, "Crack Propagation in Viscoelastic Solids," Phys. Rev. E, **71**(3), p. 036123. https://doi.org/10.1103/PhysRevE.71.036123.

[121] Ju, J., Sanoja, G. E., Nagazi, M. Y., Cipelletti, L., Liu, Z., Hui, C. Y., Ciccotti, M., Narita, T., and Creton, C., 2023, "Real-Time Early Detection of Crack Propagation Precursors in Delayed Fracture of Soft Elastomers," Phys. Rev. X, **13**(2), p. 021030. https://doi.org/10.1103/PhysRevX.13.021030.

[122] 1921, "VI. The Phenomena of Rupture and Flow in Solids," Phil. Trans. R. Soc. Lond. A, **221**(582–593), pp. 163–198. https://doi.org/10.1098/rsta.1921.0006.

[123] Bourdin, B., Francfort, G. A., and Marigo, J.-J., 2000, "Numerical Experiments in Revisited Brittle Fracture," Journal of the Mechanics and Physics of Solids, **48**(4), pp. 797–826. https://doi.org/10.1016/S0022-5096(99)00028-9.

[124] Wu, J.-Y., 2017, "A Unified Phase-Field Theory for the Mechanics of Damage and Quasi-Brittle Failure," Journal of the Mechanics and Physics of Solids, **103**, pp. 72–99. https://doi.org/10.1016/j.jmps.2017.03.015.

[125] Teichtmeister, S., Kienle, D., Aldakheel, F., and Keip, M.-A., 2017, "Phase Field Modeling of Fracture in Anisotropic Brittle Solids," International Journal of Non-Linear Mechanics, **97**, pp. 1–21. https://doi.org/10.1016/j.ijnonlinmec.2017.06.018.

[126] Miehe, C., Hofacker, M., and Welschinger, F., 2010, "A Phase Field Model for Rate-Independent Crack Propagation: Robust Algorithmic Implementation Based on Operator Splits," Computer Methods in Applied Mechanics and Engineering, **199**(45), pp. 2765–2778. https://doi.org/10.1016/j.cma.2010.04.011.

[127] Zhou, Y., Wei, C., and Jin, L., 2024, "A Modified Semi-Soft Model of Liquid Crystal Elastomers: Application to Elastic and Viscoelastic Responses," Under Revision.

[128] Rezaei, L., Scalet, G., Peigney, M., and Azoug, A., 2024, "Coupling between Viscoelasticity and Soft Elasticity in Main-Chain Nematic Liquid Crystal Elastomers," Journal of the Mechanics and Physics of Solids, **187**, p. 105612. https://doi.org/10.1016/j.jmps.2024.105612.

[129] DeSimone, A., and Dolzmann, G., 2002, "Macroscopic Response of¶Nematic Elastomers via Relaxation Of¶a Class of SO(3)-Invariant Energies," Arch. Rational Mech. Anal., **161**(3), pp. 181–204. https://doi.org/10.1007/s002050100174.

[130] Hughes, T. J. R., 1980, "Generalization of Selective Integration Procedures to Anisotropic and Nonlinear Media," International Journal for Numerical Methods in Engineering, **15**(9), pp. 1413–1418. https://doi.org/10.1002/nme.1620150914.